GRAZ UNIVERSITY OF TECHNOLOGY

MASTER THESIS

Numerical flow analysis of a mixing chamber in a turbine test rig

Supervisor:
Ao.Univ-Prof. Dipl.-Ing.
Dr.techn. Wolfgang SANZ

presented by:
Achilles KEFALAS

Head of the Institute:
Univ.-Prof. Dr.-Ing. Franz
HEITMEIR

Institute for Thermal Turbomachinery and Machine Dynamics

Die Sorge um die Menschen und ihr Schicksal muß stets das Hauptinteresse allen technischen Strebens bilden, die großen ungelösten Fragen der Organisation von Arbeit und der Güterverteilung, damit die Erzeugnisse unseres Geistes dem Menschengeschlecht zum Segen gereichen und nicht zum Fluche. Vergeßt dies nie über Euren Zeichnungen und Gleichungen.

Albert Einstein, Februar 1931

Danksagung

An dieser Stelle möchte ich mich bei Herrn Ao.Univ-Prof. Dipl.-Ing. Dr.techn. Wolfgang Sanz für die Betreuung dieser Diplomarbeit am Institut für Thermische Turbomaschinen und Maschinendynamik bedanken.

Mein Dank gilt auch Herrn Dipl.-Ing. Thorsten Selic, der mich tatkräftig in jeder Phase dieser Arbeit unterstützt hat und immer geniale Lösungsansätze parat gehabt hat.

Weiters gilt mein Dank auch Herrn Dipl.-Ing. Christian Faustmann und dem Institut für Thermische Turbomaschinen und Maschinendynamik, die diese Arbeit ermöglicht haben und mir die benötigte Software, sowie die Rechnerkapazität zur Verfügung gestellt haben.

Außerdem will ich mich auch bei Herrn Univ-Prof. Dr.-Ing. Franz Heitmeir und Univ-Prof. Dr.-Ing. habil. Günter Brenn bedanken, die in zahlreichen Lehrveranstaltungen mein Interesse für Strömungsmechanik weckten.

Bedanken möchte ich mich auch bei der Technischen Universität Graz, die es durch ihre Lehre ermöglicht ein Fundament für das Leben zu schaffen.

Mein besonderer Dank gilt meinen Eltern und meinen Großeltern, die mir mein Studium ermöglichten und mir immer die nötige Unterstützung von Herzen boten.

Achilles Kefalas

Graz, Oktober 2013

Kurzfassung

Das Institut für Thermische Turbomaschinen und Maschinendynamik führt numerische und experimetelle Untersuchungen zukunftsorientierter Turbinenkomponenten zur Überprüfung der aerodynamischen und akustischen Güte durch. Ziel sind genaue Messungen, die nur dann erreicht werden können, wenn die Temperaturverteilung in der Eintrittsebene vor den Turbinenstufen homogen ist. In einer früheren Diplomarbeit wurden dort Inhomogenitäten festgestellt. Dieses Phänomen wird durch den geringen Durchmischungsweg in der Mischkammer erklärt. In dieser Mischkammer werden zwei verschieden große Luftmassenströme mit ungleichen Temperaturen vermischt. Da sich keine Möglichkeit bietet, im Inneren der Mischkammer Messinstrumente zu installieren wurde eine numerische Analyse der internen Strömung durchgeführt, um zukünftige Vebesserungsmöglichkeiten zu untersuchen.

Abstract

The Institute for Thermal Turbomachinery and Machine Dynamics performs numerical and experimental analysis of prospective turbine components to quantify the aerodynamic and acoustic quality. The target of precise measured values can only be achieved, if the distribution of temperature at the entrance plane upstream of the turbine stages is homogeneous. In a former master thesis inhomogeneities were detected there. This phenomenon is explained by the short mixing length of the chamber. In this chamber two air flows with different mass and temperature get mixed up. Since, there is no possibility of installing measurement probes inside the chamber, a numerical analysis of the internal fluid flow was performed in order to study the improvement potential.

Contents

1 Introduction 9

2 Turbine Test Rig 11
2.1 Capabilities of the Rig 11
2.2 Turbine Inlet Concept 14
2.3 Transonic Turbine Stage 15

3 Measurement Results 16

4 Basics of Computational Fluid Dynamics (Numerical Methods) 19
4.1 Basic Equations of Fluid Mechanics 19
4.2 Navier-Stokes Equations in Conservation Form 20
4.3 Discretization Approaches 21
4.4 Finite Volume Method 22
4.5 Turbulence Modeling 23

5 Mesh Generation 26
5.1 Mesh Varieties 26
5.2 Introducing the Geometry 28
5.3 Geometrical Simplifications 33
5.4 Blocking Tactics and Mesh Partitions 36

6 Pre-processing and Simulation 49
6.1 Pre-processing 49
    6.1.1 Creation of Quality Output Files 49
    6.1.2 The Way to Implement the Grid 50
    6.1.3 The Numerical Grid 53
6.2 Simulation 54
    6.2.1 Numerical Analysis Tactic 54
    6.2.2 Case Setup 56
    6.2.3 Solution Strategy for Compressible Flows 58

7 Results 59
7.1 Simulation Results for the First Operating Point 59
7.2 Simulation Results for the Second Operating Point 72
7.3 Simulation Results for the Third Operating Point 80
7.4 Weak Points and Potential Improvements 88

7.5 Evaluation of Results 104

8 Closing Words 106

Nomenclature 107

List of Figures 107

List of Tables 111

Bibliography 113

1 Introduction

Following the process of development for jet engine components it is noticeable, that a test rig is needed to measure all significant aerodynamic and acoustic values. In such a test rig, one has to guarantee enough mass flow of compressible fluid at the inlet plane of the turbine stage, which is to be analysed. In the present test rig this is provided by a compressor unit, stationed in the basement of the Institute for Thermal Turbomachinery and Machine Dynamics and a brake compressor, stationed directly in test area. They provide air flows of different properties, which get mixed up on the internal way through a mixing chamber, to finally reach the inlet plane of the test turbine see Figure 1.1. It is of great importance, that the temperature distribution at that plane is as homogeneous as possible to achieve precise acoustic measurements. In the present thesis the internal fluid flow of the mixing chamber, from the two inlets to the inlet plane of the turbine will be analysed numerically.

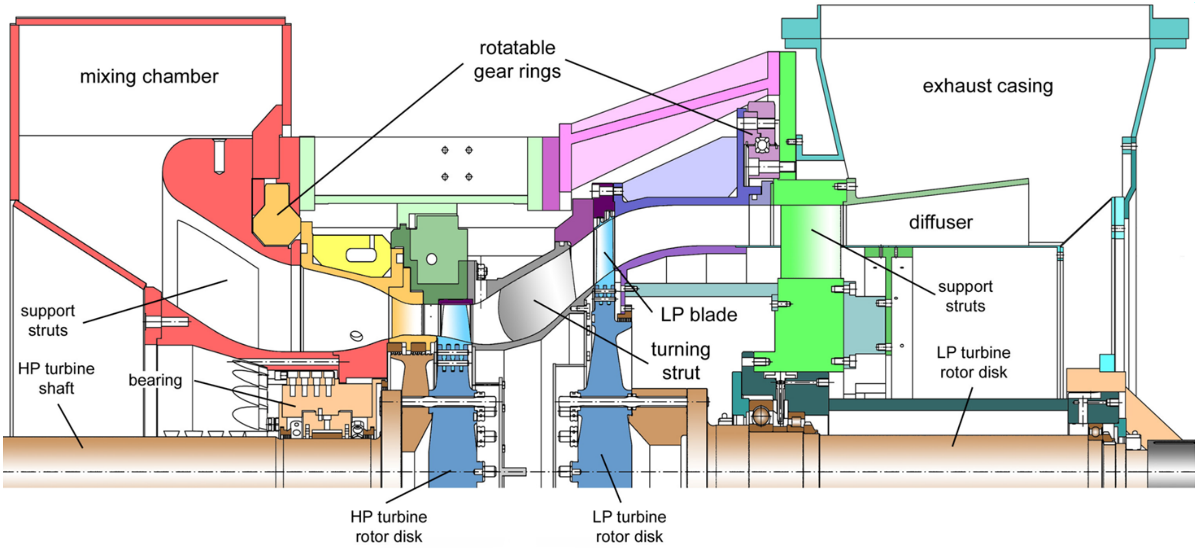

Figure 1.1: Turbine test rig

This analysis will be done for three defined operating points, where the pressure and temperature distributions at inlets of the mixing chamber and the inlet plane for the transonic turbine stage, which in that case represents the outlet of the chamber, were measured by the Institute for Thermal Turbomachinery and Machine Dynamics and are therefore known. This data will provide the boundary conditions of the simulations which will take place. The result and object of interest will be the temperature, pressure

and turbulent intensity distribution at the entrance plane of the turbine, which will then be compared with measurements.
In the following section a brief overview of the steps carried out in the present work shall be given.

- The turbine test rig is presented with a brief description of all its components. Special attention will be drawn to the compressor units, which provide pressurized air to the rig, the mixing chamber, which is the object of interest of this thesis and the transonic turbine stage.
- Results of performed measurements are presented and discussed.
- The mixing chamber geometry gets adopted by a Computer-aided design(CAD) model, which was constructed with commercial CAD-software. The computational mesh of the interior domain is produced by *ANSYS ICEMcfd V13*. It will be necessary to generate a structured hexahedron-prism mesh to capture the numerous interior volume partitions of the mixing chamber. The result will be shown in detail.
- Simulations are performed by the commercial Computational Fluid Dynamics(CFD) software *ANSYS Fluent V14*. The numerical analysis of the three defined operating points will be discussed through from the setup level to the results.
- A discussion on improvement potentials and weak points in the geometry will follow.
- An evaluation of the obtained results in comparison with the measurements is presented.

To obtain accurate results in the CFD simulation we have to give attention to the mesh quality, the right choice of turbulence and wall model and the correct setup of the solver.

2 Turbine Test Rig

In the present chapter an overview of the turbine test rig is presented, with a short description of components and special focus on the mixing chamber.

2.1 Capabilities of the Rig

At the Institute for Thermal Turbomachinery and Machine Dynamics a compressor station consisting of two turbo and one double screw compressor is located in the basement. It can be operated in various configurations, so that air can be continuously provided from $2,5\frac{kg}{s}$ up to almost $16\frac{kg}{s}$ with a pressure ratio reaching $2,9bar$ in parallel operation and $9,0\frac{kg}{s}$ at $10bar$ in serial operation.

The temperature is adjustable from $150°C$ down to $15°C$. The test turbine supply pipe ($350mm$ diameter) connects the $3bar$ low pressure or the high pressure line to the inlet casing of the test turbine, which can be operated at a maximum of $5bar$. The additional air from the brake compressor gets mixed and straightened up in vertical direction through a tandem cascade. Then the flow enters the inlet housing, where it accelerates further downstream to the nozzle and generates up to $2MW$ in the blading of the test turbine.

The direct transmission of this turbine shaft power to a three stage centrifugal compressor GHH G5-6/3L is provided by a membrane coupling. Air of the test hall gets sucked through a large filter, which is followed by a venturi nozzle for mass flow measurement and adjustable inlet guide vanes give the opportunity to manually control the absorbing brake power.

The provided compressed air by this machine can be additionally used to drive the test turbine, if the pressure ratio is lower than approximately 4 and the rotational speed of the stage is high enough. The overflow pipe ($350mm$ diameter) connects the GHH brake compressor with the turbine. This pipe provides the pressurized air to the mixer located at the bottom of the inlet casing to keep temperature distortion at the stage inlet as small as possible. This configuration allows to, approximately double the mass flow, which is a great advantage in testing high loaded turbine stages in full flow similarity.

The GHH compressor has the same speed as the turbine shaft, therefore a bypass to the exhaust line is necessary, if the inlet pressure of the test stage is higher than the exit pressure of the brake compressor at test speed. Figure 2.1 shows the flow scheme of the transonic test turbine facility [4].

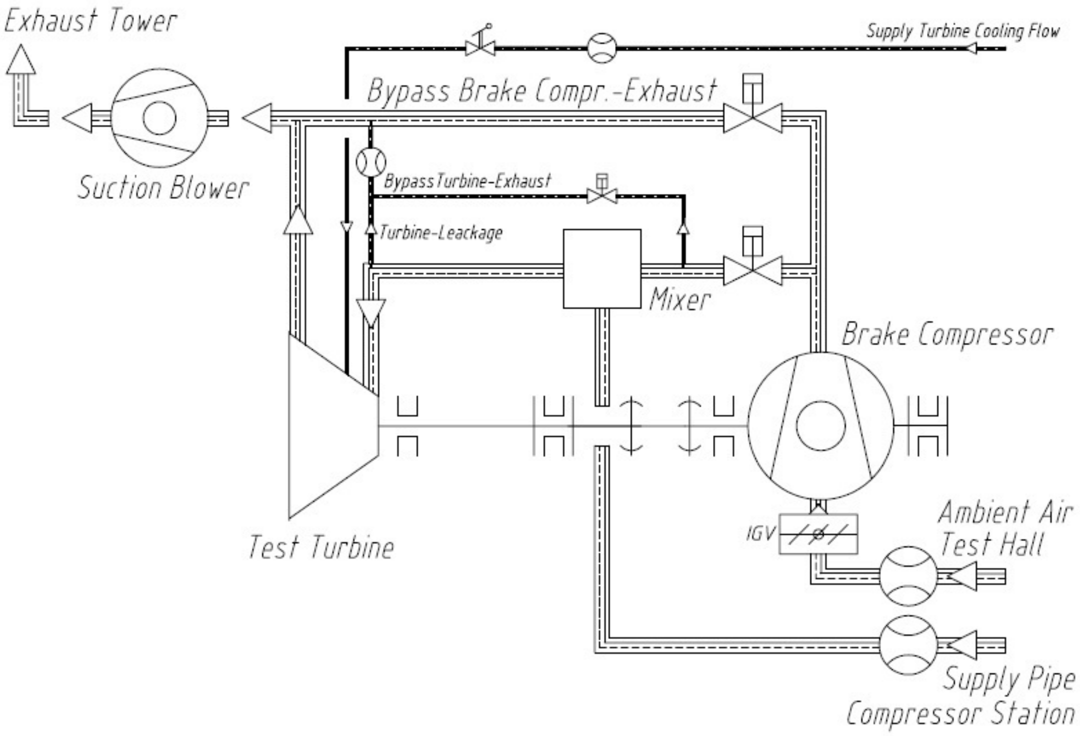

Figure 2.1: Transonic test-turbine facility flow scheme

Normally, the exit condition after the diffuser is set to ambient pressure. For gaining more freedom in pressure ratio and power, a suction blower assembly was built up, which can be integrated in the exhaust line just before the exhaust tower, if necessary.

The following Figure 2.2 visualizes the air supply of the test rig. For further detailed informations, see [4] and [5].

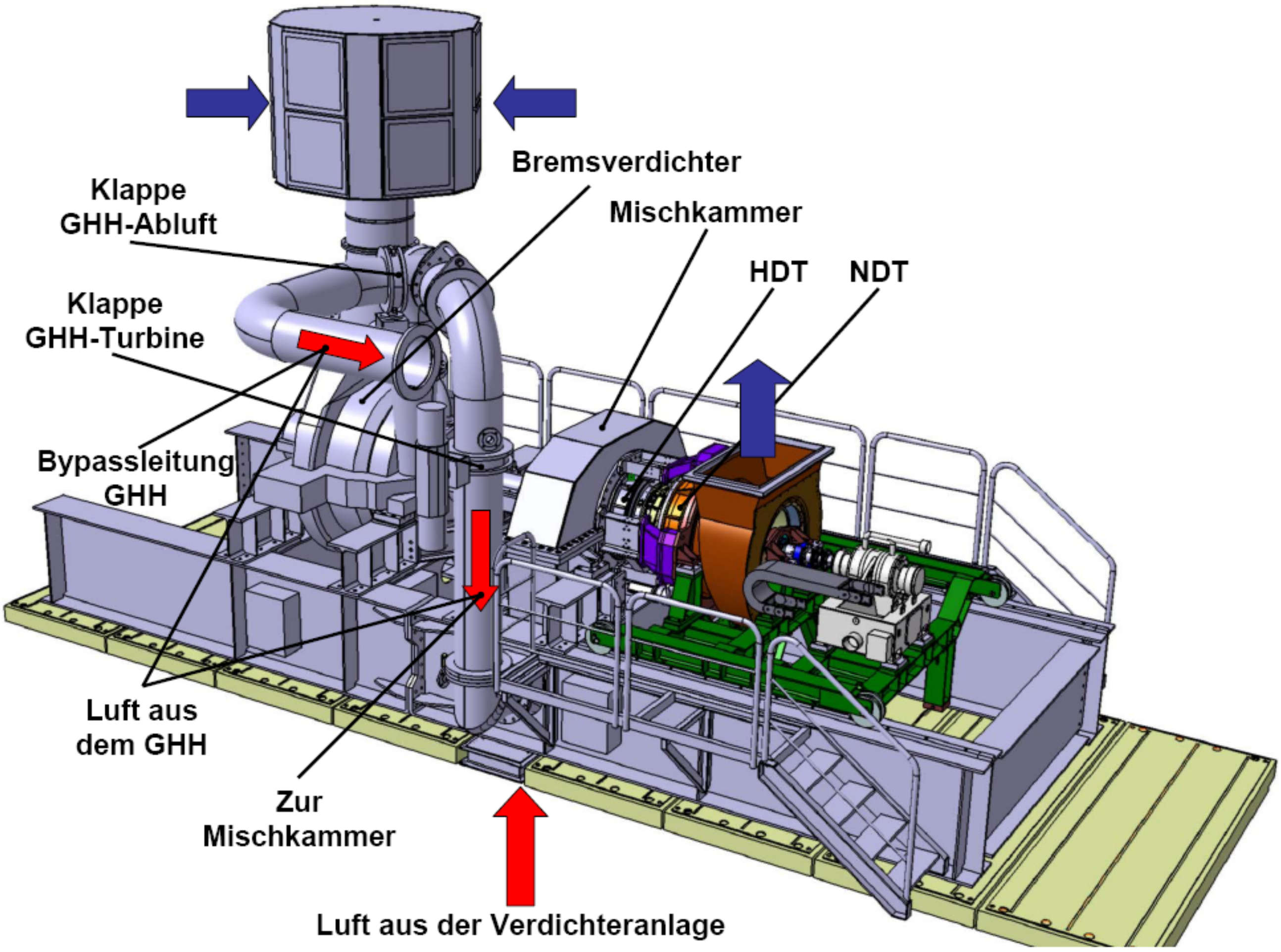

Figure 2.2: Test rig with ways of air supply

2.2 Turbine Inlet Concept

The turbine inlet concept was described well by J. Erhard and is therefore shown in the original state in Figure 2.3, obtained from [4].

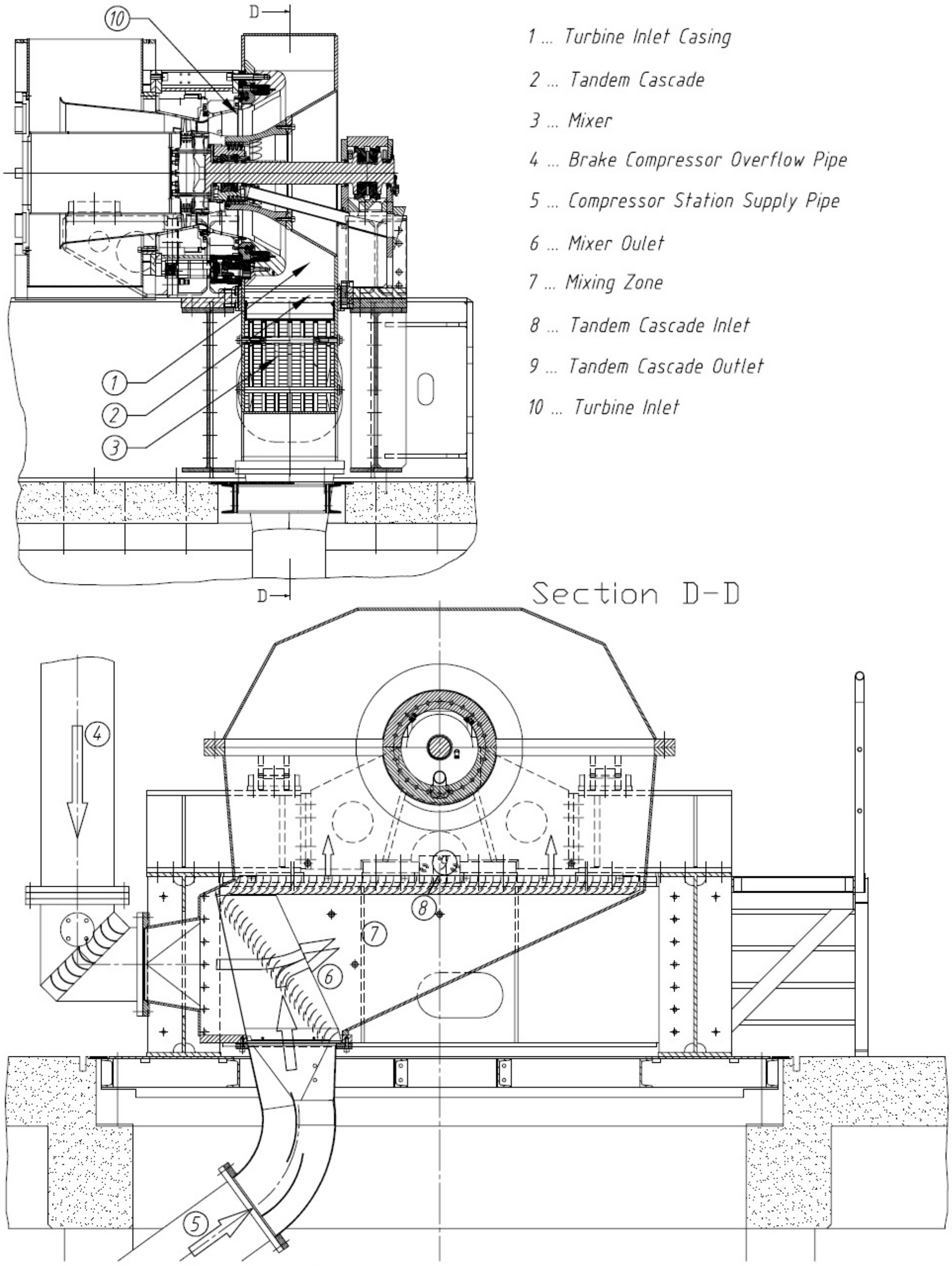

Figure 2.3: Turbine inlet concept, showing GHH- and compressor station inlets, mixer and tandem cascade in section D-D

2.3 Transonic Turbine Stage

J. Erhard performed numerous Navier Stokes simulations in his PhD thesis with different meshes to exclude a possible mesh dependency. With the results presented in [4] as basis, the design point for the TTM-stage was determined.

Table 2.1: Design Point at 11000rpm

Boundary Conditions	
$p_{0_{tot}} = 350000 Pa$	$n = 11000 rpm$
$T_{0_{tot}} = 432,2 K$	$P = 2127 kW$
$p_{2_{stat}} = 100000 Pa$	$\dot{m} = 18,8 \frac{kg}{s}$

Table 2.2: TTM-Stage Parameters

π Pressure ratio (total to static)	3,50
η Stage efficency (total to static)	0,90
ψ Loading factor $-\frac{\Delta h}{u^2}$	1,50
ϕ Flow factor $\frac{c_{ax}}{u}$	0,53
R_{kin} degree of Reaction [%]	32,4

3 Measurement Results

In the present chapter measurement data of the mixing chamber, provided by the Institute for Thermal Turbomachinery and Machine Dynamics will be presented and discussed.

The three measurement locations are at the first inlet of the mixing chamber at Point 5 in Figure 2.3, where air enters from the compressor unit, stationed in the basement. The second location is the inlet, where air is provided by the brake compressor, stationed in the test hall, (Point 4 in Figure 2.3) and the third location is right before the turbine stage or the outlet of the annulus, (downstream Point 10 in Figure 2.3). Following Tables 3.3, 3.1 and 3.2 show the measured quantities. The measurements of first and second part-load operating point were performed in **C1/ADP/Rakemessung360/Auflösung1, 5°**. The third full-load operating point is the design point of the transonic turbine stage. This data was obtained from [4] and [9].

Table 3.1: Measurement data of Part-load Operating Point 1

Inlet SC	
Total pressure $p_{tot,SC}$	$3,957bar$
Mass-flow rate m_{SC}	$8,28\frac{kg}{s}$
Total temperature $T_{tot,SC}$	$394K$
Inlet GHH	
Total pressure $p_{tot,GHH}$	$3,979bar$
Mass-flow rate m_{GHH}	$7,963\frac{kg}{s}$
Total temperature $T_{tot,SC}$	$504,7K$
Outlet	
Total pressure $p_{tot,A}$	$3,922bar$
Static pressure $p_{stat,A}$	$3,908bar$

Table 3.2: Measurement data of Part-load Operating Point 2

Inlet SC	
Total pressure $p_{tot,SC}$	$3,957bar$
Mass-flow rate m_{SC}	$4,8\frac{kg}{s}$
Total temperature $T_{tot,SC}$	$442K$
Inlet GHH	
Total pressure $p_{tot,GHH}$	$3,979bar$
Mass-flow rate m_{GHH}	$6\frac{kg}{s}$
Total temperature $T_{tot,SC}$	$423K$
Outlet	
Total pressure $p_{tot,A}$	$2,581bar$
Static pressure $p_{stat,A}$	$2,573bar$

Table 3.3: Measurement data of Full-load Operating Point

Inlet SC	
Total pressure $p_{tot,SC}$	$-$
Mass-flow rate m_{SC}	$9,5\frac{kg}{s}$
Total temperature $T_{tot,SC}$	$318K$
Inlet GHH	
Total pressure $p_{tot,GHH}$	$-$
Mass-flow rate m_{GHH}	$11,84\frac{kg}{s}$
Total temperature $T_{tot,SC}$	$408K$
Outlet	
Total pressure $p_{tot,A}$	$-$
Static pressure $p_{stat,A}$	$4,4bar$

Basically, **two** ways of imposing the physical boundary conditions on the simulation case are possible.

Giving mass flow rate at the two inlets
and
Giving static (gauge) pressure at the outlet

Giving total pressure at the two inlets
and
giving static (gauge) pressure at the outlet

In the present work the mass flow and static pressure boundary conditions were chosen. The solver calculation is more robust, therefore the chance of a stable and convergent solution is greater. Also, the observation of convergence is easier, because we can follow the mass flow rate at the outlet of the domain, which would be a proof for conserving continuity and the total pressure at the inlets of the domain can also be checked, if the calculated value for average weighted or mass weighted area total pressure is approximated.

4 Basics of Computational Fluid Dynamics (Numerical Methods)

4.1 Basic Equations of Fluid Mechanics

Fluids are substances with the property, that their molecular structure offers no resistance to external forces; even the smallest force causes deformation of a fluid particle. Liquids and gases obey the same laws of motion, despite a significant distinction between them. In most cases of interest, a fluid can be regarded as continuum. One can say, that fluid flow is caused by the action of externally applied forces.

Conservation laws can be derived by considering a quantity of matter or control mass and its extensive properties, such as mass, momentum and energy. Since it is very difficult to follow a parcel of matter in fluids, the idea to deal with the flow in a certain spatial region, we call the control volume, approved itself far more convenient [1].

We derive the *equation of continuity* by writing a mass balance over an arbitrary, infinitesimal control volume. This equation describes the time rate of change of fluid density at a fixed point in space [2].

$$\frac{\partial \rho}{\partial t} + \nabla(\rho \cdot \vec{v}) = 0 \tag{4.1}$$

To get the *equation of motion* we write a momentum balance over the same control volume, which leads to following equation [7].

$$\frac{\partial(\rho \cdot \vec{v})}{\partial t} + \nabla(\rho \cdot \vec{v} \cdot \vec{v}) = -\nabla p + \nabla \cdot \tau + \rho \cdot \vec{f} \tag{4.2}$$

To develop the *equation of energy* we need to write an energy balance over this control volume [7].

$$\frac{\partial(e)}{\partial t} + \nabla(\vec{v} \cdot (e + p)) = \frac{\partial Q}{\partial t} - \nabla \cdot \vec{q} + \nabla \cdot (\tau \cdot \vec{v}) + \rho \cdot \vec{f} \cdot \vec{v} \tag{4.3}$$

These equations of change form the basis for the application of numerical methods and are called Navier-Stokes equations. The material and state values of the flowing fluid, witch is regarded as continuum, can be plotted as continuous functions in 3-dimensional space [8].

4.2 Navier-Stokes Equations in Conservation Form

The independent variables of the differential equations are the values of $\vec{x}$ and t. The dependent variable is the state value vector:

$$\vec{U}_{(x_m,t)} = \begin{pmatrix} \rho \\ \rho \cdot u \\ \rho \cdot v \\ \rho \cdot w \\ \rho \cdot e \end{pmatrix} \tag{4.4}$$

The state value vector contains the variables (mass,momentum and total energy), which are to be conserved. The Navier-Stokes equations for a compressible fluid can now be written in conservation form and vector notation as:

$$\frac{\partial \vec{U}}{\partial t} + \frac{\partial \vec{E}}{\partial x} + \frac{\partial \vec{F}}{\partial y} + \frac{\partial \vec{G}}{\partial z} = 0 \tag{4.5}$$

The first line of the vector equation corresponds to the continuity equation, the second, third and fourth line correspond to the equation of motion and the fifth line forms the equation of energy. The state value vector contains the values, which are to be conserved based on a volume, that means mass per volume, momentum per volume and energy per volume. The equations can be written as:

$$\vec{E} = \begin{pmatrix} \rho \cdot u \\ \rho \cdot u^2 + p - \tau_{xx} \\ \rho \cdot u \cdot v - \tau_{xy} \\ \rho \cdot u \cdot w - \tau_{xz} \\ (e+p) \cdot u - u \cdot \tau_{xx} - v \cdot \tau_{xy} - w \cdot \tau_{xz} + q_x \end{pmatrix} \tag{4.6}$$

$$\vec{F} = \begin{pmatrix} \rho \cdot v \\ \rho \cdot u \cdot v - \tau_{xy} \\ \rho \cdot v^2 + p - \tau_{yy} \\ \rho \cdot v \cdot w - \tau_{yz} \\ (e+p) \cdot v - u \cdot \tau_{xy} - v \cdot \tau_{yy} - w \cdot \tau_{yz} + q_y \end{pmatrix} \tag{4.7}$$

$$\vec{G} = \begin{pmatrix} \rho \cdot w \\ \rho \cdot u \cdot w - \tau_{xz} \\ \rho \cdot v \cdot w - \tau_{yz} \\ \rho \cdot w^2 + p - \tau_{zz} \\ (e+p) \cdot w - u \cdot \tau_{xz} - v \cdot \tau_{yz} - w \cdot \tau_{zz} + q_z \end{pmatrix} \tag{4.8}$$

With the viscous part of the stress tensor, which can be written in the following index notation in Cartesian coordinates:

$$\tau_{ij} = \mu \cdot (\frac{\partial u_i}{\partial x} + \frac{\partial u_j}{\partial xi} - \frac{2}{3}\frac{\partial u_k}{\partial x_k}\delta_{ij}) \tag{4.9}$$

and the Fourier equation:

$$q_i = \frac{c_p}{Pr} \cdot \mu \cdot \frac{\partial T}{\partial x_i} \tag{4.10}$$

in addition with the state equation and material values the system of equations is closed.

All turbulence models, which were used in this numerical analysis are based on time averaging of the Navier-Stokes equations. Every value of the flow field gets split in a time average value and a fluctuating value. The form of the basic equations can, therefore be conserved. As additional unknown quantities we get turbulent apparent stresses, turbulent heat flow and the kinetic energy of the turbulent fluctuations [6]. To close the time-averaged equation system, a turbulence model is needed.

4.3 Discretization Approaches

We refer to the continuous volume, where the flow shall be analysed, as domain. That domain gets replaced by a so called grid or mesh, which organizes the discrete points. We differentiate two kinds of meshes related to the connectivity between the mesh points. Either it is structured or unstructured. In structured meshes every point can be identified with three indices i,j,k, where every index represents a direction in 3-dimensional space. The points can be assigned to sharp lines of the mesh independently. Intersection points of the mesh lines are the final points. In unstructured meshes points are allocated randomly over the domain. Every point is connected to its neighbour point, which in most cases results in triangular surface partitions. The connection between nodes and elements is produced by an assignment matrix. With spatial discretization we mean the discretization of flow values and their derivatives concerning the coordinates x,y and z at a constant point in time t. Defining a mesh is a prerequisite. There are several methods of discretization, which are [3]:

- **Finite Difference Method**: The partial derivatives are replaced by difference quotients, which are based on the state values of the grid points. On every grid point the basic equations are approximately satisfied.
- **Finite Volume Method**: The differential equation gets integrated over the whole domain. For every cell of the mesh the volume integral of flows gets transformed in surface integrals, where the order of partial derivatives becomes reduced by one. The surface integrals are then expressed by the state values in the midpoint of the cell.
- **Finite Element Method**: The distribution of state values in the area between grid points is approximated by simple base functions. The basic equations are approximately satisfied by the method of weighted residuals (in most cases with the method of Galerkin).

A method is only entirely characterized by the definition of discretization in space and time. The software which was used in the present master thesis to make the numerical calculation is *ANSYS Fluent V14*. This software uses the Finite Volume Method, that is why a more detailed description will follow in the next section.

4.4 Finite Volume Method

The discretization takes place directly in the physical space, where the area of integration is divided into cells. These cells have a general geometrical structure with four, five or six lateral surfaces (tetrahedron, prism or hexahedron). In Figure 4.1 an example cell is shown.

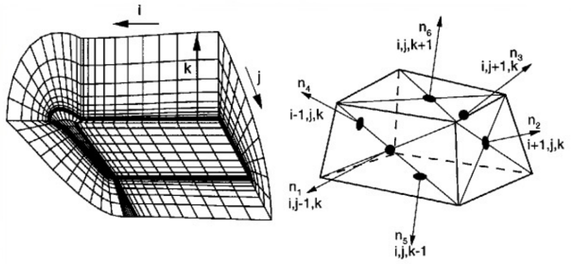

Figure 4.1: Finite Volume Cell

Initially, the basic equations get integrated over the whole volume of integration area V.

$$\frac{\partial}{\partial t}\int\limits_V \vec{U}\cdot dV + \int\limits_O \vec{E}\cdot dO + \int\limits_O \vec{F}\cdot dO + \int\limits_O \vec{G}\cdot dO = 0 \tag{4.11}$$

At the same time the Gauss' divergence theorem, which comes from the vector analysis, is applicable on all continuous functions, such as the components $\vec{E}$,$\vec{F}$ and $\vec{G}$ in our equations. The *Gauss' divergence theorem* is written as:

$$\int\limits_V (\nabla\cdot f)\cdot dV = \int\limits_O (f\cdot\vec{n}\cdot dO) \tag{4.12}$$

This theorem states, that the divergence of the vector function, on the inside of a control volume, is the same as the flows, which traverse the surfaces of that volume. O is the surface and $\vec{n}$ is the unit normal vector. The surface integral can, therefore be split in a sum of lateral surfaces of the volume. For every single cell the basic equation 4.11 is approximated.

The state values of the cell midpoint represent the state value vector. The discretization takes place in the cell midpoint. The equation 4.11 means, that the temporal change of the conservation values in every volume equals the flows traversing the surfaces of the volume. The Finite Volume Method makes use of the conservation property of the differential equations.

After successful discretization we get coupled ordinary differential equations in time for the discrete state values in every volume cell, which are solved with a time integration method. The advantage of the Finite Volume Method is, that it works better on complex geometries as the Finite Difference Method. Despite this, the formulation takes place directly in physical space.

4.5 Turbulence Modeling

In many technical flow problems we have to deal with a turbulent flow. Since a direct numerical simulation of turbulence is very costly and demands enormous amounts of computational effort, we are forced to model turbulence. The Navier-Stokes equations get time averaged and the additional terms of the Reynolds Shear Stress are represented by turbulence models. In most common models they are modeled by a turbulent viscosity, that is added to the viscosity of the fluid. Therefore the original form of the main equation is conserved.

There are inherently different approaches for modeling turbulence, that can be classified as follows [1]:

- **Algebraic Models**, that are also called Zero Equation Models. They do not possess differential equations, instead they consist of algebraic equations to form turbulent viscosity and a turbulent Prandtl number, which is added to the laminar quantities.
- **One Equation Models**, that contain one additional transport equation for a turbulent quantity.
- **Two Equation Models**, that contain two additional equations. The most popular ones solve one equation for turbulent kinetic energy and a second one for dissipation rate (k-ϵ model) or a frequency (k-ω model).
- **Reynolds Shear Stress Models**, that contain a transport equation for every component of the stress tensor.

The first three models are denoted as Eddy Viscosity Models, because they approximate the Reynolds Stresses with the following approach:

$$\rho \cdot \overline{u_i^{'} \cdot u_j^{'}} = \mu_t(\frac{\partial \overline{u_i}}{\partial x_j} + \frac{\partial \overline{u_j}}{\partial x_i} - \frac{2}{3}\frac{\partial \overline{u_k}}{\partial x_k}\delta_{ij}) \tag{4.13}$$

The quantity of μ_t is the turbulent viscosity or eddy viscosity. This formulation is analogous to the friction law of Stokes in laminar flows, therefore it eases the implementation of the model into the main equations and finally in the calculating software. The eddy viscosity describes the diffusive momentum transport, which is caused by the small scaled eddy motions and gets simply added to the laminar viscosity. The eddy viscosity is not a constant. Following Table 4.1 gives an idea of the turbulence models included in the ANSYS Fluent software package. For further detailed information on turbulence models [11] is recommended.

Table 4.1: Description of turbulence and wall model

Model	***Description***
Spalart-Allmaras	A transport equation for modeling the modified turbulent viscosity.
Standard k-ϵ	Standard models for industry; Solution of two transport equations for k and ϵ. Application of empirical constants, which are valid only for developed turbulent flow.
RNG k-ϵ	Variation of the k-ϵ model. Equation and constants are derived analytically. Application of a clearly modified equation for ϵ.
Realizable k-ϵ	Variation of the k-ϵ model. "Realizability":Taking several mathematical demands into consideration.
Reynolds Stress	Direct solution of Reynolds Shear Stresses with transport equations; Takes the anisotropy of turbulence into account.
Standard Wall Model	The viscosity dominated boundary layer is not resolved. The mesh near the wall is coarse ($y^+ = 30$ to 300). The information for the cell midpoint of the first cell is calculated from a derived wall function.
Non-Equilibrium Wall Treatment	It considers the pressure gradient for simulation of flows with pressure gradient or recirculation. Two layer model; Splitting the boundary layer in a near wall cell, which is viscous and a full turbulent region, separate calculation of τ_w, k and ϵ. Assumption that production and dissipation is in balance.

5 Mesh Generation

Normally, mesh generation is categorized under the pre-processing phase of a numerical analysis, which will be subject of the following chapter. Since, in the case of the present thesis the mesh generation was a major part, an own chapter was devoted to it.

5.1 Mesh Varieties

The mesh demands some characteristics, which have to be taken into account in the process of generation, otherwise the results of the numerical analysis will not be satisfying. It is of great importance to consider the angle ratio and the skewness of the cells to guarantee a high mesh quality. Also, a crucial criterion of obtaining high quality results, is the refinement of near wall regions. These cells would not be accepted in the main flow, because of their huge aspect ratio, but in the near wall region, they are decisive for the simulation of frictional resistance and flow separation. Boundary layer cells are also required, if complex "wall models" are used. With the term wall model we normally mean a calculation model for describing the behaviour of the boundary layer.

Figure 5.1 shows some elements, which are commonly used for mesh generation. Hexahedron and prism elements have the advantage of being more economical in Random Access Memory(RAM) usage for calculation. These meshes also provide a better convergence behaviour. These reasons were decisive for using such elements in the case of the mixing chamber. Grids consisting of tetrahedron elements have the advantage, that the meshing of a complex geometry is quite easy. Disadvantages are the increased usage of RAM for calculation and the insufficient resolution of the boundary layer.

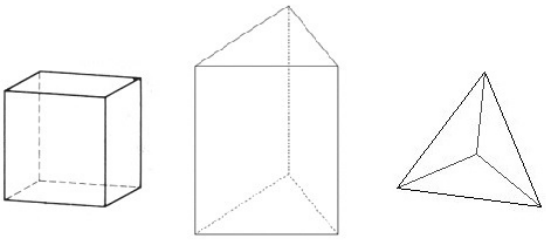

Figure 5.1: Geometrical elements: Hexahedron, Prism, Tetrahedron

The following Figure 5.2 shows the typical grid topologies for structured meshes with a solid zone, which gained acceptance. This is of great importance to get a general knowledge on how a mesh has to be built. In the present work O-grid topologies were used to mesh the various domains of the chamber, which contain solid zones. The mesh has to be generated around these zones.

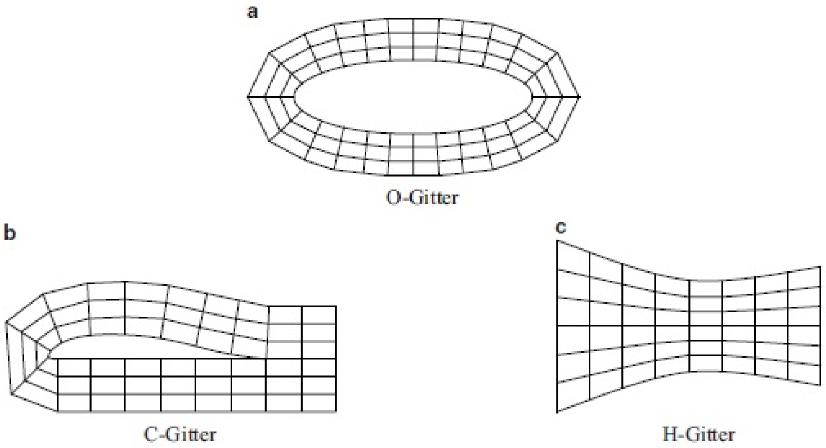

Figure 5.2: Topology of solid adapted, structured grids

5.2 Introducing the Geometry

Following figures will illustrate the geometry of the mixing chamber with all interior parts and will point out, how the complete domain was split in partitions, in order to control the meshing process. This chamber was modelled by the commercial CAD-Software*CATIA* and is a welded construction. Figure 5.3 shows the outside of the mixing chamber.

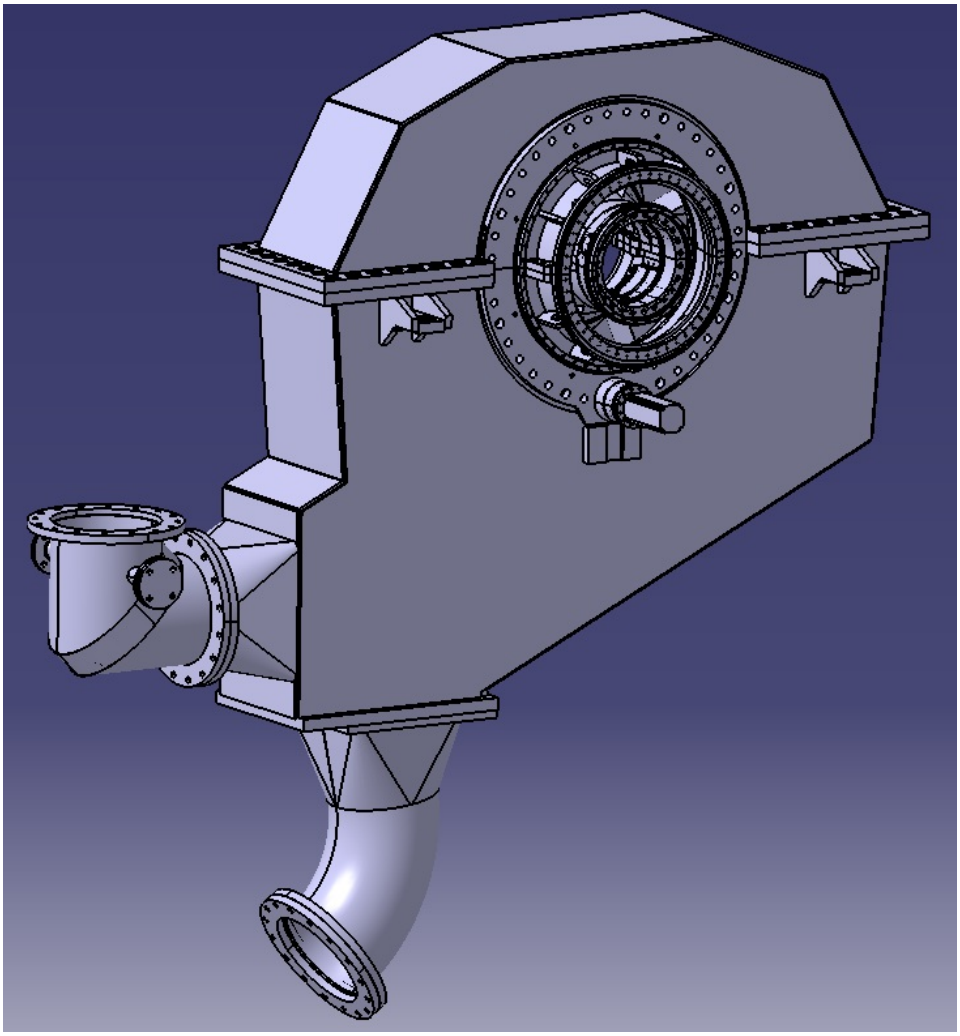

Figure 5.3: Geometry of mixing chamber

In Figure 5.4 we see, that the domain of the chamber has two Inlets called Inlet SC and Inlet GHH. After leaving these inlet domains the fluids reach the Mixer partition. The actual mixture of the two pressurized air flows starts at the outlet planes of this partition. At one plane the Mixer is connected to the Mixing Zone and on the other plane it has an interface to the Tandem Cascade. After leaving the Tandem Cascade the fluid enters a domain, which is called Lower Casing and reaches to the middle of the flange, were the next partition called Upper Casing is connected. Finally, the fluid reaches the Annulus partition, where it leaves the chamber and comes to the inlet plane of the turbine (see Figure 5.4).

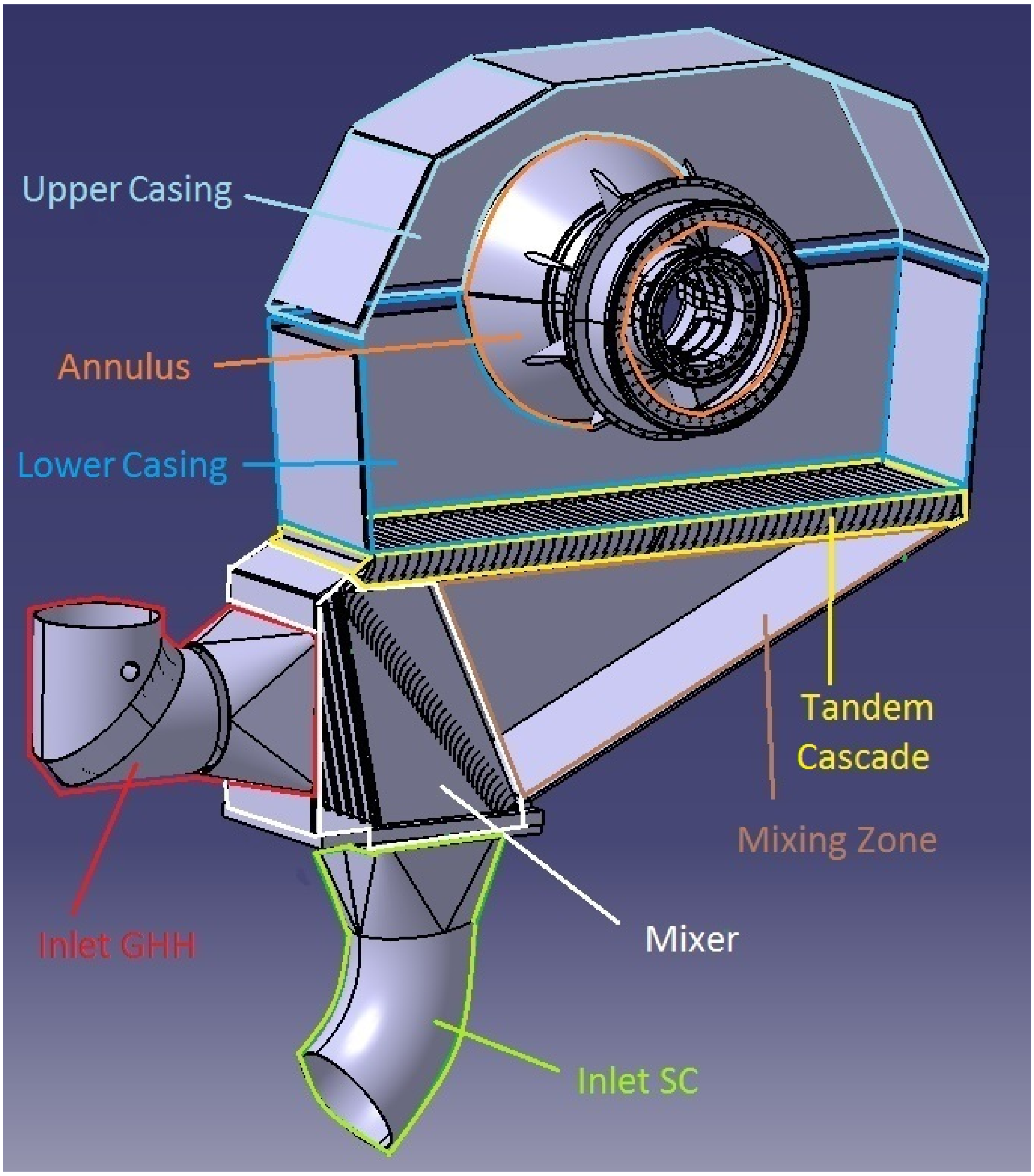

Figure 5.4: Interior geometry of mixing chamber with different flow domains

- **Inlet SC and Inlet GHH**
  The first inlet domain of the chamber called Inlet SC, where pressurized air comes from the supply pipe of the compressor station in the basement will be split in two partitions. The first one will be called SC1 and is an elbow pipe part. The second one is called SC2 and is a funnel part. The inlet of this part is circular in cross section and the outlet is rectangular with edges rounded off, as shown in Figure 5.5.

  The second inlet domain called Inlet GHH, where air is provided by the brake compressor, stationed in the test hall, will be split in four partitions named GHH1, GHH2, GHH3 and GHH4. GHH1 and GHH3 are angularly cut pipe parts. GHH2 is a cylinder part, containing a row of guiding vanes. The GHH4 part is a funnel part, where the inlet cross section is cirular and the outlet is rectangular with edges rounded off, similar to SC2 (see Figure 5.5).

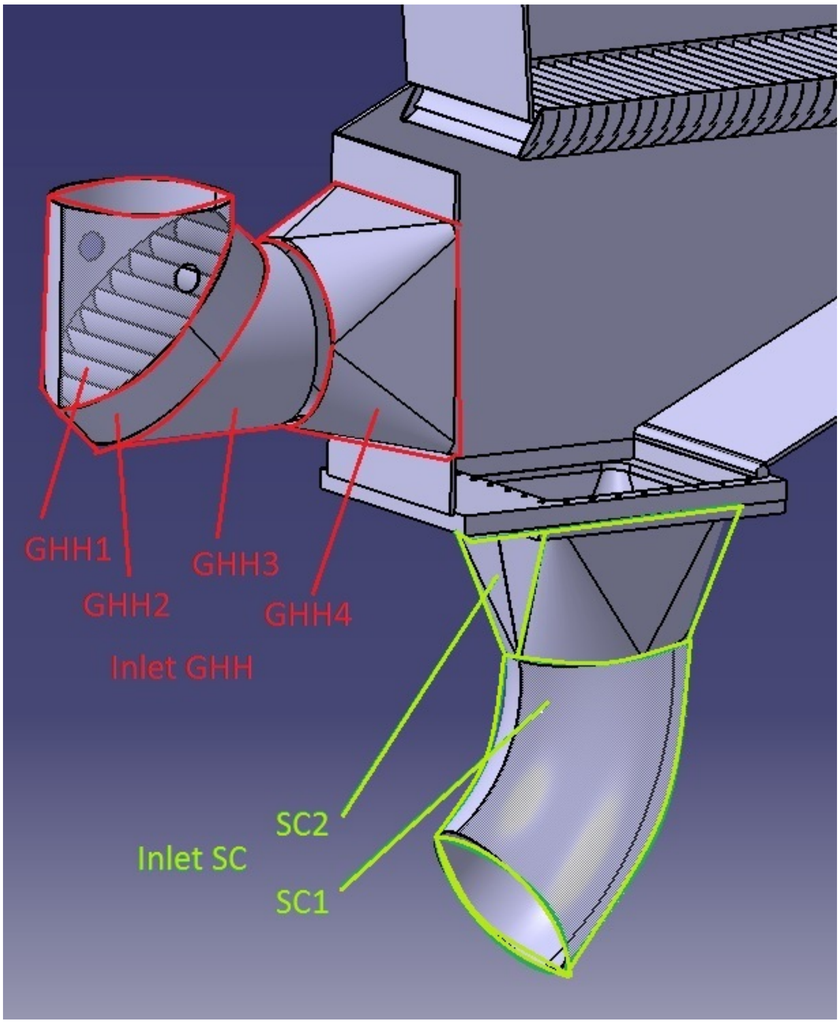

Figure 5.5: Partitions of inlet domains

- **Mixer**
  This domain is very complex, because the air coming from Inlet SC faces 8 separate channels, where the two side channels are narrower than the middle ones. In addition, the flow encounters a diagonal blade row for the purpose of deflection. This part of the domain was captured with six different mesh partitions. First one is called Main IN and builds a prism part in front of the guiding vanes. For the narrower side channels this partition is called Side IN. The second partition is the vane row called Main Blades and again another partition is needed for side channels, which is called Side Blades. The prism domain followed by the guiding vane row is called Main OUT and Side OUT for the narrower side channels (see Figure 5.6).

  From the other side, the pressurized air coming from the GHH brake compressor encounters a domain called Preblock followed by a partition named Block. After leaving this domain the fluid flows through seven similar channels with partition name Channel, as shown in Figure 5.7.

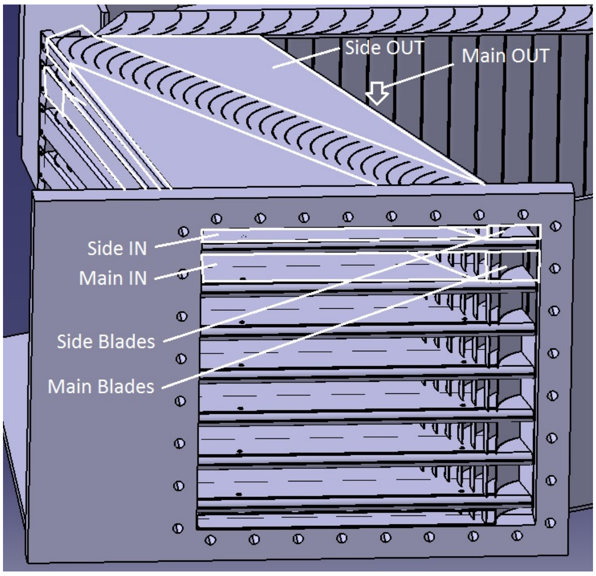

Figure 5.6: Partitions of Mixer from SC side

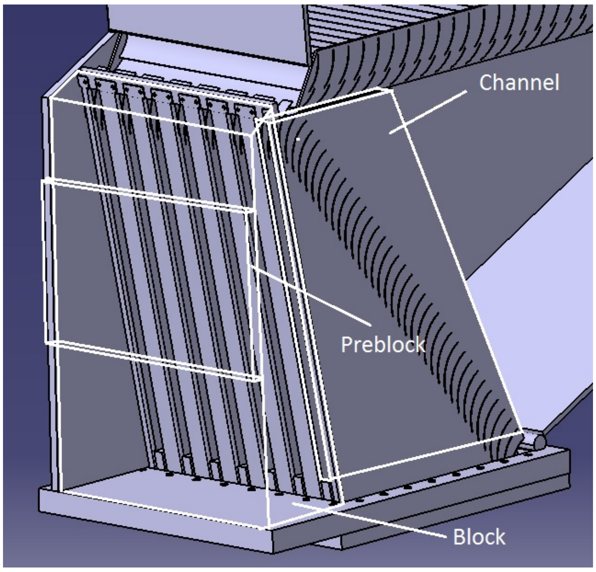

Figure 5.7: Partitions of Mixer from GHH side

- **Mixing Zone, Tandem Cascade, Lower Casing and Upper Casing**
  These domains were not split, but each was treated as one mesh block.

- **Annulus**
  A 45° segment of the mesh was constructed. The red cylinder in Figure 5.8 is the interface between the Annulus, the Under and Upper Casing partitions. Here, the fluid enters the domain of the Annulus to flow through the passage with blades and finally leave the domain, indicated by the yellow arrows and lines in Figure 5.8.

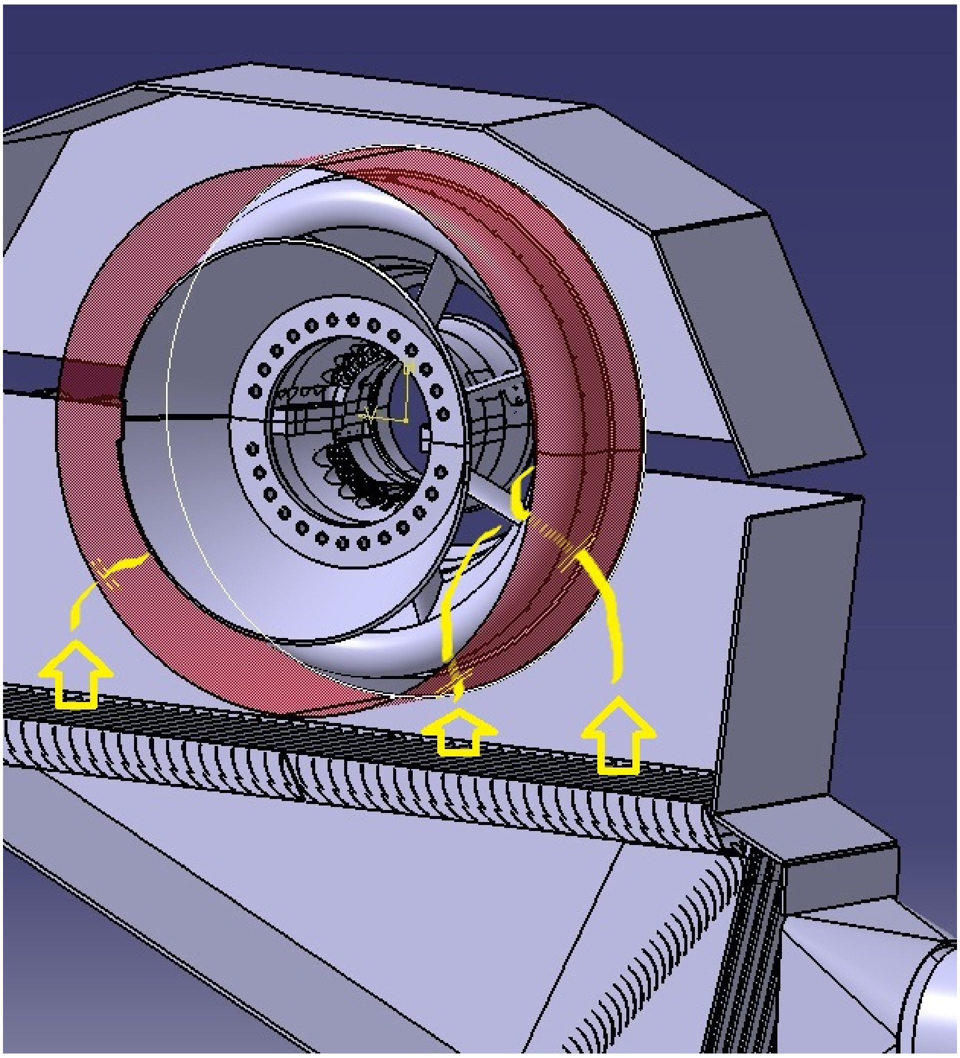

Figure 5.8: Domain of annulus

There are several geometrical simplifications, which are necessary to ensure, that a mesh can be generated.

5.3 Geometrical Simplifications

In the present work the software *ANSYS ICEMcfd V13* was used to create the partitions of the computational mesh. It is of great importance to follow a hierarchy the software proposes. On one hand, it reduces the possibilities of confusion and on the other hand, one can obtain results more quickly. Figure 5.9 shows the hierarchy of the program by simply looking at the user interface.

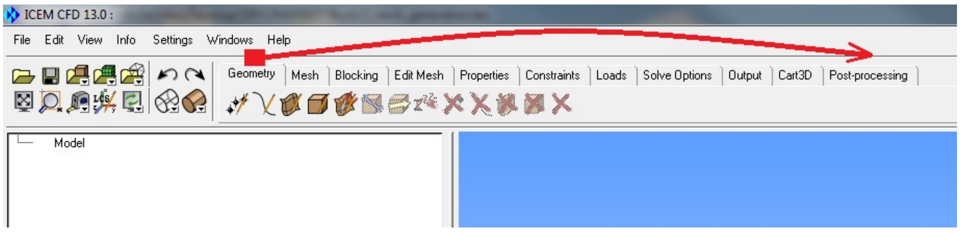

Figure 5.9: Hierarchy ANSYS ICEMcfd

This is the proposed order things have to be done. First we create or adapt the geometrical elements like points, curves and surfaces, then we have all we need to make associations of vertices and edges with the desired geometrical elements.
In general, all outer surfaces, curves and points were deleted, because only the interior domain is of interest and interfaces were created at places, where the different domains are connected to get a completely closed domain, otherwise the mesh generating program will not recognize the desired domain. An important target is to keep the geometry as correct as possible to simulate reality. But in some cases compromises are necessary. The following passage will give an overview of geometrical simplifications in different domains.

- **Inlet SC**:
  No simplifications were made.

- **Inlet GHH**:
  - In the first partition called GHH1, there are two holes modelled in CAD, these were closed.
  - The existing flange between GHH3 and GHH4 was deleted and replaced by a cylinder surface to close the domain. This was necessary for obtaining a better mesh, due to the different diameter of the inner surface of the flange and the pipe.

- **Mixer**:

The mixing process starts by the time the two air flows of different properties reach the interface to the Mixing Zone and to the upright Tandem Cascade. The CAD model is similar with the only difference, that the mixing of fluids starts already at the top of the part inside the domain, otherwise channel and tandem cascade parts would touch. The white mark in Figure 5.10 indicates the edges. These gaps were closed with surfaces, otherwise it would be impossible to generate the mesh.

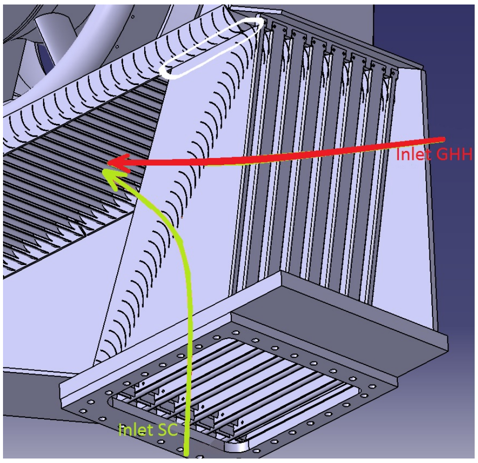

Figure 5.10: Flow of fluids in diagonal blade rows part

The leading edges of Channel parts were modified from a curve to an angular shaped structure, to get a plane surface for the interface.

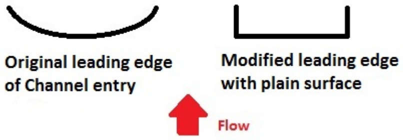

Figure 5.11: Leading edge of channel

- **Mixing Zone**:
  No simplifications were made.

- **Tandem Cascade**:
  - The tandem cascade consists of two identical parts as shown in Figure 5.8. It was treated as on piece in the present analysis.
  - On both sides some additional surfaces were integrated to guarantee a closed domain.

- **Lower Casing** and **Upper Casing**:
  The flange was deleted and the emerged gap was closed with plain surfaces, otherwise the mesh would have to bend around an edge, similar to the problem already encountered in Inlet GHH3.

- **Annulus**:
  No simplifications were made.

At that point the geometry is ready for starting the blocking procedure, which will be discussed in the next section.

5.4 Blocking Tactics and Mesh Partitions

In *ANSYS ICEMcfd* the basic idea of creating a mesh for a certain domain is to place blocks into it, which gives control over the various edges of the blocks. With them, it is possible later on to define the number of nodes and the distribution, that is desired. We can either create a simple block or an O-grid block. The O-grid block has the advantage, that refining the mesh in the near wall regions is simple. The disadvantage is, that for complex geometries the handling often gets difficult. In these situations, we can achieve our target more easily by using a simple block and adjust edge parameters afterwards. For further information on Blocking look up the *ANSYS ICEMcfd* Documentation.

The major step, which has to be taken is to inform the program, how the domain looks like. This can be achieved by *associations*. Vertices and edges can be associated to every geometrical element the program knows. Now it is obvious, that we need all geometrical elements necessary to obtain a solution. In particular cases, it is quite difficult to create an acceptable mesh, especially when a singularity point is part of the geometry, always in connection with a quadrilateral (block). For better understanding an example will help.

When we think of a quadrilateral we have four corner points, but if our geometry has a triangular structure, we somehow have to merge two corner points, otherwise it will not pe possible to obtain a block for this geometrical structure. When we perform this in *ANSYS ICEMcfd* the program still tries to find a quadrilateral, although two corner points were merged. This results in a singularity as part of the mesh structure, where all lines originate from one point. This is an undesired effect, because the cells of the grid get completely skewed, till they become one single point. Of course there is a solution to that problem, one has to think of, how the current geometry can be split in smaller quadrilateral domains.

For domains, which consist of many equal parts, such as the blade rows,*ANSYS ICEMcfd* provides the possibility of transforming the blocks. That means, we have to create the blocking for one segment and copy it by giving reference points, either translational or rotational. Here again, it is of great importance to first translate all the geometrical elements needed for associations, only then, this method will work. The following figures will illustrate the blocking and the resulting mesh on every partition. The exact position of different parts, can be checked in Figures 5.4, 5.5, 5.6 and 5.7. Besides the blocking and mesh of the partitions and indication figure is added to locate the actual part in the geometry of the chamber. A red rhombus indicates the position of the part presented. In addition, the mesh parameters of every partition are included. These parameters give information about how many nodes, quadrilateral or hexahedral cells form the actual partition.

Figure 5.12 shows the O-grid block applied in SC1 mesh partition of Inlet SC. This elbow pipe part is located at the lower end of the mixing chamber and provides the pressurized air from the compressor station located in the basement of the institute. The node distribution was refined at the wall see Figure 5.13.

Figure 5.14 illustrates the blocking of SC2, which is located downstream, right after SC1 and is a funnel part. This O-grid block was additionally split at the rectangular side, to avoid very skewed cells in this area, because this funnel part is cut angularly. The achieved mesh is shown in Figure 5.14.

The blocking structure of GHH1, which is the first angularly cut pipe part of Inlet GHH is shown in Figure 5.16 and is located on the left, where air is provided from GHH brake compressor in the test hall. Figure 5.17 shows the node distribution with refined region at the wall.

Figure 5.18 shows the blocking of part GHH2, which is positioned right after part GHH1 downstream. Here, an ordinary block was split 18 times in flow direction to capture the geometry of the guiding vanes and the interior domain between them. The block was also split vertically to flow direction to capture the edges. Finally, two splits were performed at each leading edge of the vanes to achieve a fine resolution in these areas. Figure 5.19 presents the result of the mesh for GHH2 partition.

Figure 5.20 shows the blocking of GHH3, which is identical to the GHH1 partition. The resulting mesh is presented in Figure 5.21. This part is located downstream after GHH2.

The O-grid block of GHH4 is shown in Figure 5.22. It is similar to the funnel part SC2 of Inlet SC with the difference, that the geometry did not demand an additional split at the rectangular side, because this funnel part is straight there. The mesh with the refined wall region is presented in Figure 5.23.

Figure 5.24 shows the O-grid block applied in the Preblock part. The resulting mesh is shown in Figure 5.25 with refinement at the wall.

The blocking of the partition called Block is illustrated in Figure 5.26. Here, an O-grid block was made for the center part where two ordinary side blocks were extruded. The mesh is shown in Figure 5.27.

In Channel partition of the Mixer an O-grid block was applied with an extruded block for the upper side. This blocking was transformed to all channels with near wall regions being refined as it is shown in Figure 5.28.

The blocking structure of Side IN part is the same as in Main IN part shown in Figures 5.30 and 5.32. The meshes resulting are presented in Figure 5.31 for the Side IN partition. Important to notice, that the skewness of cells is acceptable. The near wall region was refined. Same observations can be made for the mesh of Main IN shown in Figure 5.33.

The blocking of the guiding vanes of the Mixer is shown in Figures 5.34 for the Side Blades part and 5.36 for the Main Blades partition. An O-grid was applied around the blade with subsequent extrusion of blocks to capture the remaining space of the interior domain. The advantage of this method is, that the distribution of nodes around the blade can be controlled separately to the one of the remaining space. The resulting meshes are shown in Figures 5.35 for the Side Blades part and 5.37 for the Main Blades partition.

Figures 5.38 and 5.40 show the blocking structure of the Side OUT and the Main OUT partitions. The geometry is similar to Side IN and Main IN parts, therefore the blocking tactic is the same. The meshes with refined near wall regions produced for Side OUT and Main OUT are presented in Figures 5.39 and 5.41.

The same procedure as in the other prism domains was performed in the blocking for the Mixing Zone part. Here an additional split was needed at the interface connecting the Mixer part to prevent skewed cells, because the geometry has an additional edge in the lower region. The mesh is illustrated in Figure 5.43.

Around the blades of the Tandem Cascade partition O-grid blocks were applied. The remaining spaces were captured with extruded blocks. The region where the two blades overlap needs to have an additional block, otherwise the distribution of nodes is not controllable. Figure 5.44 shows the blocking and Figure 5.45 shows the achieved mesh for the Tandem Cascade partition.

Figure 5.46 shows the blocking for Lower Casing part. The resulting mesh was refined in the near wall regions as illustrated in Figure 5.47.

The Upper Casing part is presented in Figure 5.48. Here, the regions near the wall were also refined. Figure 5.49 shows the generated mesh.

The blocking of the Annulus part was made of ordinary blocks, apart from the region around the blades, where an O-grid block was applied. A segment of 45 degrees was generated. The cells around the blade were refined. Figure 5.50 shows the blocking and Figure 5.51 the resulting mesh for the Annulus partition.

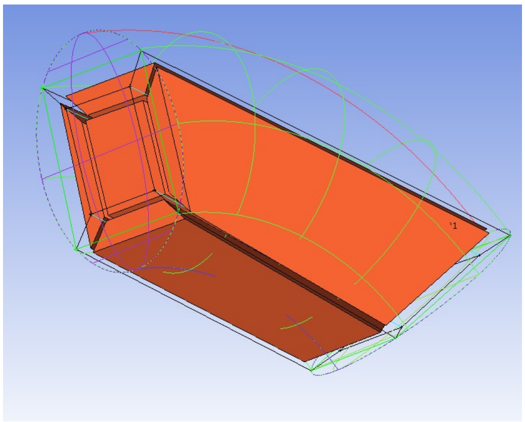

Figure 5.12: Blocking of SC1

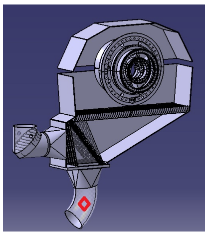

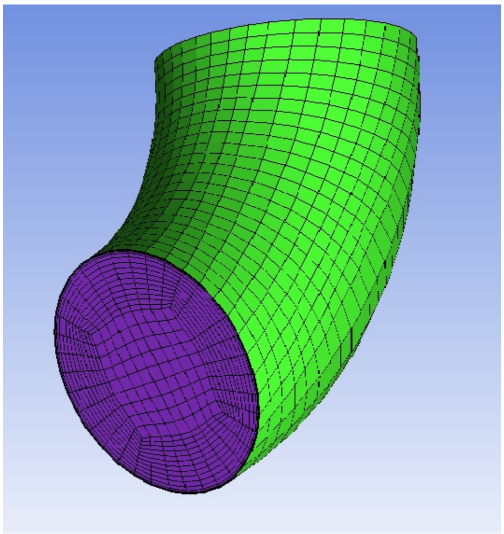

Figure 5.13: Mesh of SC1

nodes	16000
quads	2106
hexas	14904

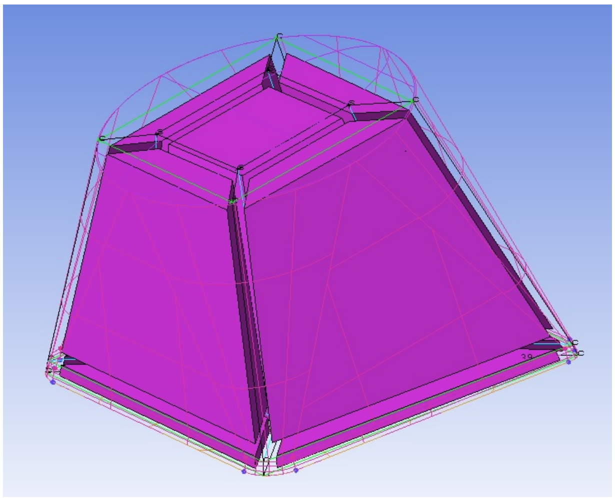

Figure 5.14: Blocking of SC2

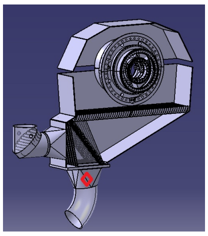

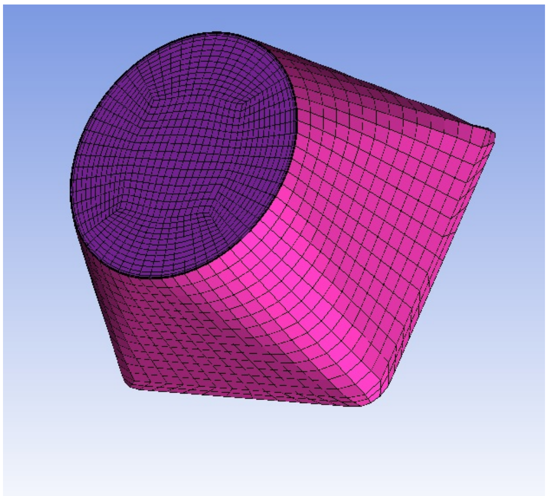

Figure 5.15: Mesh of SC2

nodes	19652
quads	3210
hexas	18000

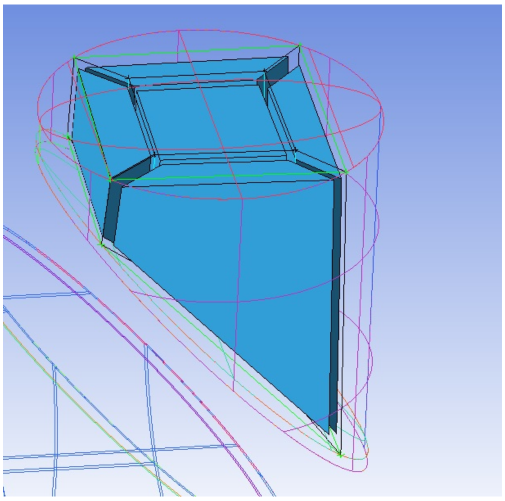

Figure 5.16: Blocking of GHH1

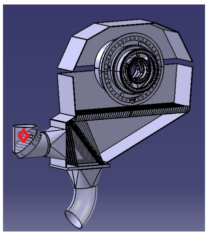

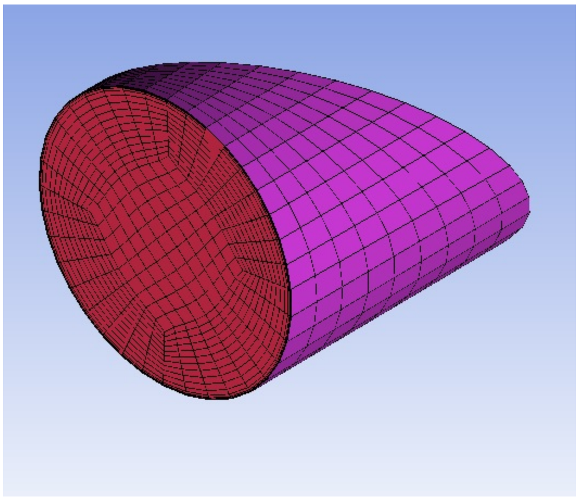

Figure 5.17: Mesh of GHH1

nodes	6400
quads	1566
hexas	5589

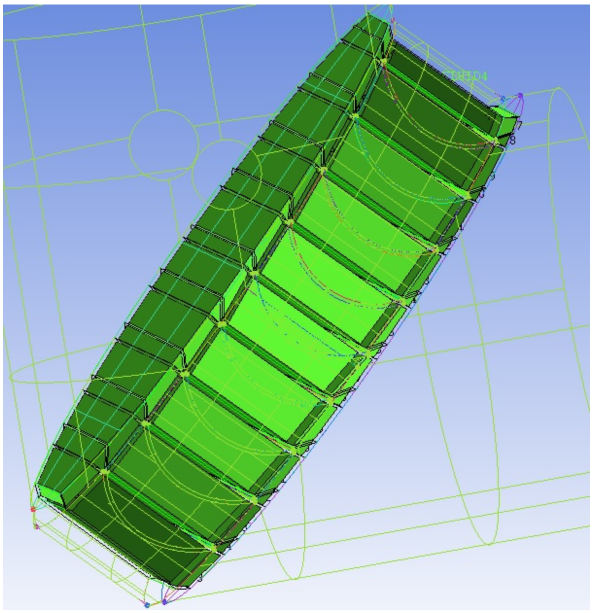

Figure 5.18: Blocking of GHH2

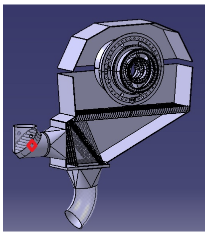

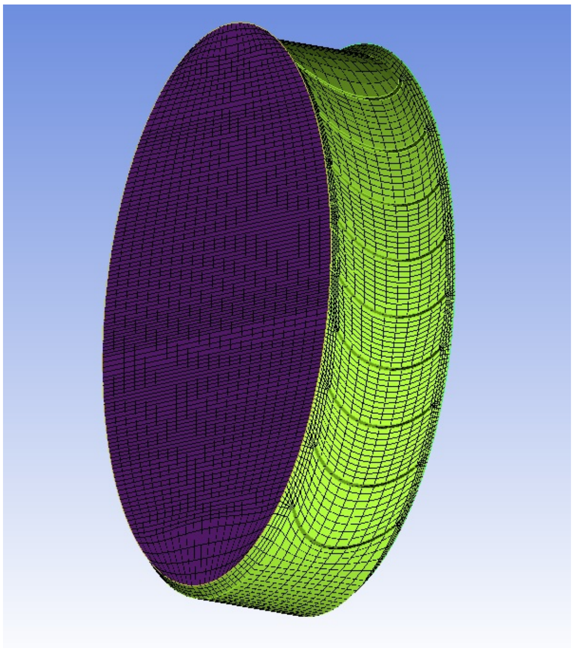

Figure 5.19: Mesh of GHH2

nodes	49500
quads	15676
hexas	41559

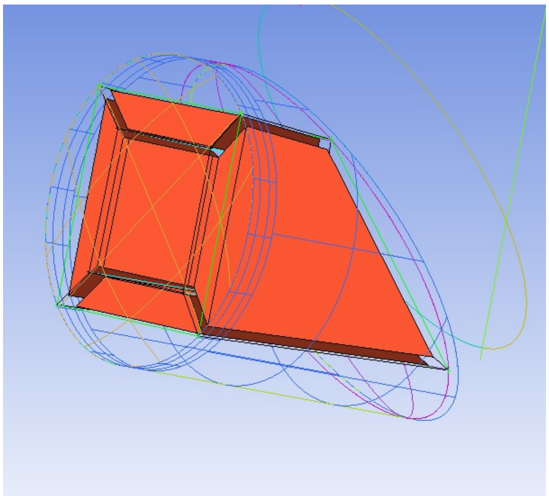

Figure 5.20: Blocking of GHH3

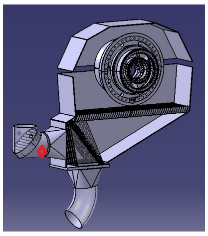

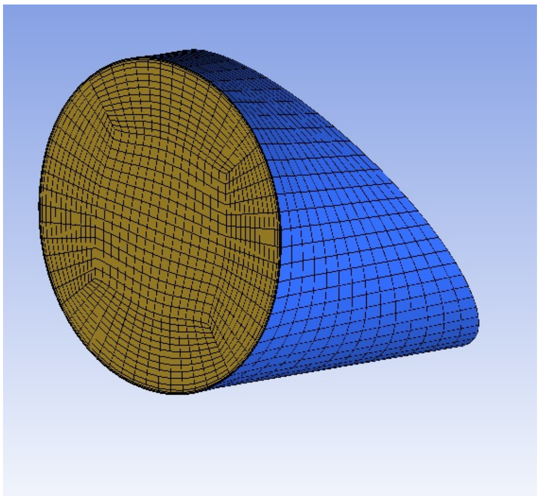

Figure 5.21: Mesh of GHH3

nodes	17340
quads	3090
hexas	15750

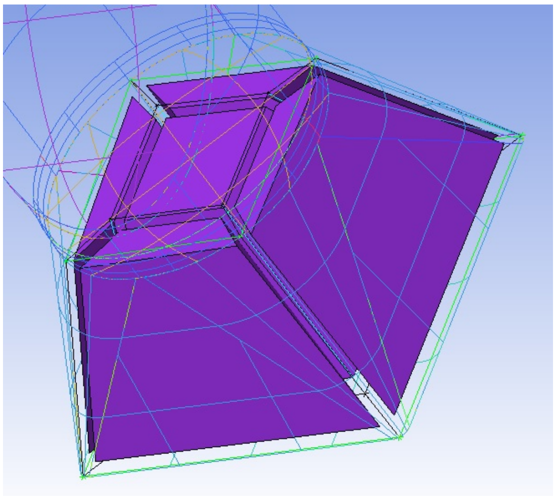

Figure 5.22: Blocking of GHH4

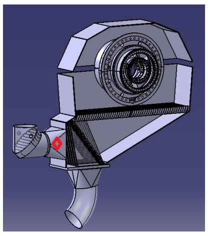

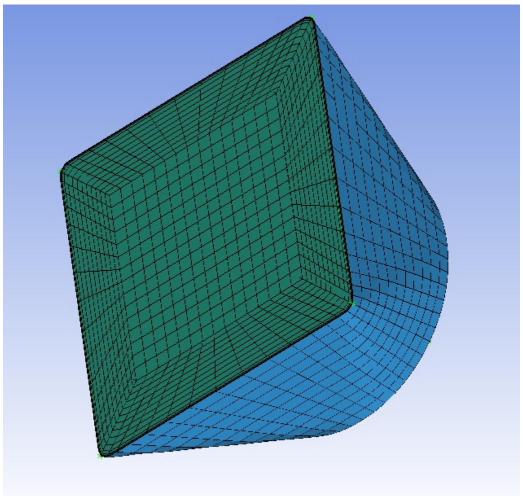

Figure 5.23: Mesh of GHH4

nodes	13872
quads	2916
hexas	12375

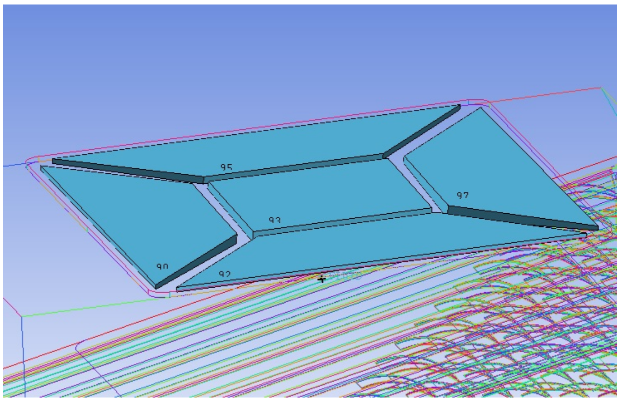

Figure 5.24: Blocking of Preblock

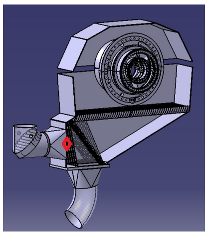

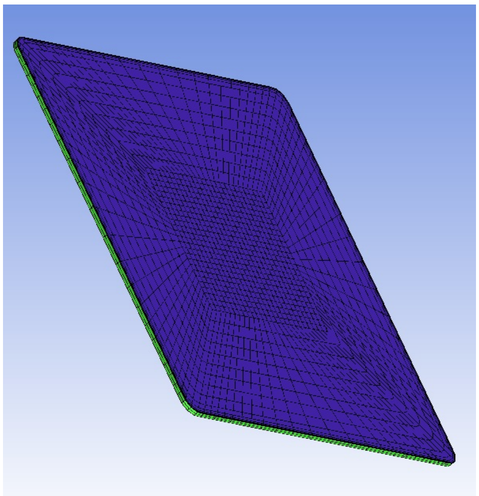

Figure 5.25: Mesh of Preblock

nodes	6528
quads	4450
hexas	4250

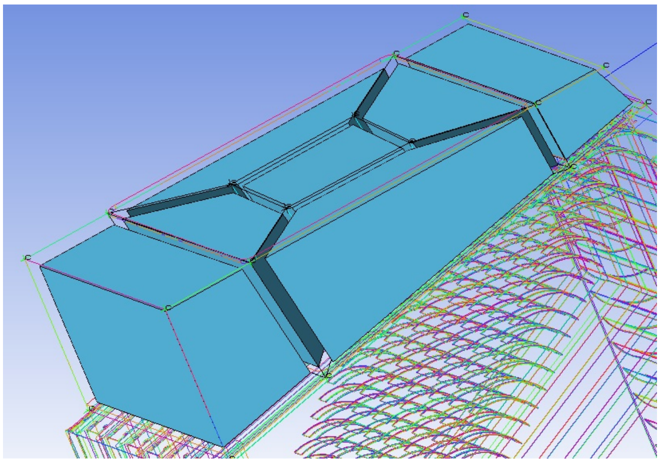

Figure 5.26: Blocking of Block

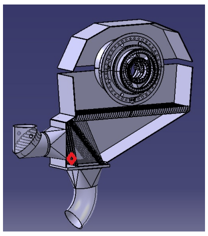

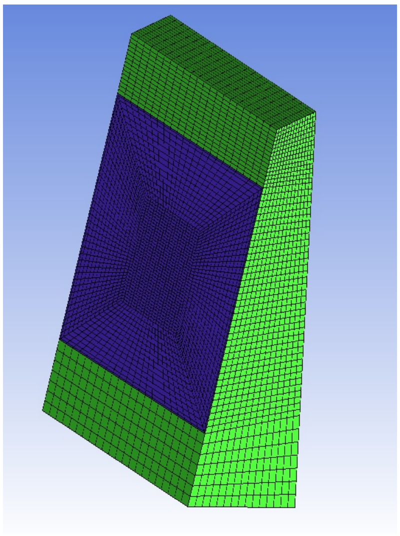

Figure 5.27: Mesh of Block

nodes	50400
quads	8566
hexas	46020

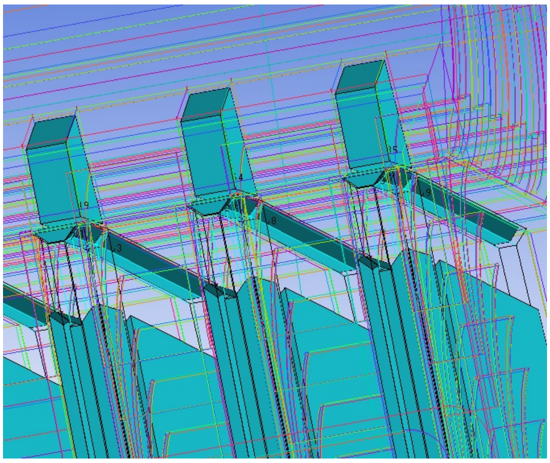

Figure 5.28: Blocking of Channels

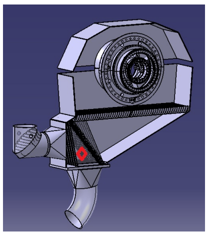

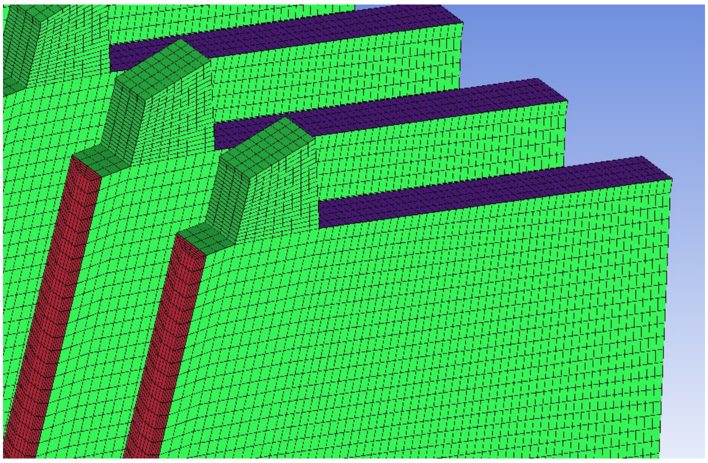

Figure 5.29: Mesh of Channels

nodes	670670
quads	111384
hexas	613690

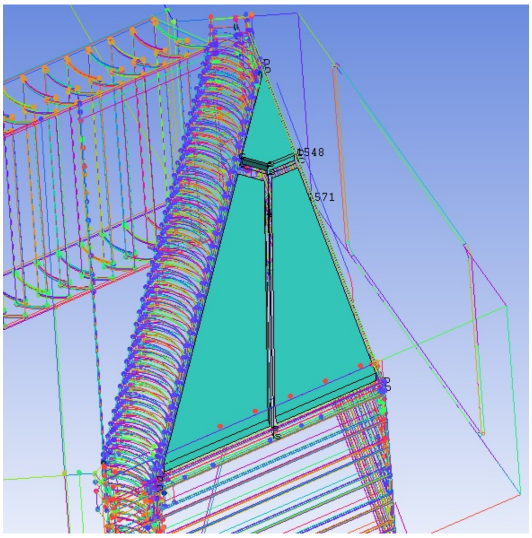

Figure 5.30: Blocking of Side IN

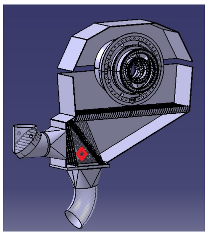

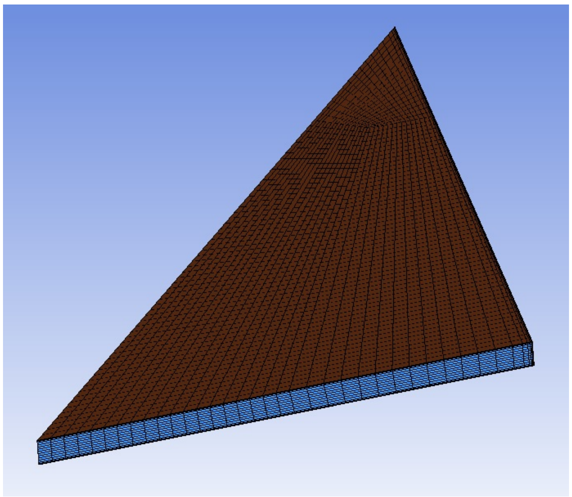

Figure 5.31: Mesh of Side IN

nodes	43216
quads	8116
hexas	39045

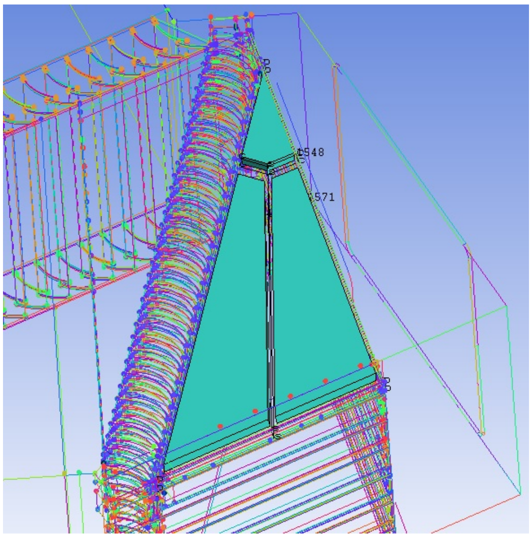

Figure 5.32: Blocking of Main IN

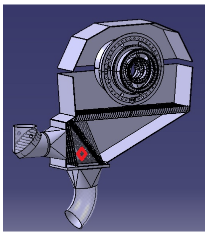

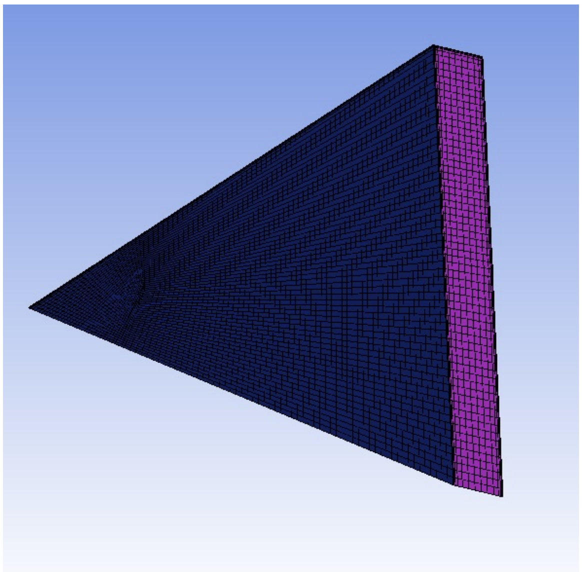

Figure 5.33: Mesh of Main IN

nodes	78640
quads	13272
hexas	71865

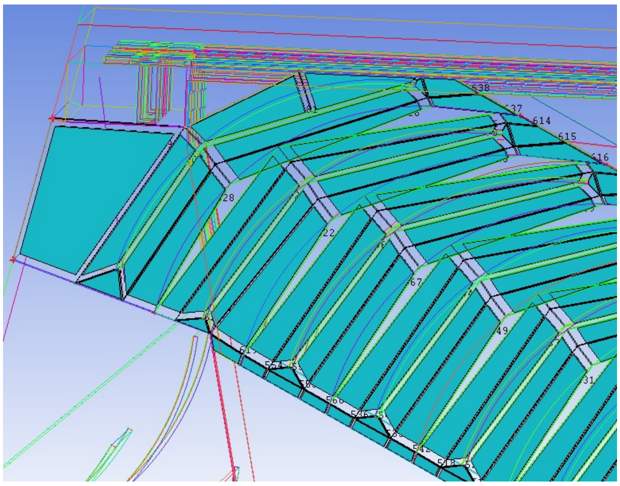

Figure 5.34: Blocking of Side Blades

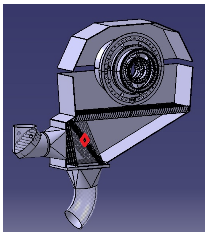

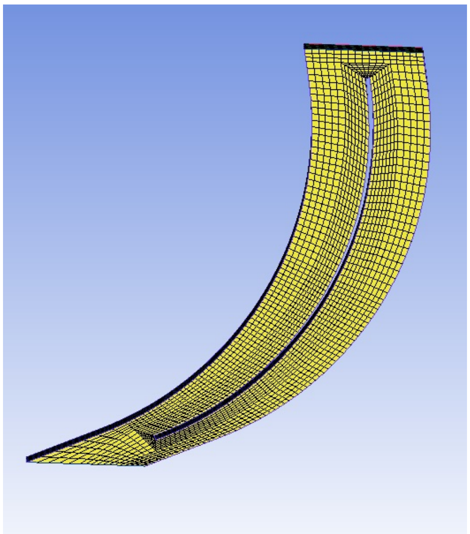

Figure 5.35: Mesh of Side Blades

nodes	23592
quads	7816
hexas	19484

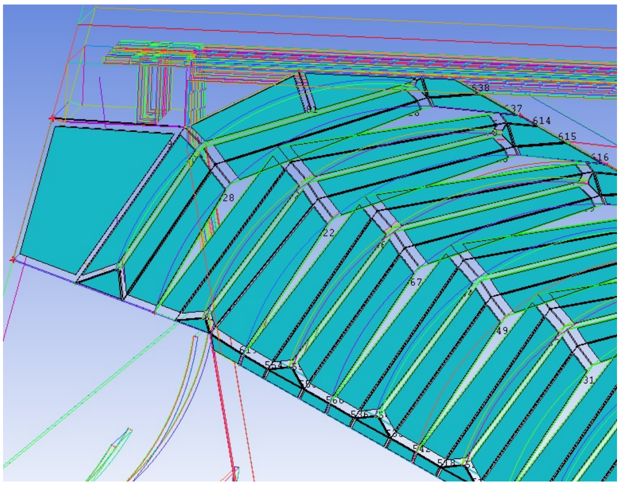

Figure 5.36: Blocking of Main Blades

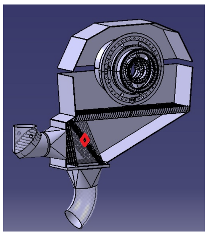

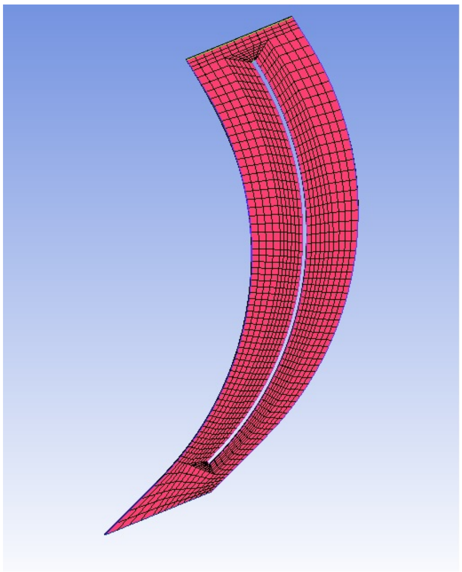

Figure 5.37: Mesh of Main Blades

nodes	12376
quads	4882
hexas	9786

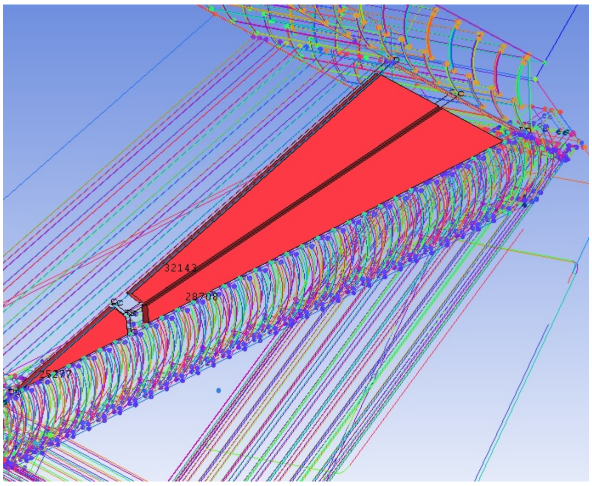

Figure 5.38: Blocking of Side OUT

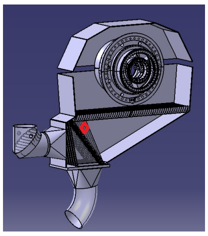

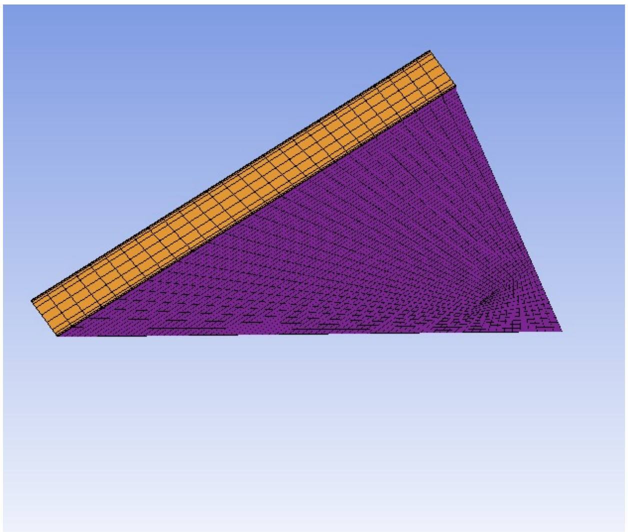

Figure 5.39: Mesh of Side OUT

nodes	23232
quads	5610
hexas	20328

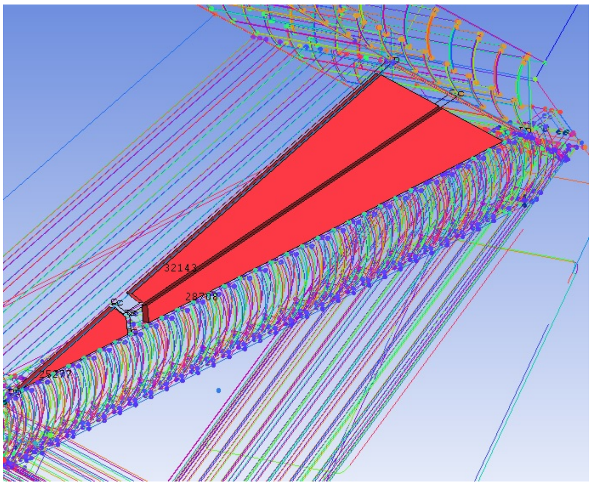

Figure 5.40: Blocking of Main OUT

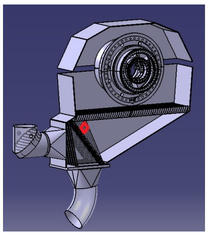

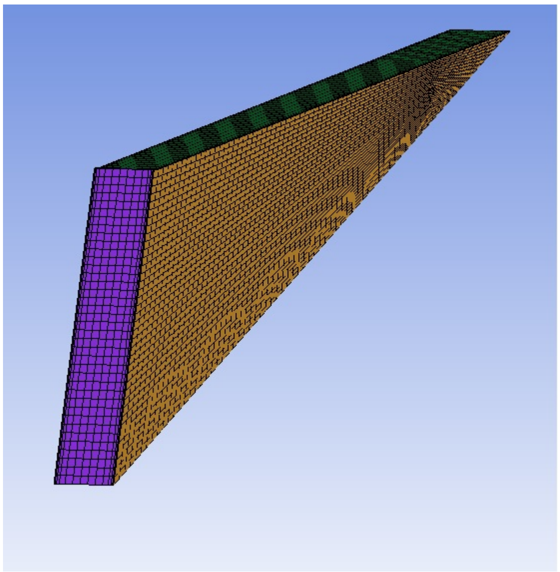

Figure 5.41: Mesh of Main OUT

nodes	43216
quads	8116
hexas	39045

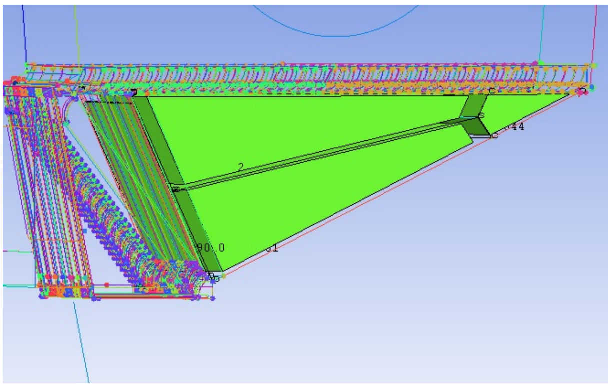

Figure 5.42: Blocking of Mixing Zone

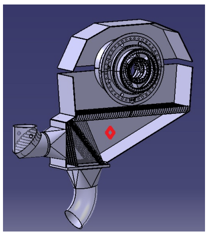

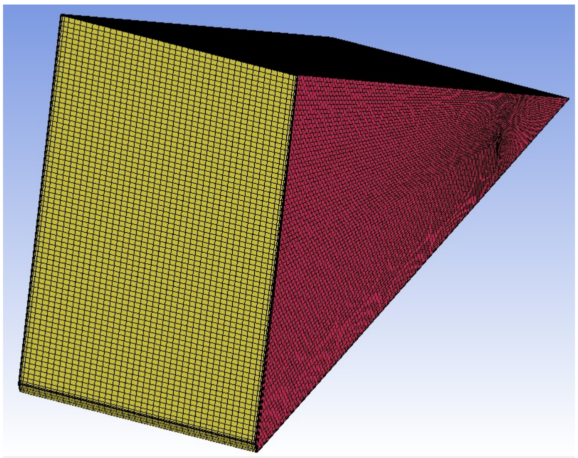

Figure 5.43: Mesh of Mixing Zone

nodes	561900
quads	41674
hexas	540813

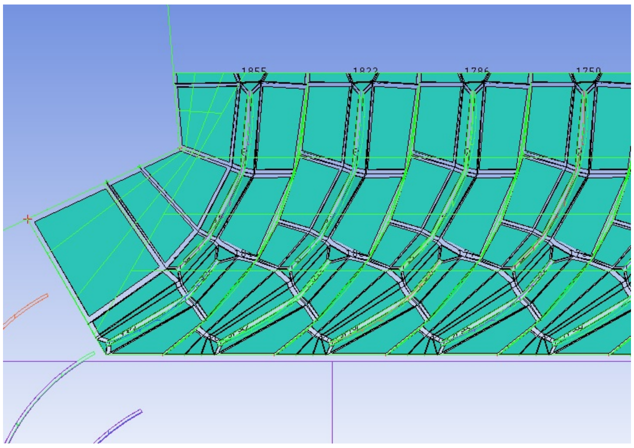

Figure 5.44: Blocking of Tandem Cascade

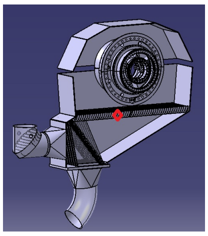

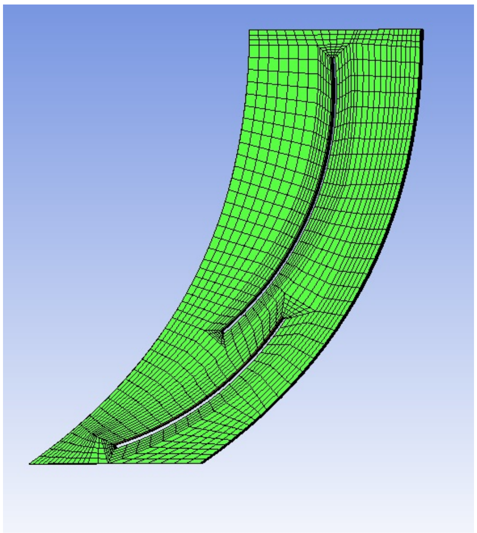

Figure 5.45: Mesh of Tandem Cascade

nodes	7105120
quads	1159076
hexas	6752288

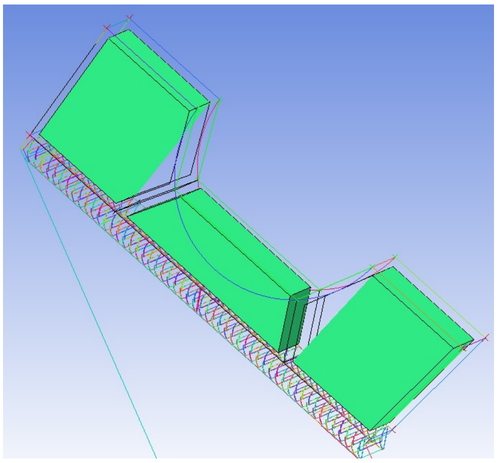

Figure 5.46: Blocking of Lower Casing

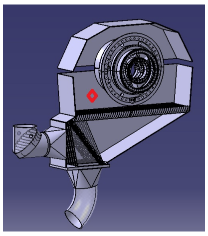

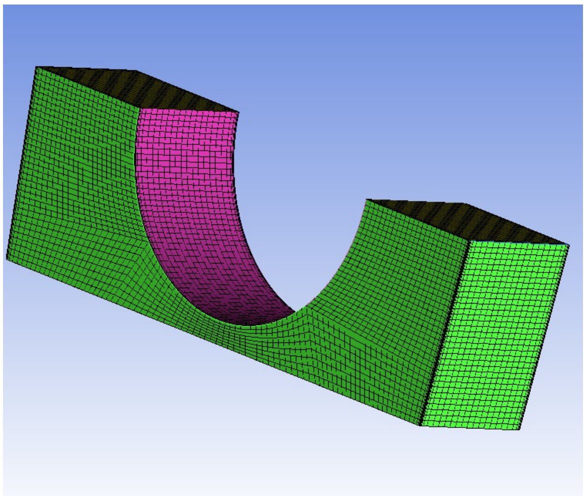

Figure 5.47: Mesh of Lower Casing

nodes	71400
quads	13158
hexas	64641

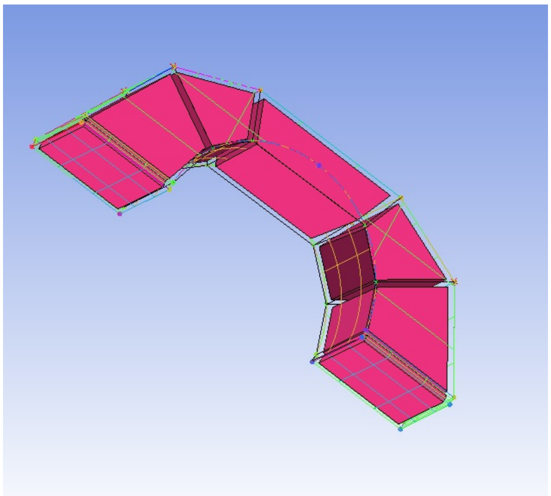

Figure 5.48: Blocking of Upper Casing

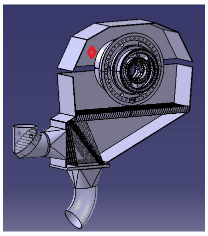

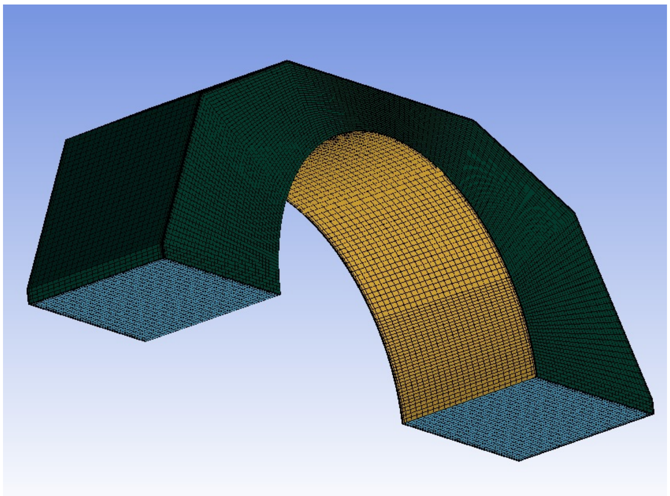

Figure 5.49: Mesh of Upper Casing

nodes	201600
quads	23302
hexas	189735

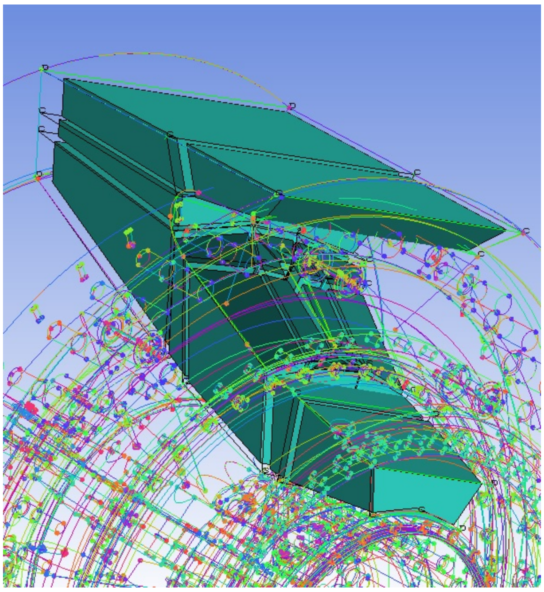

Figure 5.50: Blocking of Annulus

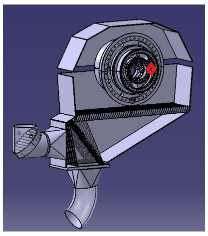

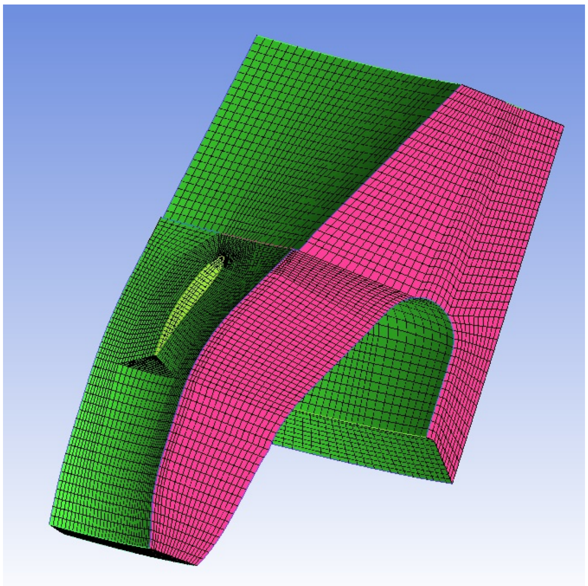

Figure 5.51: Mesh of Annulus

nodes	82936
quads	15298
hexas	75096

6 Pre-processing and Simulation

A numerical simulation demands several steps, which have to be taken. A brief overview shall be given, with a subsequent detailed description of every stage the present simulation went through.

- **Pre-processing**: This stage contains every step from the moment you receive the description of your technical problem to the start of the setup for your calculation. Generating the mesh, reading it and adapting it as needed.
- **Simulation**: Setting up all physical properties, the required boundary conditions and the solver options. After this, the solution can be calculated.
- **Post-processing**: This is the final phase of the numerical analysis, where the obtained results will be illustrated in proper figures and plots. Finally, a conclusion is drawn, which is presented.

For every step of the described procedure for a numerical analysis, there are different tools. In most cases it is more convenient to make use of different software for every step, because every tool was developed for just one purpose originally, but often programs offer the opportunity, through further work of developers, to take additional steps with the same software. The advantage of this tactic is obvious, that one saves time, if an additional program has not to be learned. Also the compatibility of different software will not be a problem, which is often not guaranteed, if work is performed in many different tools. For sure, one has to think of these matters in advance, to individually find the best compromise possible.

6.1 Pre-processing

6.1.1 Creation of Quality Output Files

The geometry and the generated mesh partitions were discussed in chapter 5. At that point the various pre-mesh partitions have to be converted in meshes to obtain output files for *ANSYS Fluent*.

It is of great importance to name the different faces correctly, without causing confusion. An example shall illustrate the potential problem.
Fluent recognizes a given name like **interface3** as interface and if the face is meant to be a wall, then confusion will arise, plus additional effort to redefine the type of face.

By treating the names, one specifies, with caution, work will be much easer afterwards.

We have to make sure, that the pre-mesh does not contain any negative cell, because it means, that something went wrong with the associations of the vertices or that a mistake in the geometry or blocking was made and that could cause problems. In addition, cells with very low quality are not good for the calculation, but in some cases compromises have to be made. There are many options integrated in *ANSYS ICEMcfd* for checking the pre-mesh quality. Here, the 3x3 determinant criterion with a plot, ranging from -1 till 1, was applied on each grid partition, guaranteeing that no negative cells and as few as possible low-quality cells are part of the pre-mesh. This metric for quality computes the deformation of the elements by first calculating the Jacobian for each hexahedron an then normalizing the determinant of the matrix. There are also some possibilities to let the program smooth out the mistakes. In some cases, such a feature can be helpful and save time, but in most cases these methods will not solve the problem, but only make things worse.

Converting the pre-mesh into an unstructured mesh is the next step to be taken. After this, a mesh check was performed to see, if all mesh properties are OK. A check of the mesh quality was made, similar to the procedure explained before. Now, all requirements are fulfilled to write an output file for the solver.

6.1.2 The Way to Implement the Grid

In this section, problems one encounters with implementing a complex grid in *ANSYS Fluent V14* will be described and one possible way to problem solution, which was chosen in the present thesis, will be pointed out.

First of all, we have to **read** in the mesh partitions individually. It is advisable to start with the most complex part of the mesh, because the chance of encountering a problem there is higher as for simple parts and once geometry, consists of many partitions, making changes and corrections becomes difficult. Now we have a basis structured grid read in and we just have to **append** part after part.

After finishing that, we have to be sure the imported mesh is scaled correctly by checking the dimensions of domain. Since *ANSYS ICEMcfd* works in *mm* by default the grid has to be scaled, because *ANSYS Fluent* applies SI units on provided geometry. It is important to scale the grid straight after implementing the mesh, before one defines interface connections, because by changing the coordinates of nodes in physical space by scaling, the defined boundary conditions would be wrong, because every physical quantity depending on length, therefore also area and volume would be incorrect. This leads to divergence right at the start of the initialisation step. If this situation occurs, the simplest and fastest way to get things under control is to work in batch mode, which means you have a certain geometry in one case and you want to transfer all applied settings of the case to another case with different geometry. *ANSYS Fluent V14* can treat settings and case separately, which leads us to the following procedure. First we make use of command **write-settings**. This writes a file with all settings applied in original case. After this, we change geometry, as required and then make use of command **read-settings**. By using this technique it is important that defined interface connections get deleted by adopting changes on geometry and all geometrical elements are obliged to have same names.

Unfortunately, the complex mesh partitions of the single blade rows, the tandem cascade and the annulus could not be implemented as one part, without causing problems to *Fluent*. The idea, which lead to a solution was to reduce the complexity of the mesh partitions by implementing the different lateral blades with their domain separately and then import just one segment of the middle blades, which then was copied in the right direction with the command **copy-move-cell-zone**, *ANSYS Fluent V14* has included. This command gives you the opportunity to create either a translational or a rotational copy of your mesh.

After doing this, the command **merge zones** will be necessary to reduce the effort of assigning the interfaces to each other. The following example of the tandem cascade shall specify the problem one encounters. Building the grid as described above, results in a domain for these tandem rows, where 52 different fluid zones arise for 52 blade rows with each of them having individual inlet facets, outlet facets, walls and interfaces. This is inconvenient and would take a lot of time to assign the right interfaces and the probability of making mistakes gets enormous. Therefore, before executing this step, reducing the number of interfaces is substantial. An additional problem with **merge zones** is, that *Fluent* has a very tight tolerance defined by default, on how much space zones, which are to be merged, are allowed to have between them. Since the present geometry is complex and many face parts and zones have to be merged, this tolerance has to be adapted to a higher value, because otherwise the program will not merge the desired zones and an error message occurs. Using the TUI-panel the command **mesh/modify-zone/matching-tolerance** can be used to adjust the default value of [0.05] to [0.3], as it was done in the present work. After this, there will be a greater possibility, that the program eventually assigns undesired zones to each other. So one has to check, if desired zones were merged.

The next step is to guarantee, that the partitions are located and split by the applied interfaces at the exact same position and are named differently in each partition file, because in the next step they will get assigned to each other. For this reason, they obligatorily must have different names. It is important to know, that *Fluent* takes data from one side of interface, which comes first in flow direction and interpolates it to the other side of interface to provide non-conformal nodes with required information for solving the equations.

Now everything we need for the command **Create/Edit** is in place. This allows us to create all interface connections of the computational grid. Here an advantage arises, if the procedure of building the mesh is the same for every complex partition, because *Fluent* automatically creates a changed name for a copied partition just by appending the number of the new zone to the original name. Therefore, a logical pattern of all named faces unfolds, with every element of same type, having the same difference to the one before it and the one after it. If this logical pattern is detected, one saves lots of time and the chance of making mistakes is reduced to a minimum. If such problems would be encountered often, for sure the convenience of a tool, which makes these assignments for you, gets obvious. Once this is done, *Fluent* tells you through a mesh check, if all existing interfaces are assigned correctly or, if there are unassigned faces. The following figure illustrates, how the interface connections were made for the numerical grid of the mixing chamber.

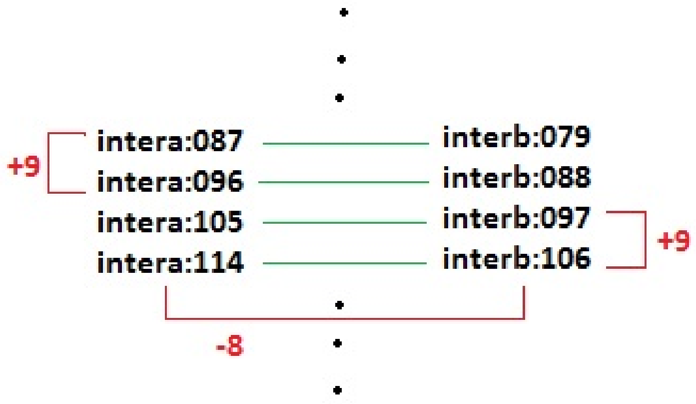

Figure 6.1: Interface Connections

6.1.3 The Numerical Grid

By the time, all interface connections are made and all boundaries are defined correctly, a final mesh check should confirm the status. On the following figures, the implemented grid properties will be presented.

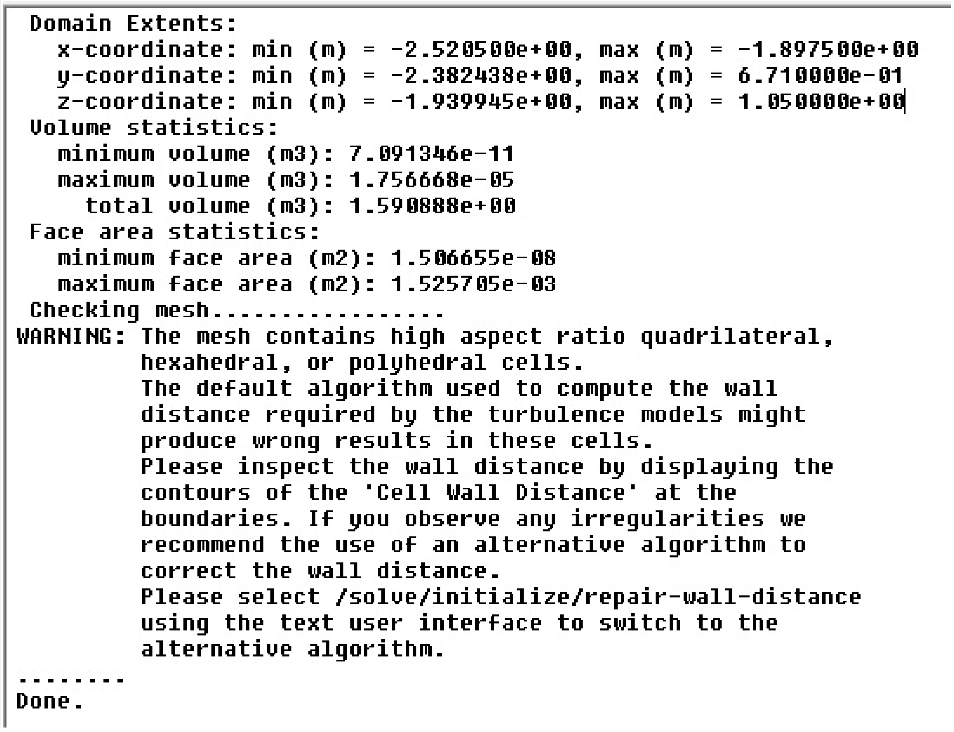

```
 Domain Extents:
   x-coordinate: min (m) = -2.520500e+00, max (m) = -1.897500e+00
   y-coordinate: min (m) = -2.382438e+00, max (m) = 6.710000e-01
   z-coordinate: min (m) = -1.939945e+00, max (m) = 1.050000e+00
 Volume statistics:
   minimum volume (m3): 7.091346e-11
   maximum volume (m3): 1.756668e-05
     total volume (m3): 1.590888e+00
 Face area statistics:
   minimum face area (m2): 1.506655e-08
   maximum face area (m2): 1.525705e-03
 Checking mesh.................
WARNING: The mesh contains high aspect ratio quadrilateral,
         hexahedral, or polyhedral cells.
         The default algorithm used to compute the wall
         distance required by the turbulence models might
         produce wrong results in these cells.
         Please inspect the wall distance by displaying the
         contours of the 'Cell Wall Distance' at the
         boundaries. If you observe any irregularities we
         recommend the use of an alternative algorithm to
         correct the wall distance.
         Please select /solve/initialize/repair-wall-distance
         using the text user interface to switch to the
         alternative algorithm.
........
Done.
```

Figure 6.2: Grid Check

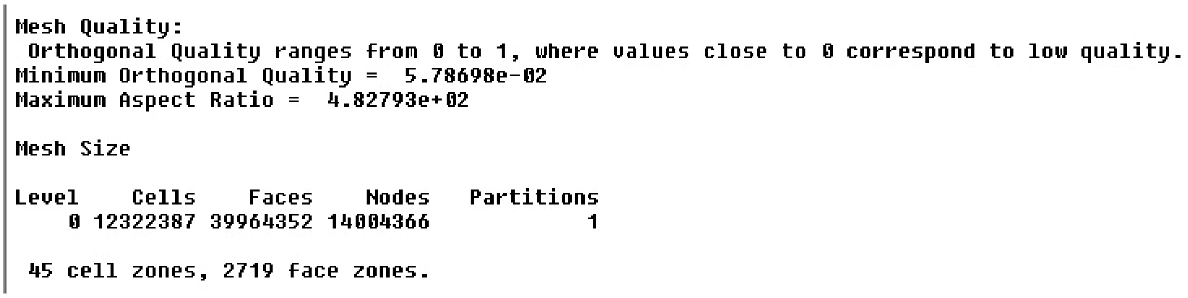

```
Mesh Quality:
 Orthogonal Quality ranges from 0 to 1, where values close to 0 correspond to low quality.
Minimum Orthogonal Quality =  5.78698e-02
Maximum Aspect Ratio =  4.82793e+02

Mesh Size

Level    Cells    Faces    Nodes   Partitions
    0 12322387 39964352 14004366            1

 45 cell zones, 2719 face zones.
```

Figure 6.3: Grid Information

6.2 Simulation

In the present section the general course of action, the case setup with physical explanations and the definition of boundary conditions will be discussed in detail. Furthermore, an applied strategy for solving compressible flow will be presented and the procedure of calculation will be described.

6.2.1 Numerical Analysis Tactic

Since a turbulence model is needed to close the system of equations, choosing the right one is essential. One encounters a variety of models for a numerical simulation. Unfortunately, there is no strict guideline, which model obtains best results for certain cases. That is why it is necessary to perform various simulations, where the obtained results are compared to measurement results in order to finally decide, which solution fits best. A brief description of the chosen models for the present work follows:

- **realizable $\mathbf{k}-\epsilon$**
  The term realizable stands for mathematical constraints on the Reynolds Stresses consistent with the physics of turbulence.
  This model has two adopted features in comparison to the standard $k-\epsilon$ model. First, a new eddy-viscosity formula, involving a variable C_μ was implemented and secondly a new model equation for dissipation ϵ based on the dynamic equation of the mean-square vorticity fluctuation is used.
  Therefore, it promises more accuracy in flows involving rotation, boundary layers under strong adverse pressure gradients, separation and recirulation.
  The eddy vicosity in $k-\epsilon$ models is computed from

  $$\mu_t = \rho C_\mu \frac{k^2}{\epsilon} \tag{6.1}$$

  In equation 6.1 the variable C_μ is no longer constant.

- **SST $\mathbf{k}-\omega$**
  The Shear-Stress Transport (SST) $k-\omega$ model was refined in comparison to the standard $k-\omega$ model. It uses the standard $k-\omega$ and the $k-\epsilon$ models, which are multiplied by a blending function and added together. The design of this blending function is 1 in the near-wall region, activating $k-\omega$ and 0 away from the surface, activating $k-\epsilon$. Another modification is, that this model incorporates a damped cross-diffusion derivative term in the equation of ω. The definition of turbulent viscosity is also modified to account for the transport of the turbulent shear stresses. Finally, the model constants are different.
  These features promise more reliable and accurate results, than the standard $k-\omega$ model for flows involving adverse pressure gradient flows, air foils and transonic shock waves.

The turbulent viscosity is computed as

$$\mu_t = \frac{\rho k}{\omega} \frac{1}{max\left[\frac{1}{\alpha^*}, \frac{SF_2}{a_1 \omega}\right]} \tag{6.2}$$

In equation 6.2 S is the strain rate magnitude, F_2 is a blending function and α^* is a coefficient, which damps the turbulent viscosity, causing low-Reynolds number correction.

- **Reynolds Stress Model (RSM)**
  The RSM promises good results for cases with a high degree of swirling and rotating flow passages, which in the present case of the mixing chamber could be beneficial. The 7-equation approach is often more accurate, but the additional computational cost is a disadvantage.
  The eddy viscosity is computed equally as in $k - \epsilon$ models with the variable $C_\mu = 0.09$.

For further information on turbulence models see [11].

6.2.2 Case Setup

In the present thesis the numerical calculations were performed with the software package ANSYS Fluent V14, which contains the broad physical modeling capabilities needed to model flow, turbulence, heat transfer, and reactions for industrial applications.

Here, it is again strongly recommended, as it was before with *ICEMcfd* to follow the hierarchy the program proposes, because actions are very consuming in computational cost. This methodology will save time and prevent trouble. The next figure gives an overview of the user interface the program *ANSYS Fluent V14* offers.

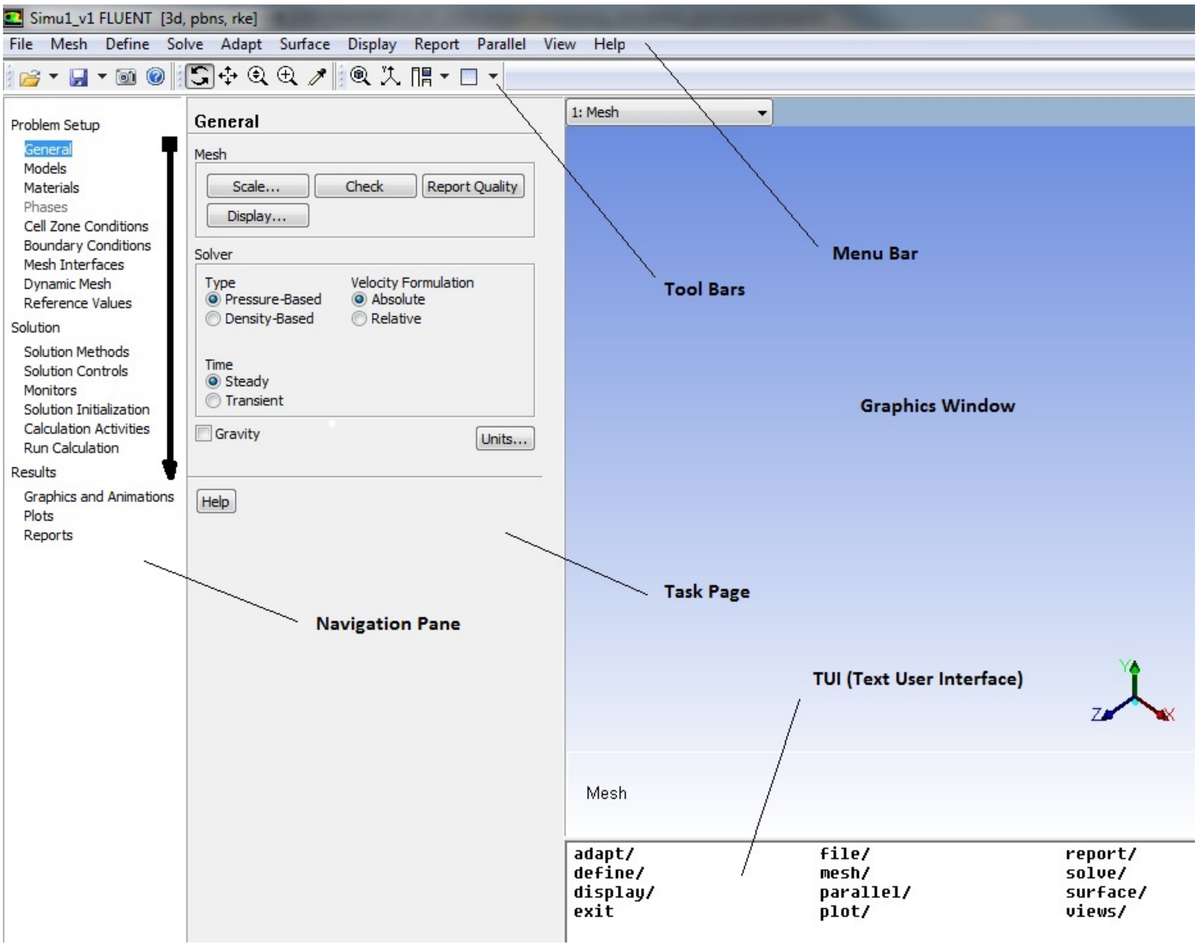

Type
● Pressure-Based
○ Density-Based

Velocity Formulation
● Absolute
○ Relative

Time
● Steady
○ Transient

☐ Gravity

```
adapt/          file/           report/
define/         mesh/           solve/
display/        parallel/       surface/
exit            plot/           views/
```

Figure 6.4: Fluent V14, User interface

The presentation of the settings will follow the order of navigation panel for retaining clarity.

Starting with the problem setup, the first thing to do is to choose the basic solver settings, as it is shown in figure 6.4.

In the models category the set of equations for solving the problem have to be chosen. Here, the energy equation was activated and a variation of viscous models was performed. Firstly, the realizable $k-\epsilon$ model with enhanced wall treatment and activated viscous heating was applied. This means that the convective heat transport in the "modeled" energy equation is represented by the deviatoric stress tensor $(\tau_{ij})_{eff}$ see [11]. Secondly, the SST $k\omega$ model was chosen and finally a calculation with the Reynolds Stress Model was made.

Air was defined as material for all domains, with density being calculated by ideal gas law, which can be written as:

$$\rho = \frac{p_{op}+p}{\frac{R}{M_w}T} \tag{6.3}$$

The specific heat c_P and the thermal conductivity λ were derived from an average value of the two inlet conditions given and were set as constant.

The viscosity was calculated by Sutherland's law with the three coefficient method, which is:

$$\mu = \mu_0 + \left(\frac{T}{T_0}\right)^{3/2} \frac{T_0+S}{T+S} \tag{6.4}$$

The molecular weight was set as constant.

Next category is boundary conditions, were the boundaries of the problem setup get specified. In the present case two mass-flow inlets were defined and the temperatures were set. The outlet was defined as pressure outlet with the given static (gauge) pressure. For all boundaries the turbulence specification method, which was chosen, is the intensity and hydraulic diameter.

The implemented mesh interfaces, are described in section 6.1.2.

This brings us to the solution tab. Under "Solution Methods" the "Pressure-Velocity Coupling Scheme" was chosen as "Coupled". The Spatial Discretization for Gradient was set as "Least Squares Cell Based", for pressure as "Standard" and the rest of the options were set as "Second Order Upwind", because this discretisation scheme is more accurate than the "First Order Upwind". The reason for this is, that reference values of two neighbouring cells before are considered.

Under "Solution Controls", the Courant number can be set, which is defined as

$$CFL = \frac{u \cdot \Delta t}{\Delta x} \tag{6.5}$$

It indicates how many cells an observed quantity maximal moves on per timestep. Reducing it to 20 and treating the "Under Relaxation Factors" as described in section 6.2.3, were important to achieve a stable calculation.

Two additional monitors were defined, apart from the default monitor for residuals. The first showed the mass-flow weighted average at outlet and the second plotted the curve of area-weighted average total pressure at the two inlets. These monitors provide information needed to check during the calculation if boundary conditions which are not known but get calculated, approach desired values.

The "Solution Initialisation" was performed, as described in the next section.

Now, calculation process can be started.

6.2.3 Solution Strategy for Compressible Flows

There are difficulties associated with solving compressible flows. This results from the high degree of coupling between the flow velocity, density, pressure and energy. Special solution techniques may be required in order to obtain a stable calculation and a converged result. In addition, shocks (discontinuities) may occur in the flow, producing a further stability problem. The solution strategy, which was beneficial in the present simulation of the mixing chamber is the following:

- (Pressure-based solver only) Initialize the flow to be near stagnation (velocity small, but not zero, pressure to inlet total pressure, temperature to inlet total temperature). Turn off the energy equation and calculate the density with a constant value appropriate to conditions of the gas. In other words, use an incompressible calculation mode for the first 50 iterations. Leave the energy under-relaxation at 1. Set pressure under-relaxation to 0.4 and the momentum under-relaxation to 0.3. After solution stabilizes and the energy equation has been turned on switch to ideal gas law for density calculation and increase the pressure under-relaxation to 0.7[12].

7 Results

7.1 Simulation Results for the First Operating Point

The boundary conditions for the first part-load OP were presented in chapter 3, Table 3.1.

First thing to do after a simulation run is to control, if convergence is reached. Besides the indicators as residuals, mass flow rate at outlet, area weighted total pressure at inlets and area weighted total temperature at outlet, which were monitored during calculation and achieved all desired values, another criterion is necessary to make a reliable statement, if calculation reached convergence. The wall shear stress is a good indicator, because as long as the distribution over the wall of a blade still changes, the flow over the blade profile has not reached the steady state.

In *Fluent* an **iso-surface** was created right through a blade of the annulus, which was clipped properly with the **iso-clip** command, to obtain only the area around the blade. The quantities of wall shear stress around the blade contour could then be plotted. Calculation was continued for another 100 iterations and afterwards the wall shear stresses were compared to the previous solution. The two plots were approximately equal, therefore reached convergence is proven. Figure 7.1 shows the result.

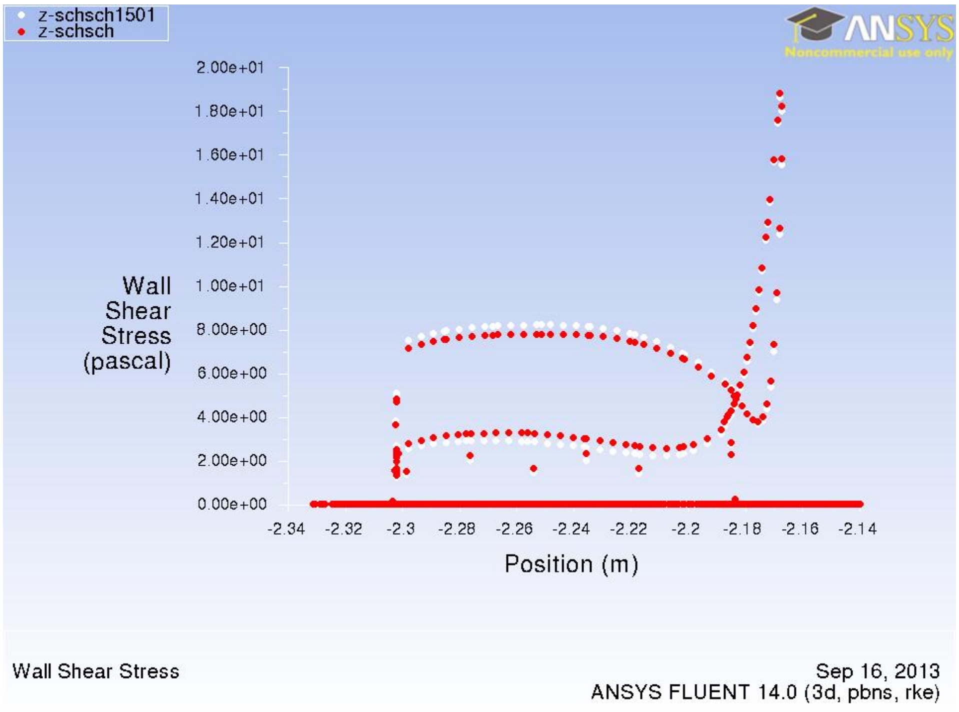

Figure 7.1: Wall shear stress around blade for OP1, realizable $k - \epsilon$

In Figure 7.1 the red distribution for the realizable $k - \epsilon$ model was obtained after 1401 iterations and the white one was received at the end of simulation step 1501.

In Figure 7.2 the same is done for the SST $k-\omega$ case. The red distribution shows the wall shear stress at iteration 1703 and the white shows the result after 100 additional iterations. From the difference of the distributions of the wall shear stress especially around position $-2,28m$ entirely reached convergence can be questioned. For some regions, where flow separation occurs calculation was not able to find a steady solution, although the SST $k-\omega$ simulation run was performed for clearly more iterations than the realizable $k-\epsilon$ simulation. Figure 7.2 presents the result.

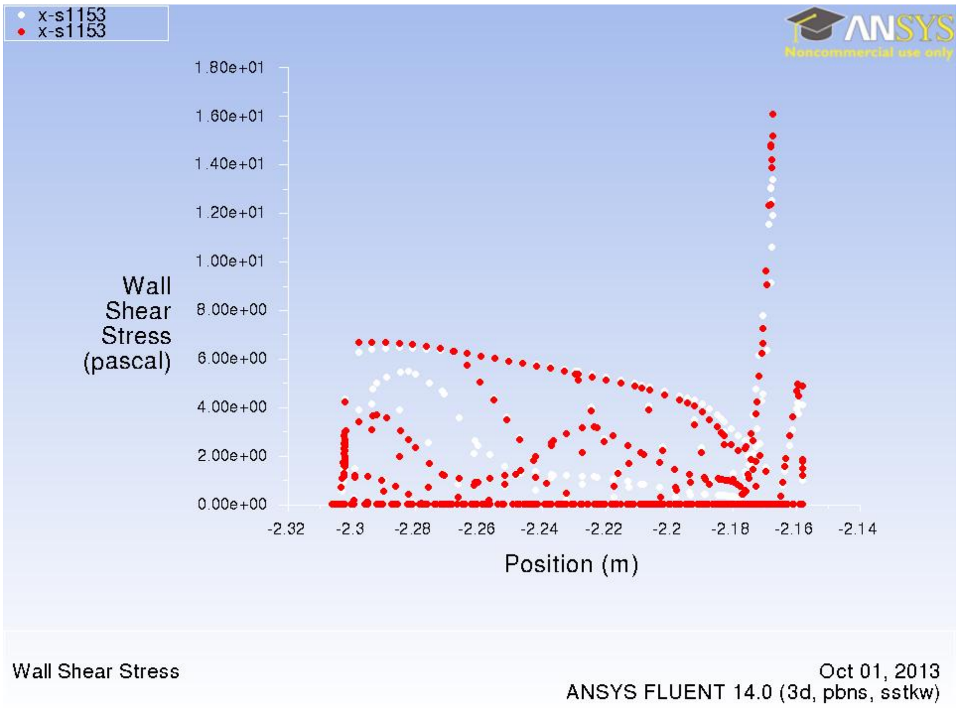

Figure 7.2: Wall shear stress around blade for OP1, SST $k-\omega$

In Figure 7.3 the temperature distribution of realizable $k-\epsilon$ simulation for OP1 is shown. This distribution can be compared to Figure 7.4, which shows the result for SST $k-\omega$ simulation and Figure 7.5 of the RSM simulation run. Figure 7.6 presents the measurement data of the total temperature distribution for OP1.

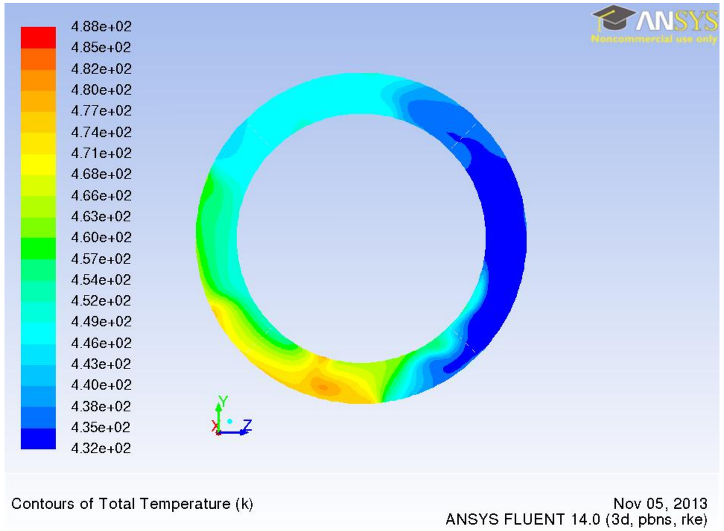

Figure 7.3: Total temperature at outlet plane A for OP1, realizable $k-\epsilon$

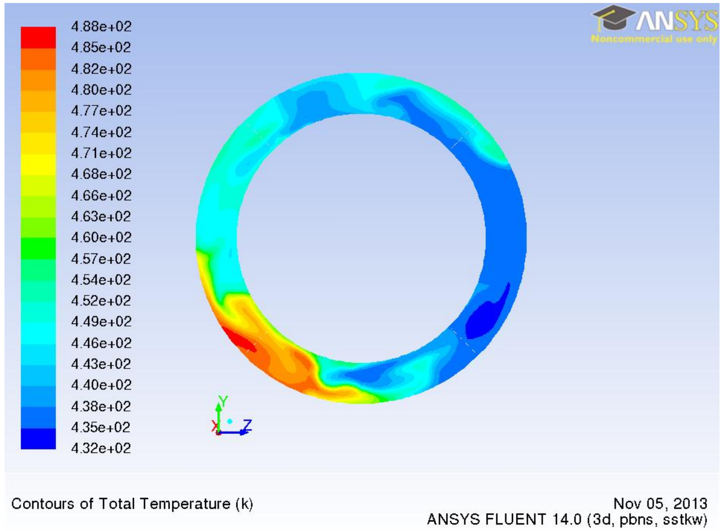

Figure 7.4: Total temperature at outlet plane A for OP1, SST $k-\omega$

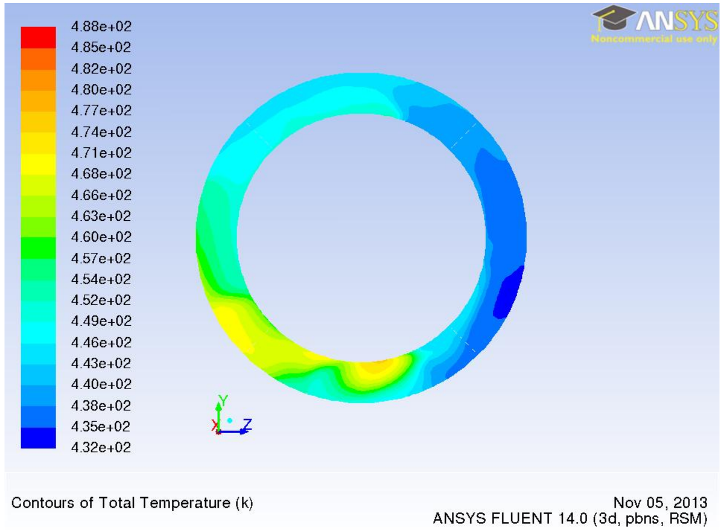

Figure 7.5: Total temperature at outlet plane A for OP1, RSM

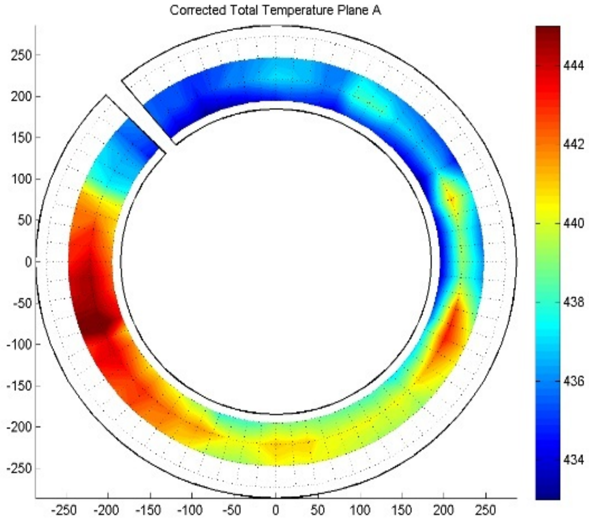

Figure 7.6: Total temperature at outlet plane A for OP1, measurements

The measurement data of temperature distribution shown in Figure 7.6 contains a hotspot in the south-west region. This hot spot has a maximum temperature of $445K$ and is detected by all performed simulation runs. In general, the calculated maximum temperatures of the simulations are of higher level than the measurement data. Possible reasons for this will be explained in section 7.5. According to measurements the south region of the outlet plane is clearly hotter than the northern segment. This was also confirmed from the realizable $k-\epsilon$ and the RSM simulation. Results obtained from SST $k-\omega$ simulation show that the hot region does not reach the south-east area. In measurements the coldest part of the outlet temperature distribution is located in the northern region of the outlet plane. All performed simulation runs obtain results for the coldest region in the east region reaching to the north. The difference between the SST $k-\omega$ simulation to the others is remarkable. The realizable $k-\epsilon$ and the RSM simulations on the other hand perform similarly and obtain results that fit better to measurements.

The differences between the applied turbulence models shall also be presented in the next Figure 7.7, which shows the total temperature at mid section of the outlet plane over the circumferential position. The starting point of received values and the position of the three axes are indicated in the diagram.

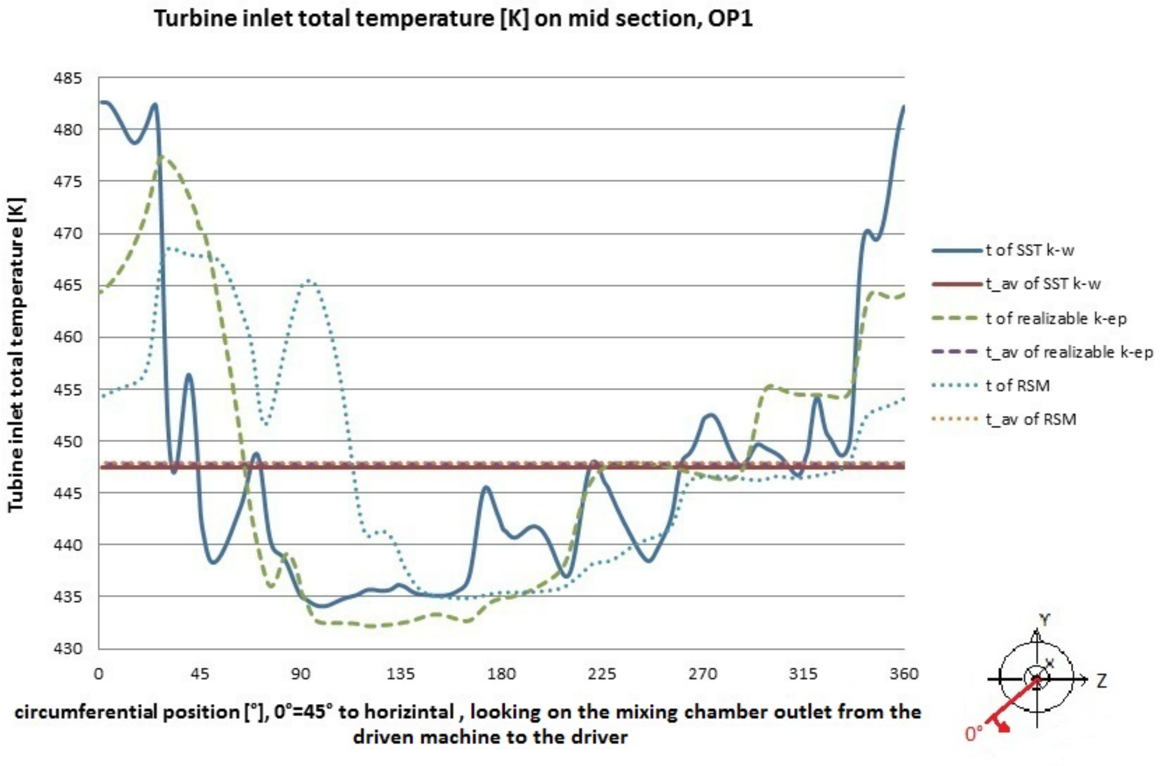

Figure 7.7: Turbine inlet total temperature for OP1

In Figure 7.7 we see how fluctuating the temperatures obtained from SST $k-\omega$ model are in comparison to the others. The realizable $k-\epsilon$ model produces a very smooth temperature distribution. The SST $k-\omega$ model has a maximum and minimum, which is of higher level than the other models. All applied turbulence models achieve the same average temperature. The tendency of the realizable $k-\epsilon$ and the SST $k-\omega$ curve is matching.
The explanation for this intensive fluctuation shown in the total temperature curve obtained from SST $k-\omega$ result is, that this turbulence model produces enormous eddies in the outlet plane. Following Figures 7.8 and 7.9 will visualize the eddies and where they are located by showing the streamlines upstream the outlet plane A. This plane shown was created $5,45cm$ upstream the outlet plane A, because there the phenomenon becomes apparent clearly. The difference between realizable $k-\epsilon$ and SST $k-\omega$ turbulence model is remarkable.

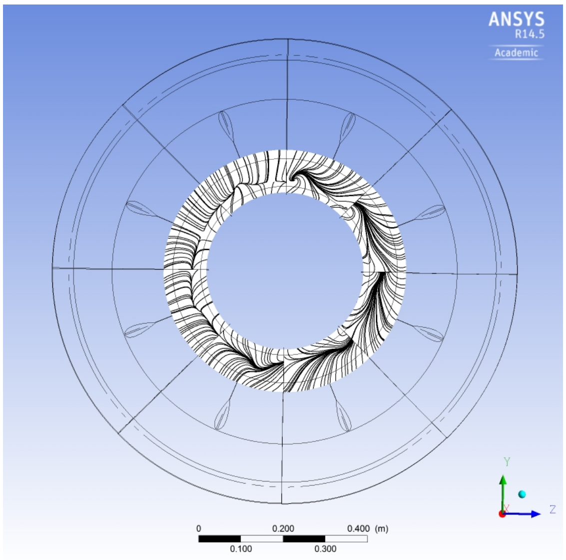

Figure 7.8: Streamlines upstream the outlet plane A for OP1, realizable $k-\epsilon$

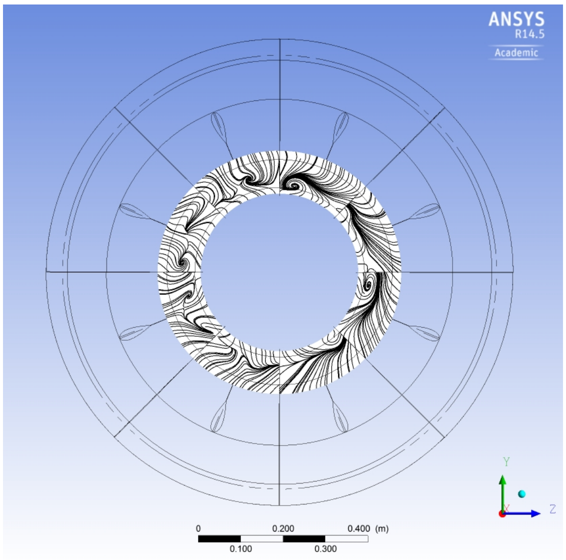

Figure 7.9: Streamlines upstream the outlet plane A for OP1, SST $k-\omega$

Checking the calculated mass-weighted average total temperature at the boundaries of the domain is important to see, if the energy is conserved. The received inlet boundary conditions for OP1 are

$\dot{m}_{SC} = 8,285\frac{kg}{s}$, $t_{tot,SC} = 394K$ and $\dot{m}_{GHH} = 7,963\frac{kg}{s}$, $t_{tot,GHH} = 504,7K$.

With these values the mass-weighted average total temperature of the inlets can be calculated as:

$$T_{tot} = \frac{T_{tot,SC} \cdot \dot{m}_{SC}}{\dot{m}_{SC} + \dot{m}_{GHH}} + \frac{T_{tot,GHH} \cdot \dot{m}_{GHH}}{\dot{m}_{SC} + \dot{m}_{GHH}} = 448,253K$$

The mass-weighted average temperature at the outlet plane obtained from the realizable $k-\epsilon$ simulation run is $T_{tot,A} = 448,262K$ and for the SST $k-\omega$ it is $T_{tot,A} = 448,258K$.

The following Figures 7.10, 7.11, 7.12 and 7.13 present the results for the total pressure distribution at outlet plane A for OP1. The measurement data of Figure 7.13 shows an almost homogeneous distribution of total pressure, which was confirmed by simulations. Again the results obtained from realizable $k-\epsilon$ model are almost equal to the RSM. The SST $k-\omega$ model generates results, which show a slightly higher level of total pressure. Compared to measurements all three simulation runs generate matching results, because differences are small.

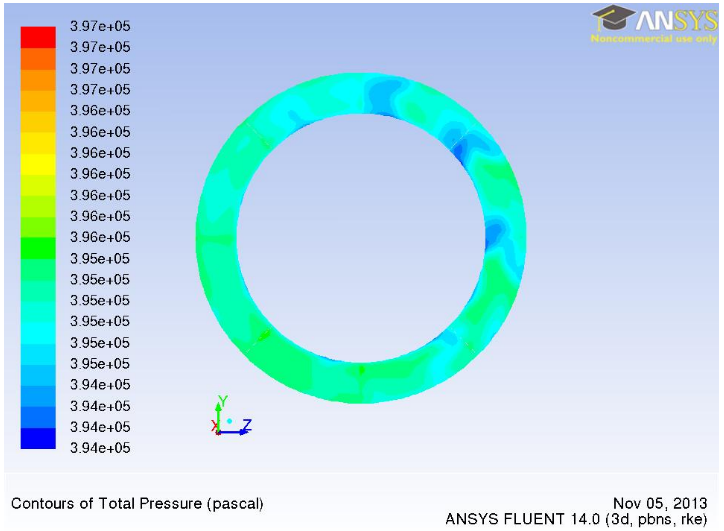

Figure 7.10: Total pressure at outlet plane A for OP1, realizable $k-\epsilon$

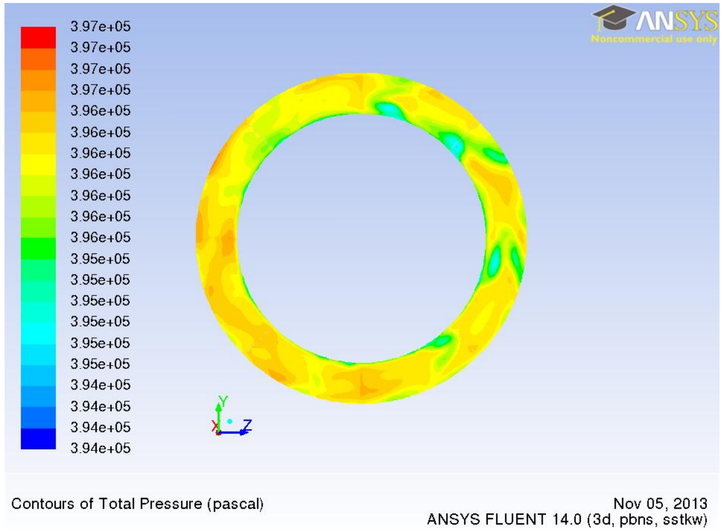

Figure 7.11: Total pressure at outlet plane A for OP1, SST $k-\omega$

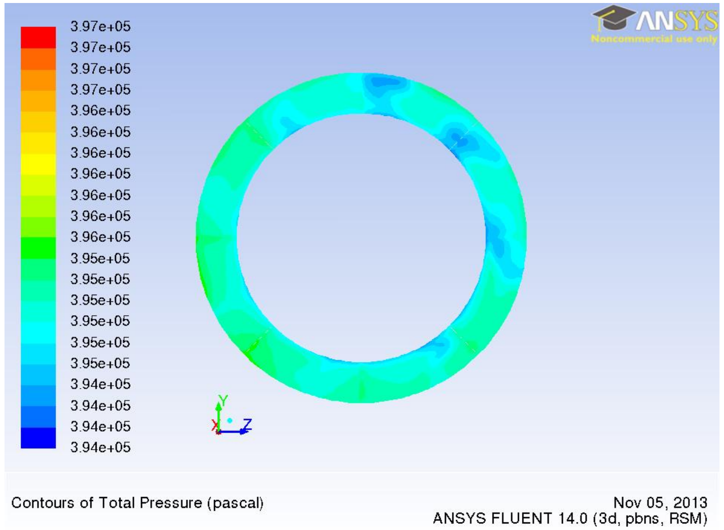

Figure 7.12: Total pressure at outlet plane A for OP1, RSM

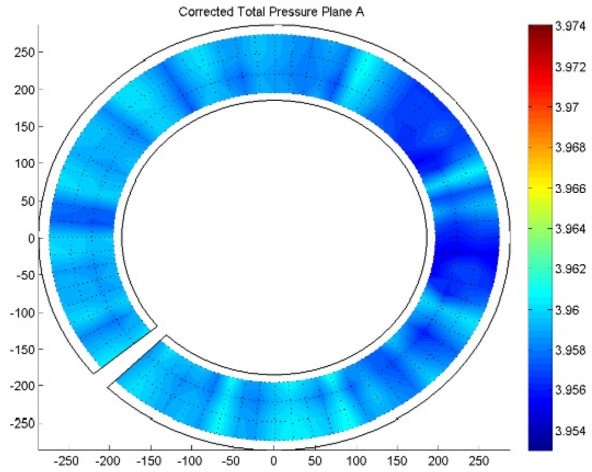

Figure 7.13: Total pressure at outlet plane A for OP1, measurements

The pressure loss calculation is an important indication, which of the different turbulence models gives the more accurate results. From measurements we know, that the inlet values are

$\dot{m}_{SC} = 8,285\frac{kg}{s}$, $p_{tot,SC} = 3,957bar$ and $\dot{m}_{GHH} = 7,963\frac{kg}{s}$, $p_{tot,GHH} = 3,979bar$.

For the outlet value we have $p_{tot,A} = 3,922bar$.

Therefore the mass-weighted average total pressure loss Δp_{tot} can be calculated as:

$$\Delta p_{tot} = \left(\frac{\dot{m}_{SC}}{\dot{m}_{SC} + \dot{m}_{GHH}} p_{tot,SC} + \frac{\dot{m}_{GHH}}{\dot{m}_{SC} + \dot{m}_{GHH}} p_{tot,GHH} \right) - p_{tot,A} = 45,8mbar$$

The realizable $k - \epsilon$ simulation produced $\Delta p_{tot} = 12,4634mbar$ and the SST $k - \omega$ $\Delta p_{tot} = 14,9532mbar$. Comparing these values, one would say, that the simulations obtain results of similar quality. There is not a clear tendency, that one of the applied turbulence models performs more accurately.

The next Figures 7.14, 7.15 and 7.16 show the turbulent kinetic energy distribution in outlet plane A of the annulus. The obtained results visualize that the realizable $k - \epsilon$ finds turbulent kinetic energies of a higher degree than the SST $k - \omega$ turbulence model and the RSM. The north-east region of the outlet plane contains three spots, where maximum values around $65,4\frac{m^2}{s^2}$ are reached. In SST $k - \omega$ simulation results these spots are not as widely spread as in the others, but are still detected with maximum turbulent kinetic energies of $45\frac{m^2}{s^2}$. The RSM agrees with SST $k - \omega$ simulation in maximum value, but the contour of its turbulent kinetic energy distribution is similar to the result of the realizable $k - \epsilon$ model.

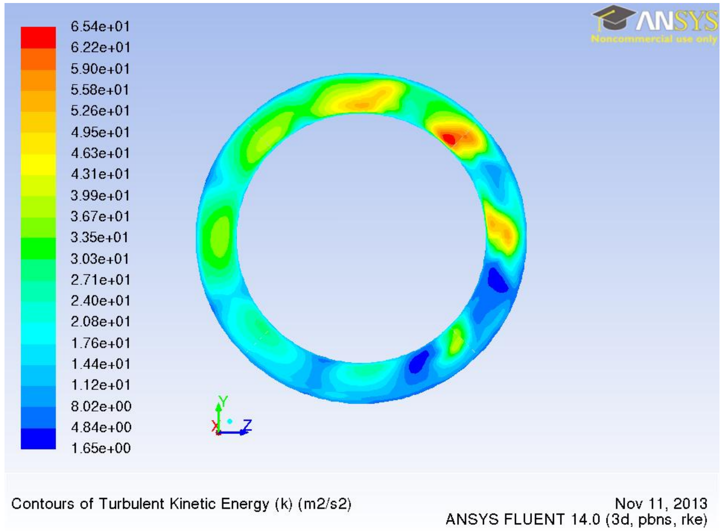

Figure 7.14: Turbulent kinetic energy at outlet plane A for OP1, realizable $k-\epsilon$

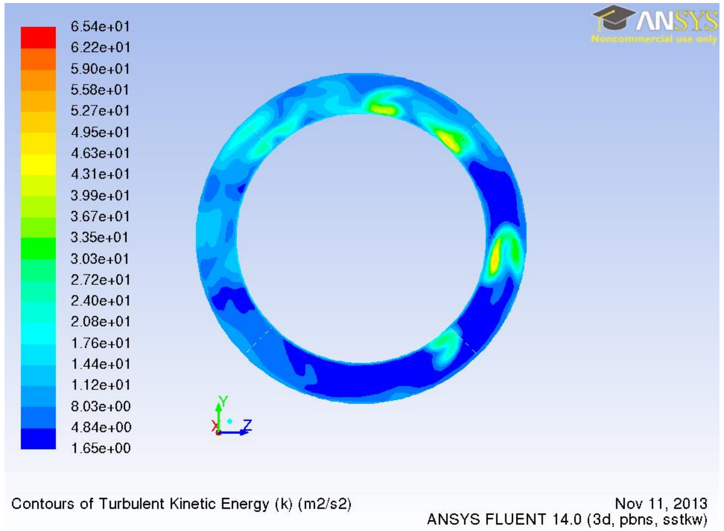

Figure 7.15: Turbulent kinetic energy at outlet plane A for OP1, SST $k-\omega$

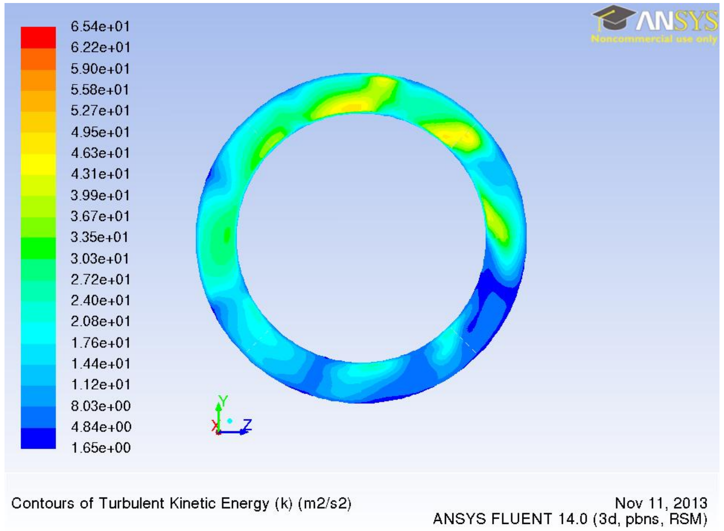

Figure 7.16: Turbulent kinetic energy at outlet plane A for OP1, RSM

An explanation of these locally occurring high turbulent kinetic energies shall be given with the following figures.
In Figure 7.17, 7.18 and 7.19 the axial velocity distribution of the outlet plane A is shown for the different simulation cases. It is noticeable that the obtained results of all performed simulations show regions of backflow with negative axial velocities in the east of the outlet plane. These are the explanation for the high values of turbulent kinetic energy. In the west region these distributions reach the maximum value. The SST $k-\omega$ model has a clearly lower minimum and a higher maximum than the realizable $k-\epsilon$ and the RSM model.

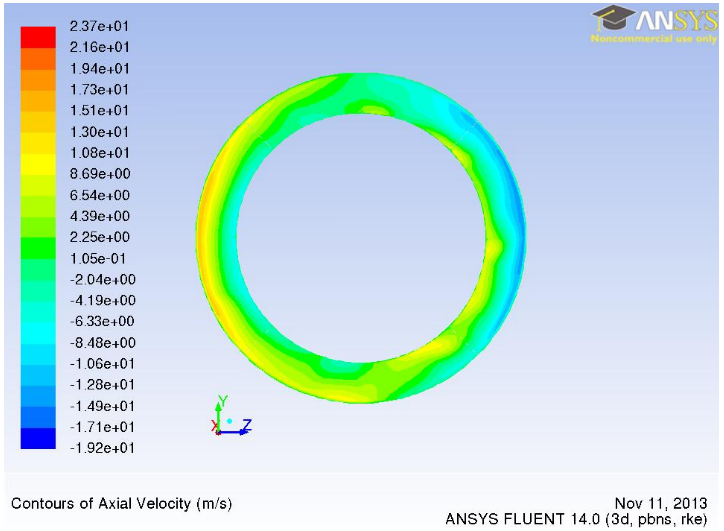

Figure 7.17: Axial velocity at outlet plane A for OP1, realizable $k - \epsilon$

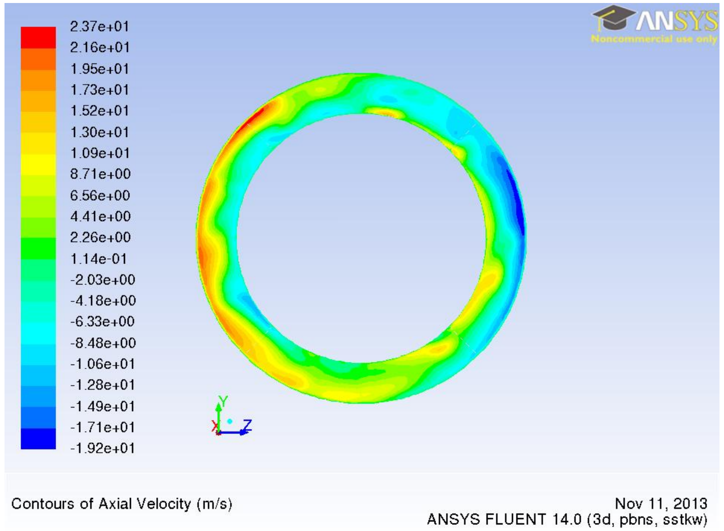

Figure 7.18: Axial velocity at outlet plane A for OP1, SST $k - \omega$

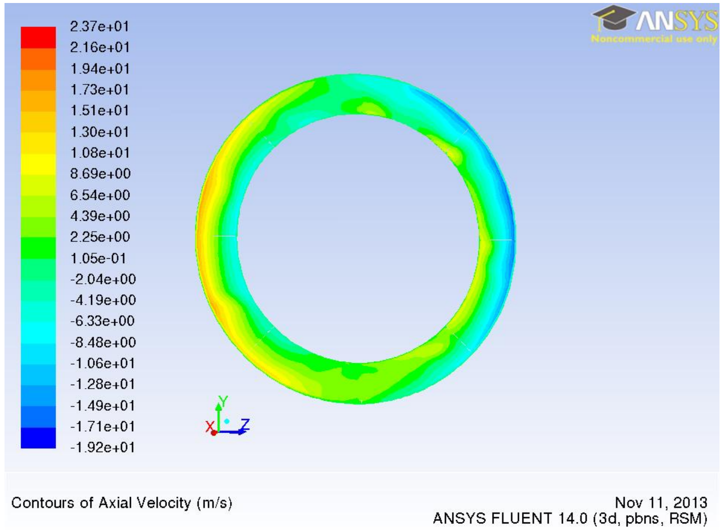

Figure 7.19: Axial velocity at outlet plane A for OP1, RSM

The RSM was initialized with a fully converged solution of the realizable $k-\epsilon$ model and calculation progress was achieved for about 100 iterations with "under relaxation factors" being very low, allowing the calculation to find a way of stabilizing. At that point the residuals and the other monitored quantities reached an acceptable level. When the simulation was continued, the calculation diverged. One plausible explanation for this is the mesh quality. Obviously the high skewness and the low orthogonal quality of some cells, which was inevitable due to the complexity of the geometry might be the reasons, why the calculation diverged. The sensitivity to cells, which are not orthogonal to flow direction is remarkable in RSM calculations.
The results showed, that the RSM is not performing more accurately in the case of the mixing chamber than the 2-equation models and the stability of calculation is problematic. Therefore it was not applied in the simulations for the next operating points.

7.2 Simulation Results for the Second Operating Point

Simulations were initialized with the obtained solutions of the first part-load OP. The applied boundary conditions are given in chapter 3, Table 3.2. Here again the same methodology as in OP1 will be used to prove convergence, followed by the distributions of total temperature, total pressure and turbulent intensity for the outlet plane A of the annulus.

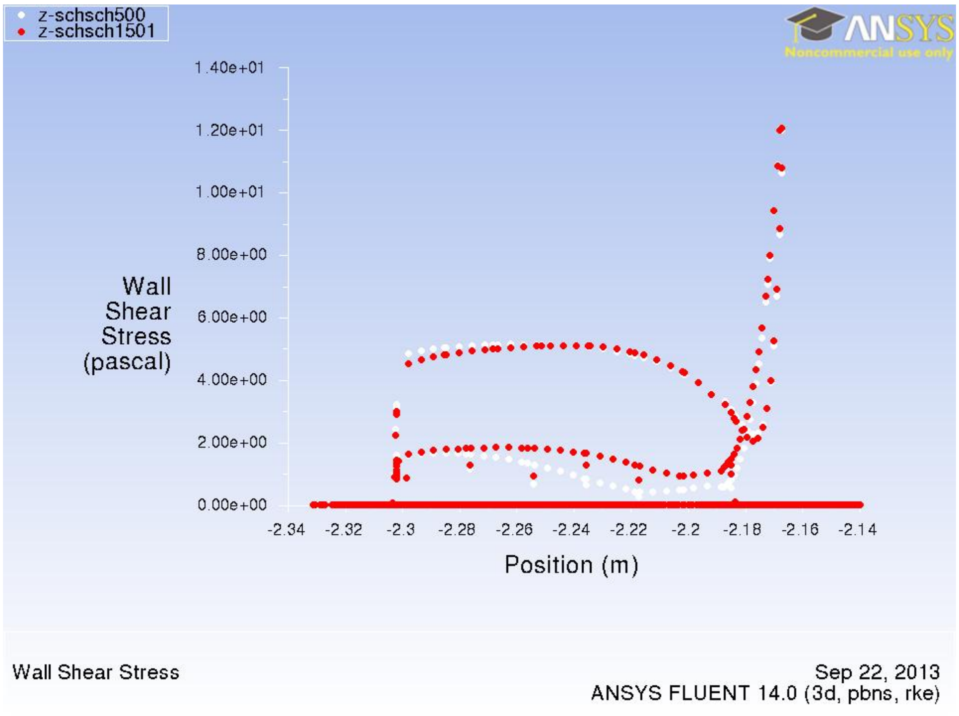

Figure 7.20: Wall shear stress around blade, realizable $k - \epsilon$

In Figure 7.20 the red distribution was achieved at iteration 400 and the white one shows the result after 100 additional iterations. The distributions in the lower region of wall shear stress at about $-2.22m$ are slightly different, because regions of flow separation prevented a steady solution.

In Figure 7.21 the wall shear stress distributions for the SST $k-\omega$ simulation follow the same tendency mentioned in OP1. Despite more performed iterations the simulation was not able to obtain equal distributions. Again the reason for this are regions of flow separation preventing a steady and completely converged solution. The red curve was obtained after 700 iterations and the white one after iteration 800.

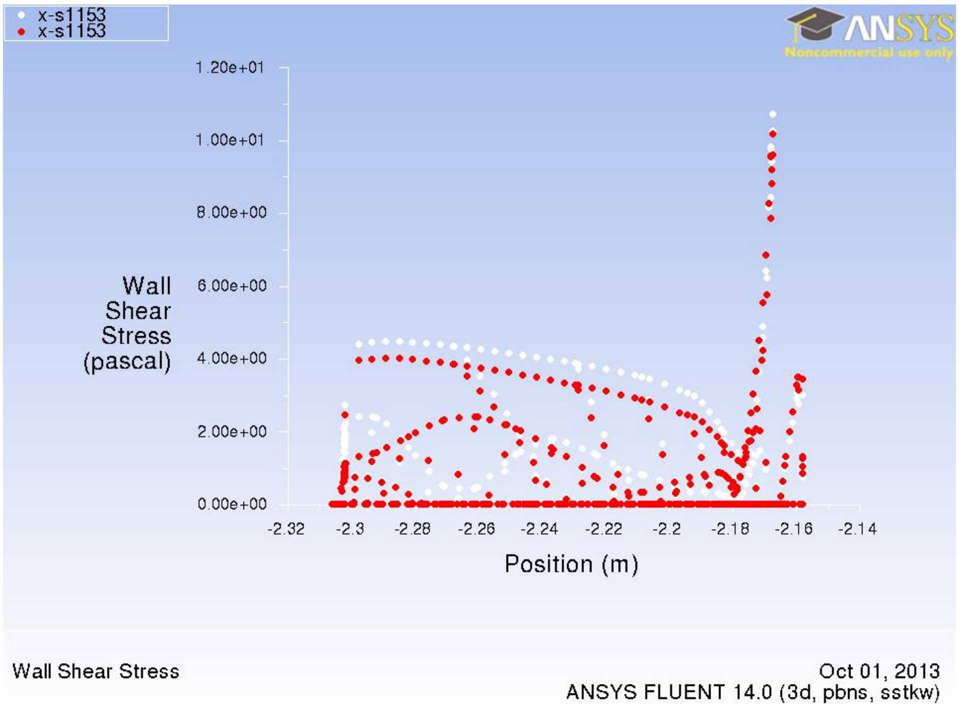

Figure 7.21: Wall shear stress around blade, SST $k-\omega$

In Figures 7.22, 7.23 and 7.24 the total temperature distribution at the outlet plane of the annulus are illustrated for OP2.

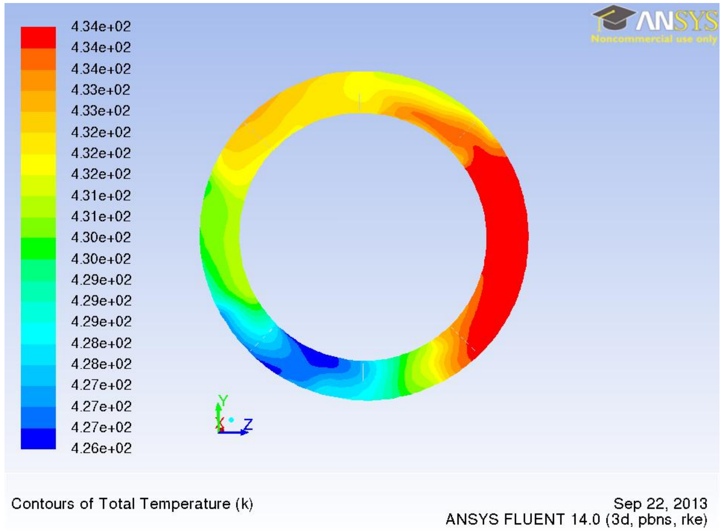

Figure 7.22: Total temperature at outlet plane A for OP2, realizable $k-\epsilon$

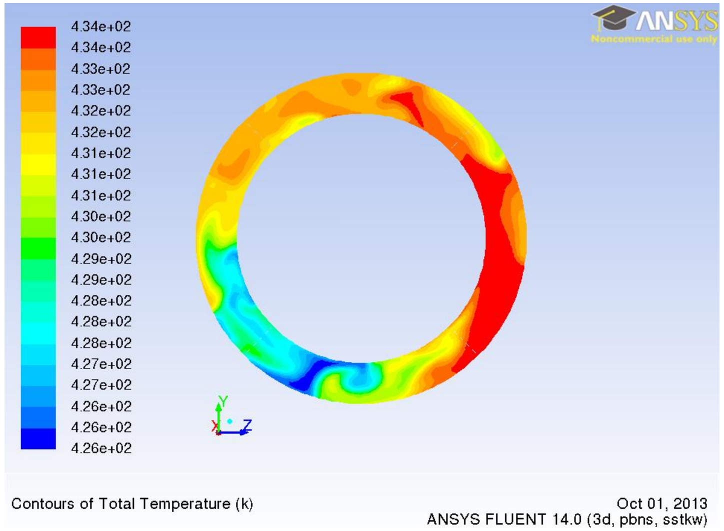

Figure 7.23: Total temperature at outlet plane A for OP2, SST $k-\omega$

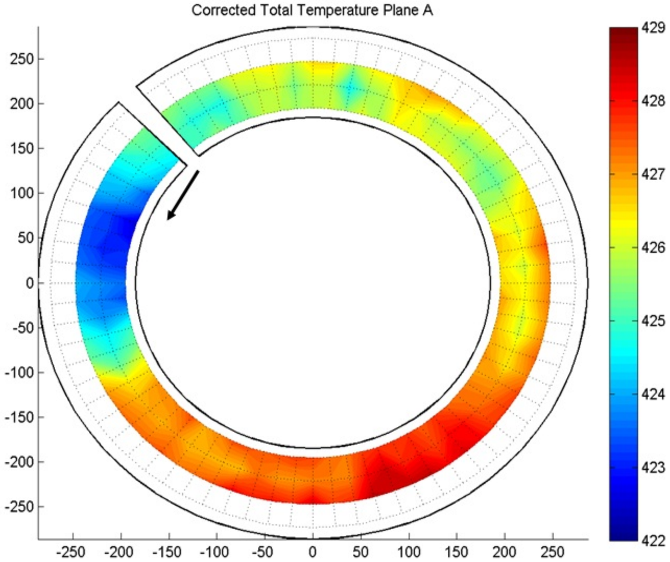

Figure 7.24: Total temperature at outlet plane A for OP2, measurements

In Figure 7.24 the measured total temperature distribution is shown for part-load OP2. The hotspot is detected in the south-east region of the outlet plane. At this OP the hotter air is provided by the compressor station located in the basement of the Institute for Thermal Turbomachinery and Machine Dynamics. It enters the mixing chamber at Inlet SC and not at Inlet GHH as it was in OP1. Therefore it is a logical consequence, that regions of colder pressurized air from OP1 are the hotter spots in OP2. The total temperature distributions obtained from different simulation runs are shown in Figures 7.22 and 7.23. The gradient of total temperature is reproduced correctly especially by the realizable $k-\epsilon$ simulation. Simulation results would fit perfectly, if the distribution would be turned for 90 degrees in clockwise direction. Still the hotspot of the measurement data, which is located in the south-east region is confirmed by simulations. The cold air of measurements is located in the western region and the simulations generate results where this cold air is located in the south-west region. The differences between the two turbulence models are remarkable. Compared to measurement data the obtained results of the realizable $k-\epsilon$ model fit better.

Figure 7.25 shows the obtained total temperature distribution on the mid section of the outlet plane, comparing the results obtained from the two simulation runs. The position of the starting point for obtaining the plotted values is presented in the lower right corner of Figure 7.25 with indication of the coordinate axes. In Figure 7.25 we see that the realizable $k-\epsilon$ and SST $k-\omega$ model produce a similar total temperature

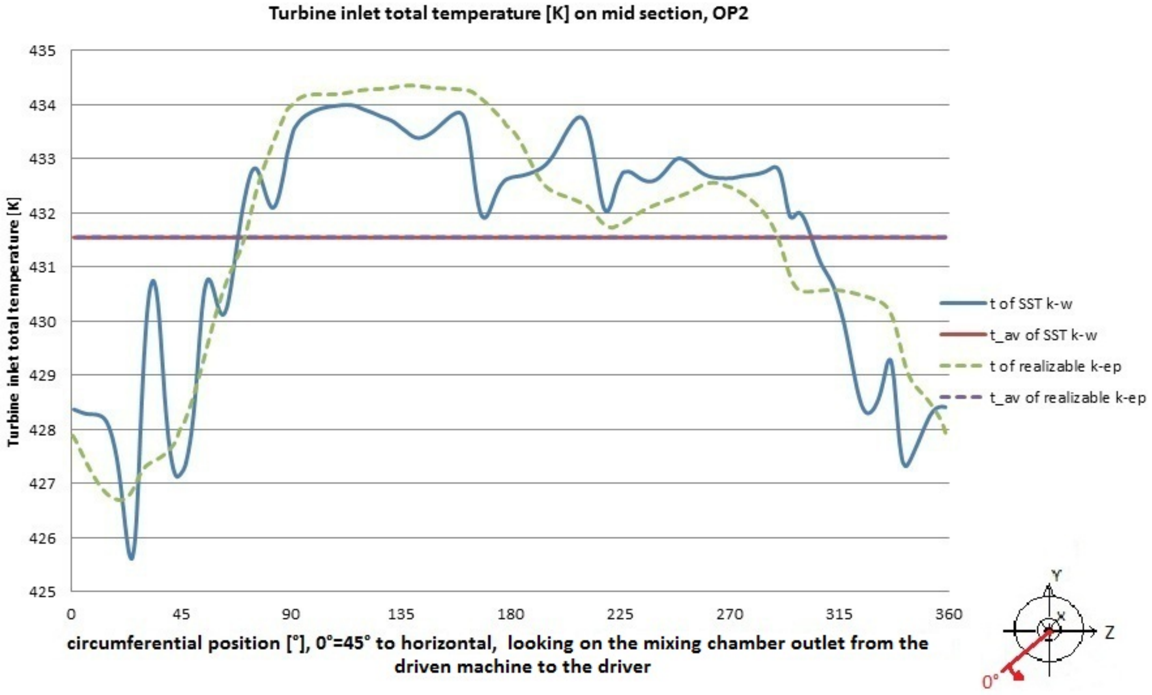

Figure 7.25: Turbine inlet total temperature for OP2

distribution in the mid section of the outlet plane. The position of local and global minima and maxima is the same. Again, as it was in OP1, the SST $k-\omega$ model generates fluctuating total temperature values on the mid section. The realizable $k-\epsilon$ model on the contrary generates a smooth curve. The average total temperature obtained from the two simulation runs is exactly the same.

In the following Figures 7.26, 7.27 and 7.28 the total pressure distributions for OP2 are shown. The total pressure distributions are almost homogeneous. The tendency of received results for OP1 are confirmed, because here again the level of total pressure obtained from SST $k-\omega$ simulation is slightly higher than in the case of realizable $k-\epsilon$. The achieved values of realizable $k-\epsilon$ simulation are more suiting to measurement data. The eastern region of measurements, shown in Figure 7.28, contains areas of slightly lower total pressure. These were also confirmed by simulations.

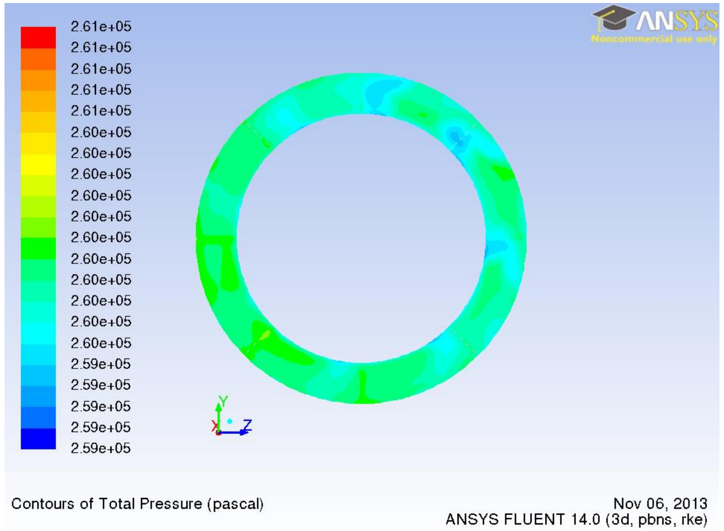

Figure 7.26: Total Pressure at outlet 2OP, realizable $k - \epsilon$

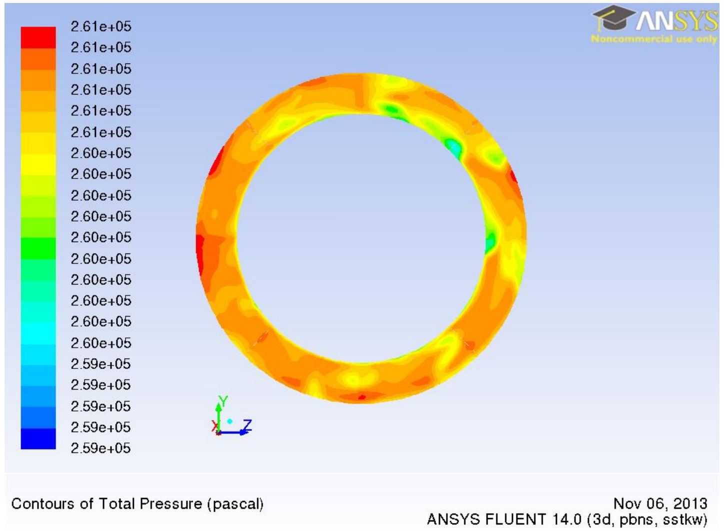

Figure 7.27: Total Pressure at outlet 2OP, SST $k - \omega$

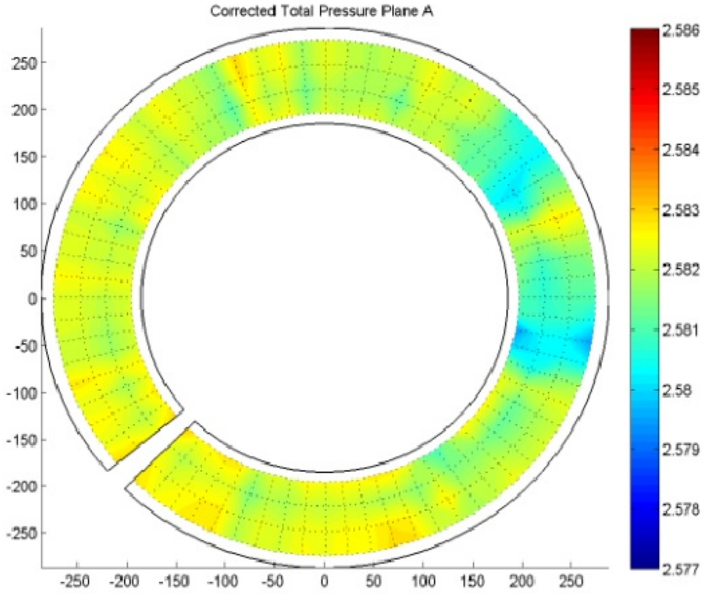

Figure 7.28: Total Pressure at outlet 2OP, measurements

Figures 7.29 and 7.30 show the distribution of turbulent kinetic energy for the two applied turbulence models. The locations of spots with higher turbulent kinetic energy is confirmed by both turbulence models. The differences are that the realizable $k-\epsilon$ model produces slightly lower values and the turbulent kinetic energy occurring in the north-west region is not reproduced by the SST $k-\omega$ simulation.

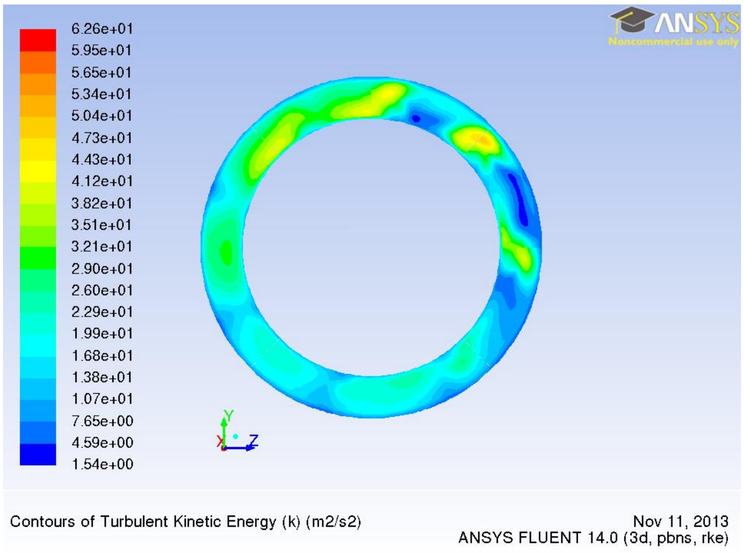

Figure 7.29: Turbulent kinetic energy at outlet plane A 2OP, realizable $k-\epsilon$

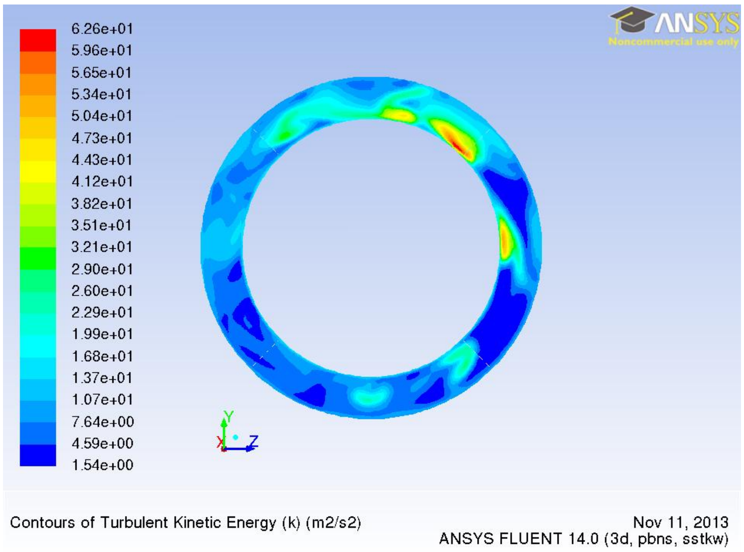

Figure 7.30: Turbulent kinetic energy at outlet plane A 2OP, SST $k-\omega$

Figure 7.31 and 7.32 show the axial velocity distribution on the outlet plane, which can be seen as an explanation for the locally high achieved turbulent kinetic energy. Again, as it was in the previous OP1, the region in the east contains backflows. The west region of the outlet plane has maximum axial velocities. The SST $k-\omega$ model reaches higher maximum and lower minimum values.

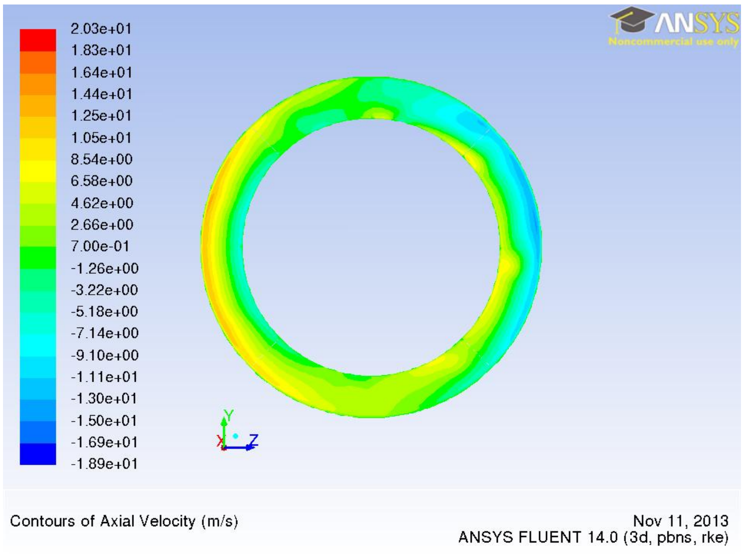

Figure 7.31: Axial velocity at outlet plane A 2OP, realizable $k-\epsilon$

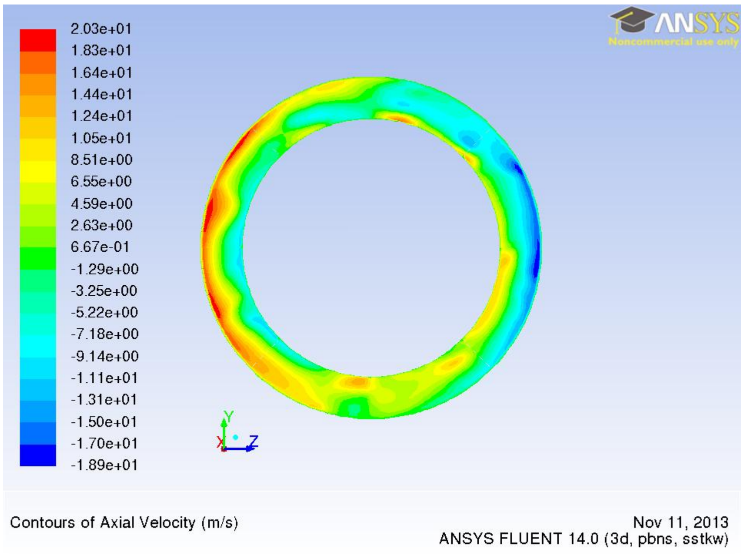

Figure 7.32: Axial velocity at outlet plane A 2OP, SST $k-\omega$

7.3 Simulation Results for the Third Operating Point

The data needed for the boundary conditions in the simulation of the full-load operating point as are obtained from chapter 3 Table 3.3. These simulation runs were initialized with the obtained solutions from OP2. The same methodology applied for the previous operating points will be used for OP3. The distribution of wall shear stress around a blade of the annulus will be used as indicator of convergence behaviour.

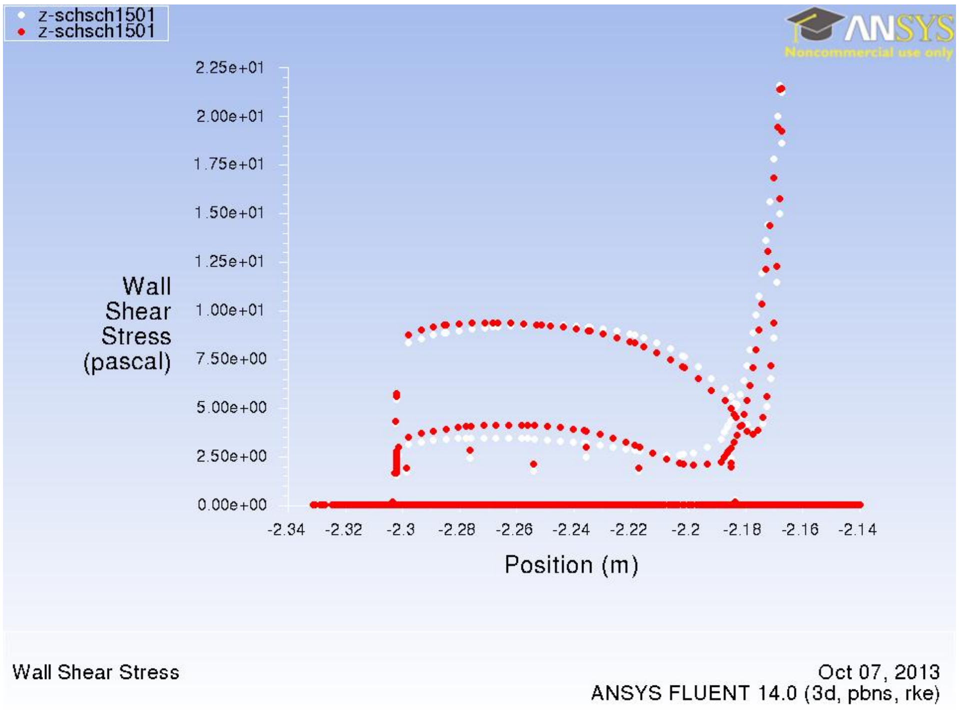

Figure 7.33: Wall shear stress around blade, realizable $k - \epsilon$

In Figure 7.33 the red distribution was achieved after 800 iterations and the white one was obtained after iteration 900. Small differences occur in the lower region of the wall shear stress at Position $-2,27m$ due to areas where flow separation occurs, because calculation was not able to achieve a steady solution.

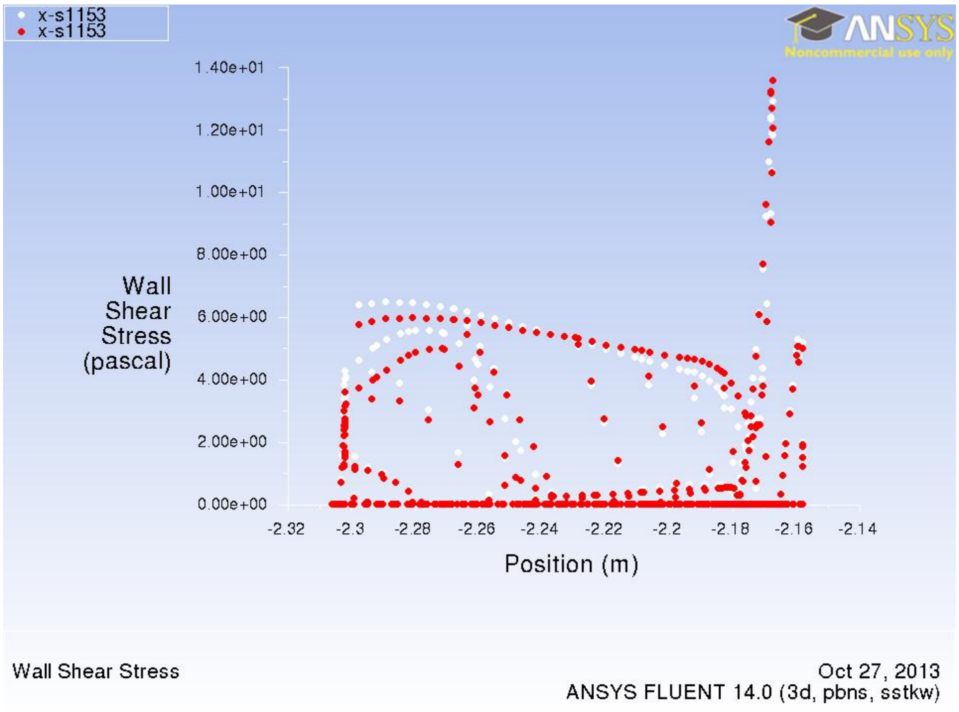

Figure 7.34: Wall shear stress around blade, SST $k - \omega$

In Figure 7.34 the red distribution was obtained at iteration 1000 and the white one shows the result after performing 100 additional iterations. Here a similar degree of convergence is achieved as in the previous realizable $k - \epsilon$ case.

The following Figures 7.35 and 7.36 show the obtained total temperature distribution for OP3.

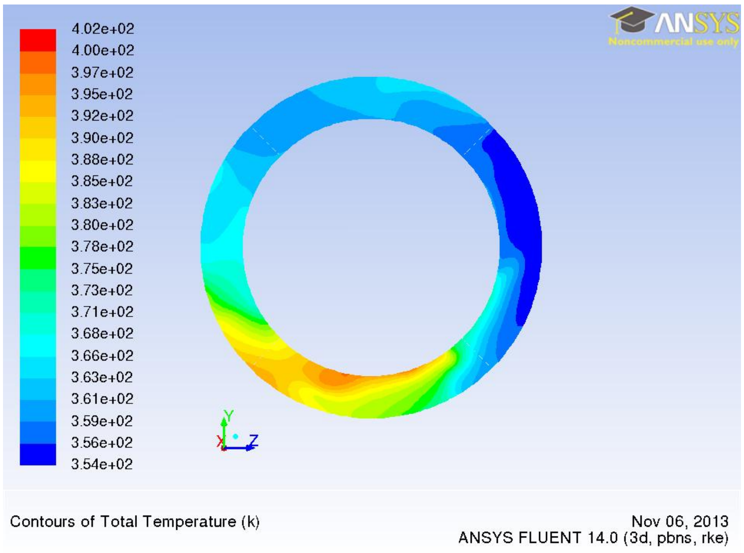

Figure 7.35: Total temperature at outlet plane A for OP3, realizable $k - \epsilon$

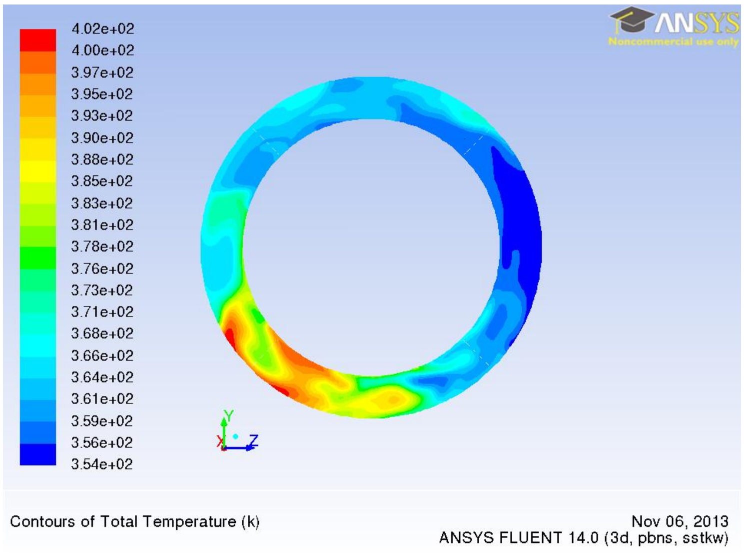

Figure 7.36: Total temperature at outlet plane A for OP3, SST $k - \omega$

The received distribution of total temperature from the realizable $k - \epsilon$ simulation has a hotspot in the south-west region, similar to the location of the hotspot form OP1. This makes sense, because for the actual OP3 the hotter air is provided from the GHH inlet coming from the brake compressor stationed in the test hall. The total temperature distribution obtained from SST $k - \omega$ simulation also detects the hotspot in this area, but the maximum total temperature achieved is $6K$ higher than in the realizable $k - \epsilon$ case. The colder region in the distribution of total temperature is in the west area of the outlet plane. Here, the results of the two turbulence models are similar. The obtained contours of total temperature for the two applied turbulence models show remarkable differences in general.

Figure 7.37 visualizes the turbine inlet total and average temperatures on the mid section of the outlet plane. Results obtained form the realizable $k-\epsilon$ and the SST $k-\omega$ model are compared. The diagram has an indicator included in the lower right corner to give information about the starting point of the plotted values and the coordinate axes.

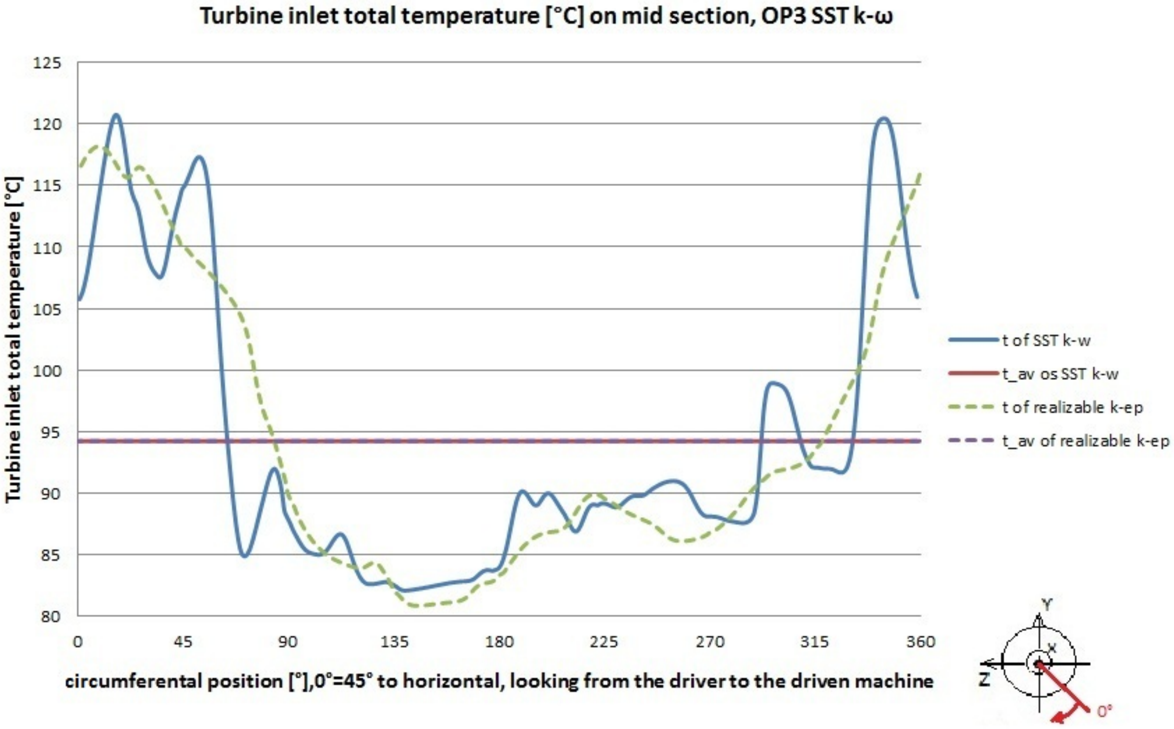

Figure 7.37: Turbine inlet total temperature for OP3

Figure 7.37 shows a matching tendency of the curves. The SST $k-\omega$ model generates a fluctuating total temperature distribution in comparison to the realizable $k-\epsilon$ model. The global minima and maxima are located almost at the same circumferential position. The obtained average total temperature by the different turbulent models is the same. Even though the tendency of the curves mentioned before is matching, it is impressive how different the two plots are.

A further comparison of the obtained mid section total temperatures of Figure 7.37 shall be done with measurement data.

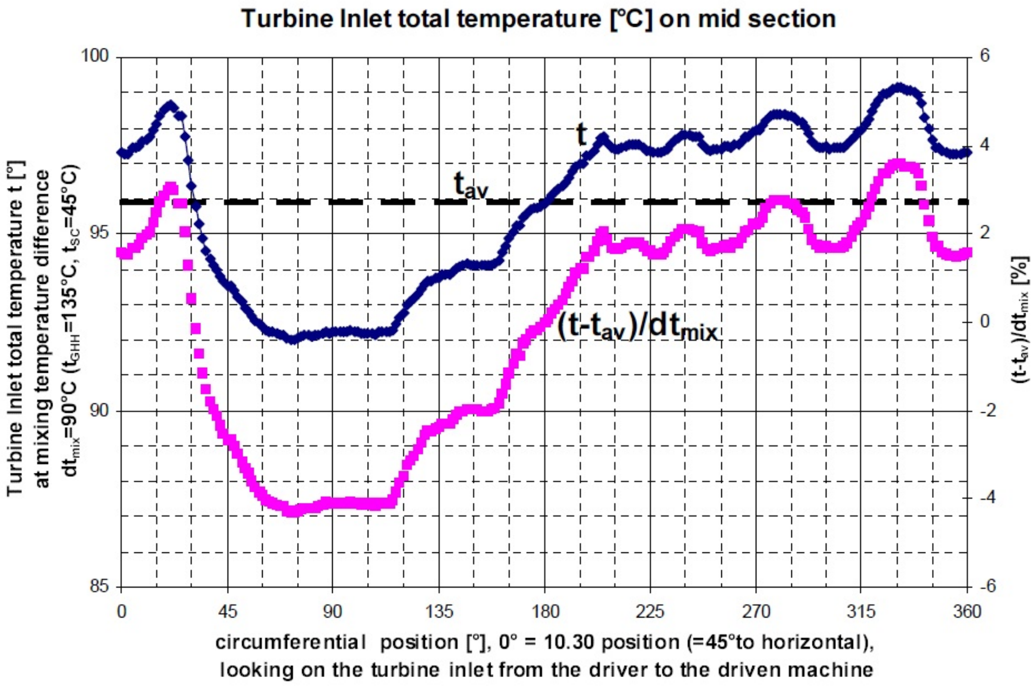

Figure 7.38: Mixer performance measurement of plane A

Figure 7.38 visualizes the mid section total and average temperature obtained from measurements performed in [4]. Since the only boundary conditions for this measurement OP, which was presented in [4] were the total temperatures at inlets, the other boundary conditions needed for the simulation case were obtained from [9]. This is a possible explanation for achieving different temperature distributions. Further arguments for obtaining results that are not matching this measurement data shall be presented in section 7.5.

Following Figures 7.39 and 7.40 show the total pressure distributions achieved in the simulation cases. The SST $k-\omega$ model produced a distribution of slightly higher total pressure than the realizable $k-\epsilon$ model, like it was before in the previous operating points. The three spots of lower pressure in the north-east region were detected by both simulations. The received distributions are almost homogeneous.

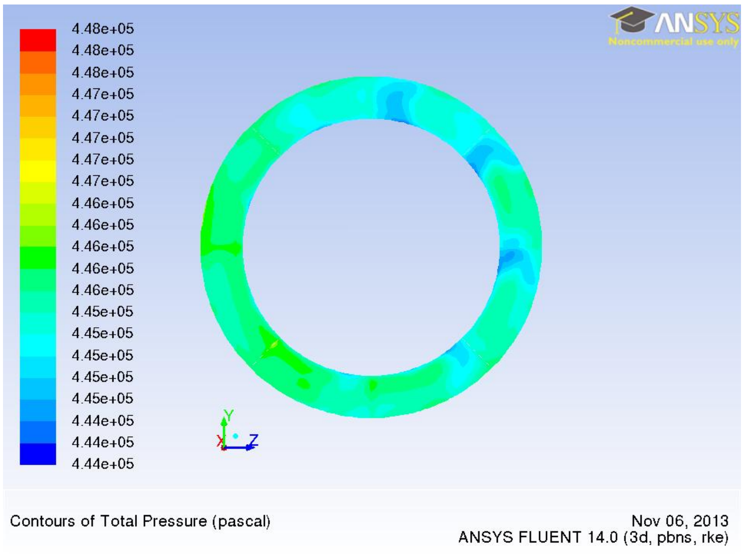

Figure 7.39: Total pressure at outlet plane A for OP3, realizable $k-\epsilon$

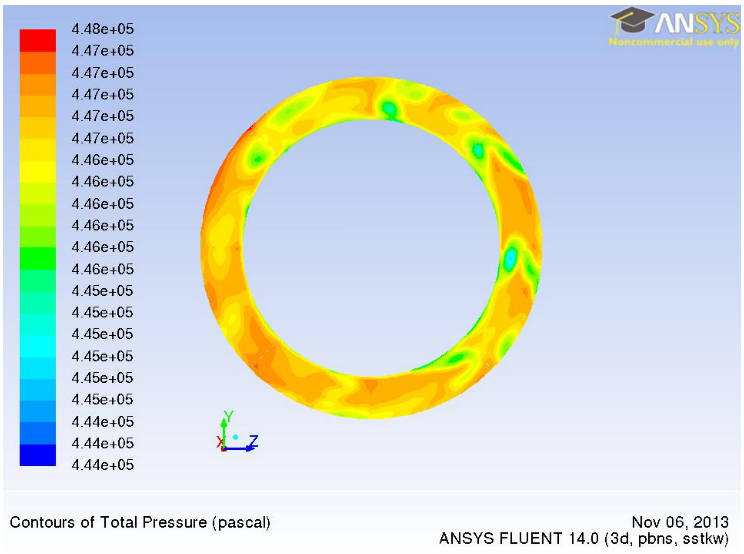

Figure 7.40: Total pressure at outlet plane A for OP3, SST $k-\omega$

Figures 7.41 and 7.42 the distribution of turbulent kinetic energy is shown. The realizable $k-\epsilon$ model achieved a higher maximum value than the SST $k-\omega$ model. The minimum value obtained from SST $k-\omega$ simulation is lower. The three spots of high values in the north-east region are detected in both simulation cases. The distribution of the SST $k-\omega$ model has two spots in the north-west region, which seem not to be present in the realizable $k-\epsilon$ results. On the other hand, the SST $k-\omega$ has not captured the west and south-west spots of higher turbulent kinetic energy the realizable $k-\epsilon$ model captured.

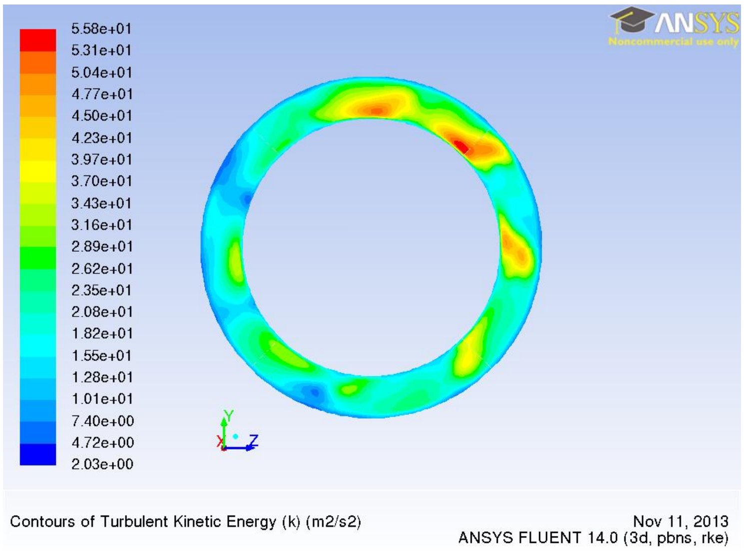

Figure 7.41: Turbulent kinetic energy at outlet plane A for OP3, realizable $k-\epsilon$

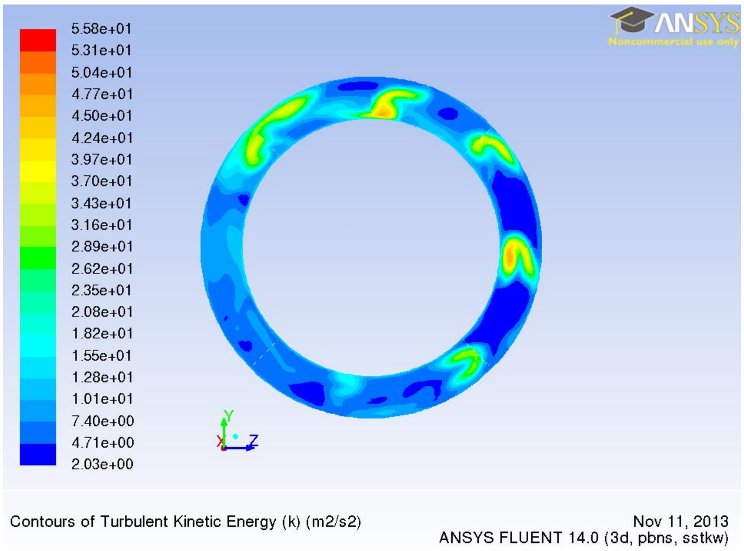

Figure 7.42: Turbulent kinetic energy at outlet plane A for OP3, SST $k-\omega$

Following Figures 7.43 and 7.44 of the axial velocity distribution at the outlet plane A of the Annulus will deliver an explanation for the high local values of turbulent kinetic energy. The east region of the outlet plane contains backflows and in the west has the maximum is located. The distribution of the SST $k-\omega$ model has achieved a lower minimum and a higher maximum value.

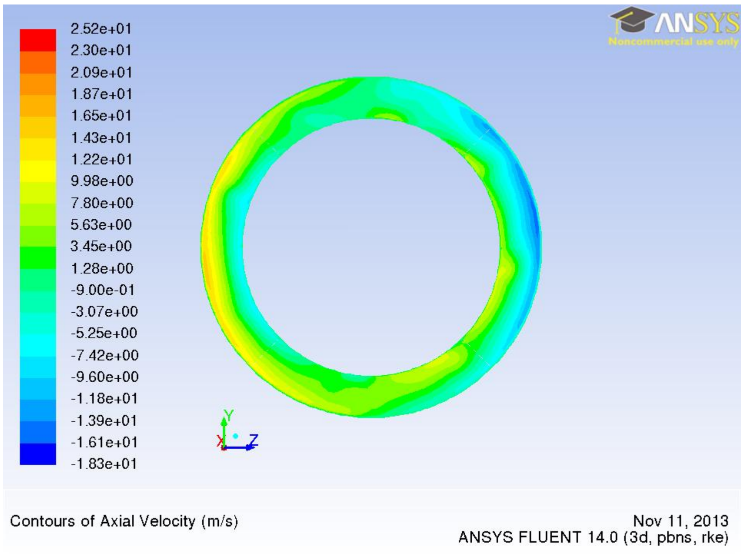

Figure 7.43: Axial velocity at outlet plane A for OP3, realizable $k-\epsilon$

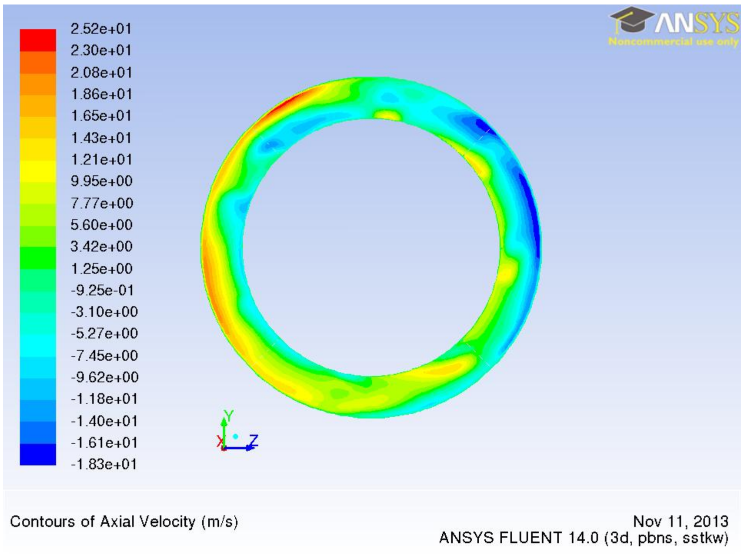

Figure 7.44: Axial velocity at outlet plane A for OP3, SST $k-\omega$

7.4 Weak Points and Potential Improvements

In this section a detailed flow analysis will be presented, to point out the problems the fluid flow encounters on the way through the chamber. Potential improvements will be mentioned. This will happen for results of the first part-load OP comparing realizable $k - \epsilon$ and SST $k - \omega$ simulations.

The following figures were produced with *CFD–Post V14.5* included in the CFX software package. The convenience of this tool is remarkable. Even for cases, such as the present one, containing numerous elements, work can be performed fast and efficiently.

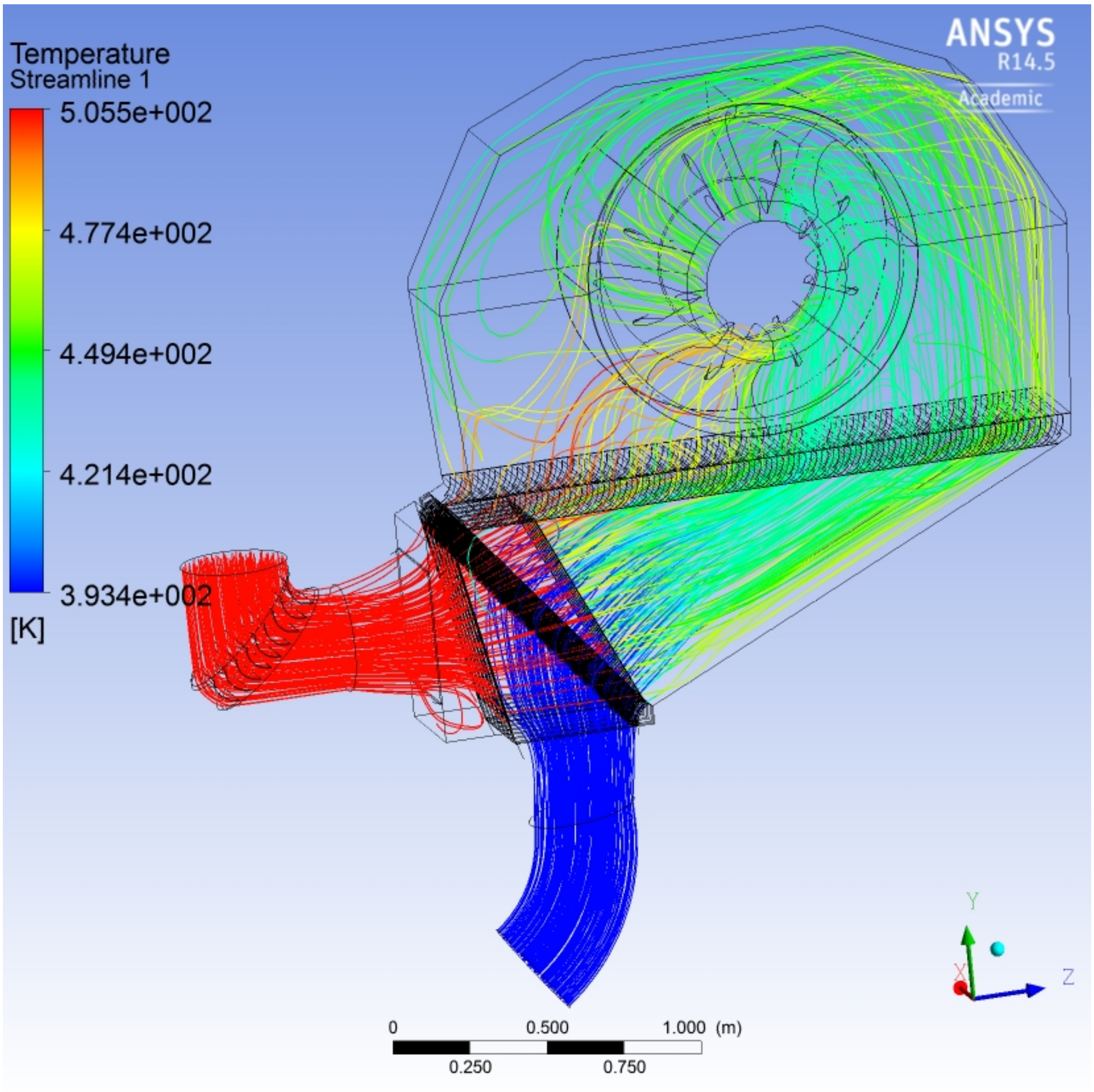

Figure 7.45: Temperature streamlines, realizable $k - \epsilon$

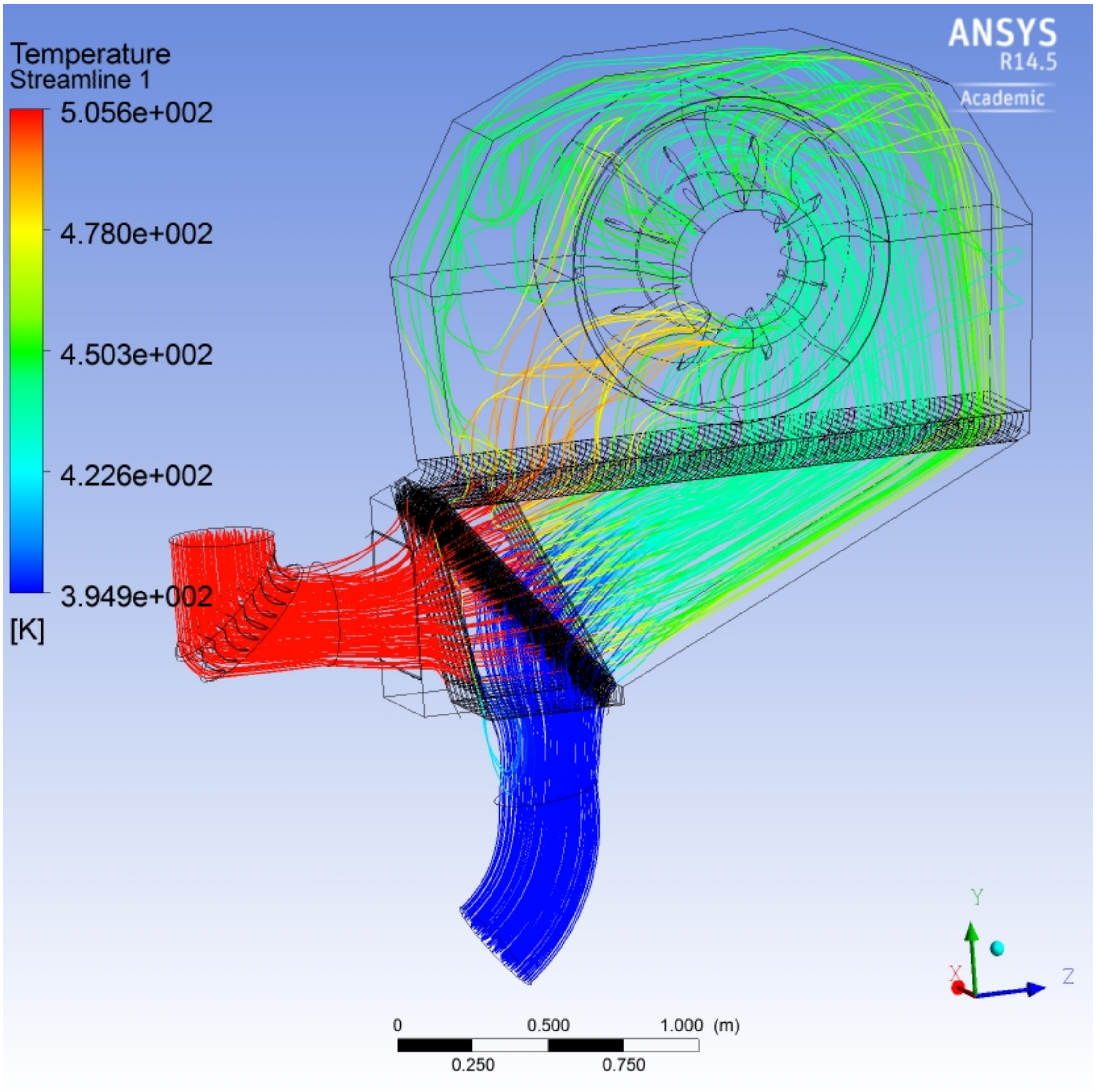

Figure 7.46: Temperature streamlines, SST $k - \omega$

Figures 7.45 and 7.46 illustrate the streamlines with their associated temperatures of the air flow from the inlets till the outlet of the mixing chamber.

The cold fluid flow of Inlet SC (blue streamlines) has the problem, that it cannot reach the upper section of the Mixer, mainly due to flow separation occurring in the funnel part after the elbow. Consequently, the flow leaves the Mixer only sideways to the right, at an early stage, entering the Mixing Zone.
The hot fluid flow (red stremlines) on the other hand, provided from the GHH brake compressor, leaves the Mixer sideways and at the upper side. Since there is no air provided by the Inlet SC on the upper side of the Mixer part, no mixing takes place there and the GHH fluid finds the way of less resistance to flow through the Tandem Cascade

to reach the Lower Casing partition and finally flow trough the Annulus where is leaves the outlet plane in the south-west region right where the hotspot is detected.

To visualize and explain the exact positions where problems occur the following figures will show two different cross sections through the whole chamber for the two applied turbulence models.

Figure 7.47 shows the streamlines of a cross section, which was positioned through a Main Blade partition of the Mixer to visualize the problems occurring in the air flow, provided from the station compressor in the basement. The first problem region is marked with an "A". Here, we can see flow separation in the funnel part of Inlet SC. The angle of aperture in this funnel part is to large. Therefore, the pressure gradient is reaching a level which is too high and flow separation occurs.
At position "B" in Figure 7.47 we can see, that no air, provided from Inlet SC, is reaching the upper region of the Mixer. This air leaves the Mixer to the right entering the Mixing Zone. Therefore, no cold air, which would be necessary for mixture is located there. The reasons for this are the elbow part of Inlet SC and the following funnel part, which obviously has a too large angle of aperture.

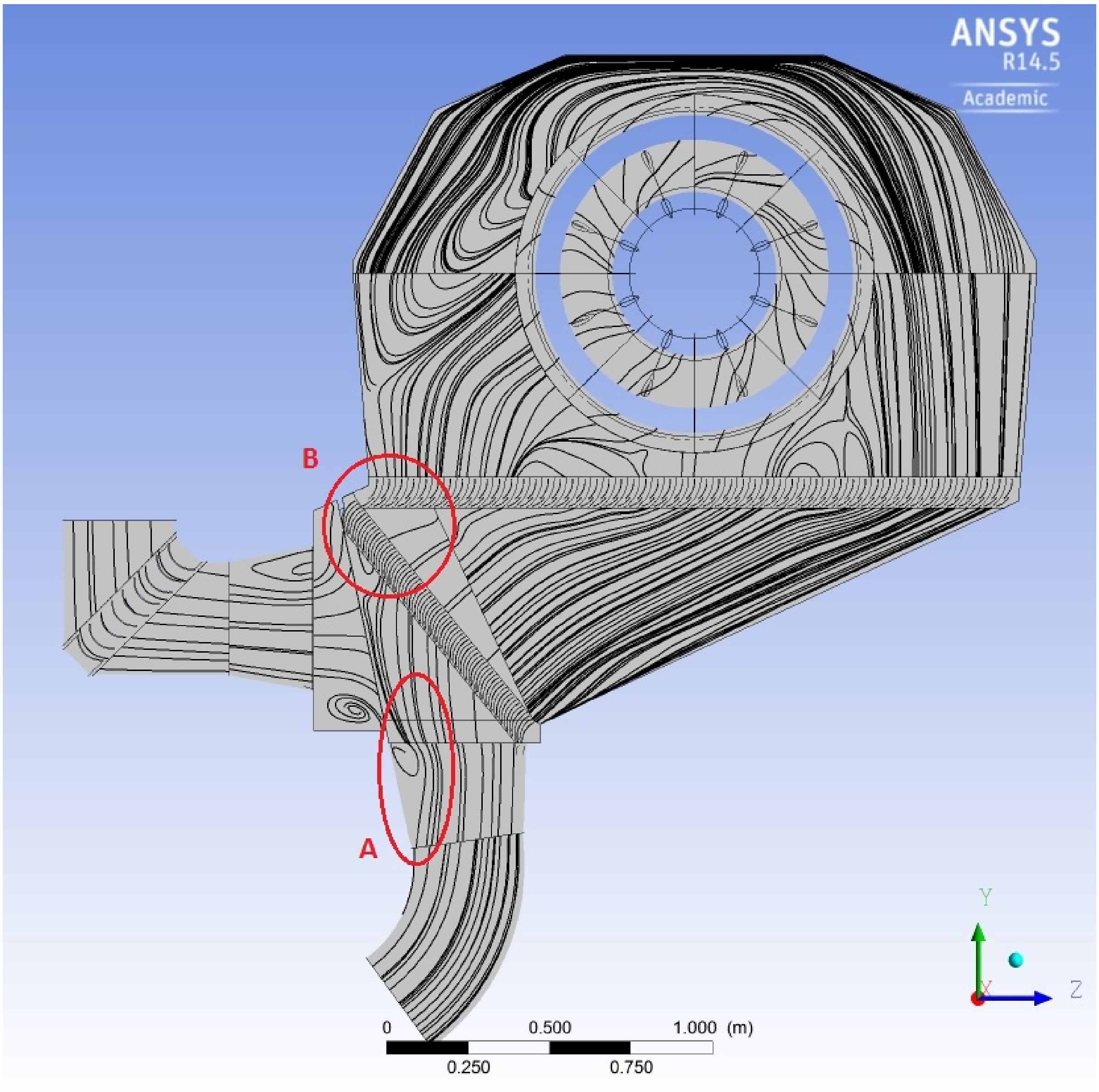

Figure 7.47: Streamline cross section through Main Blade, realizable $k - \epsilon$

Following Figure 7.48 shows the same occurrences, but presents the result of streamlines in the same cross section produced in SST $k-\omega$ simulation run. It is noticeable, that the SST $k-\omega$ simulation generates a larger region for "B", which is an explanation for achieving higher temperatures in the outlet plane of the Annulus see Figure 7.3 and 7.4.

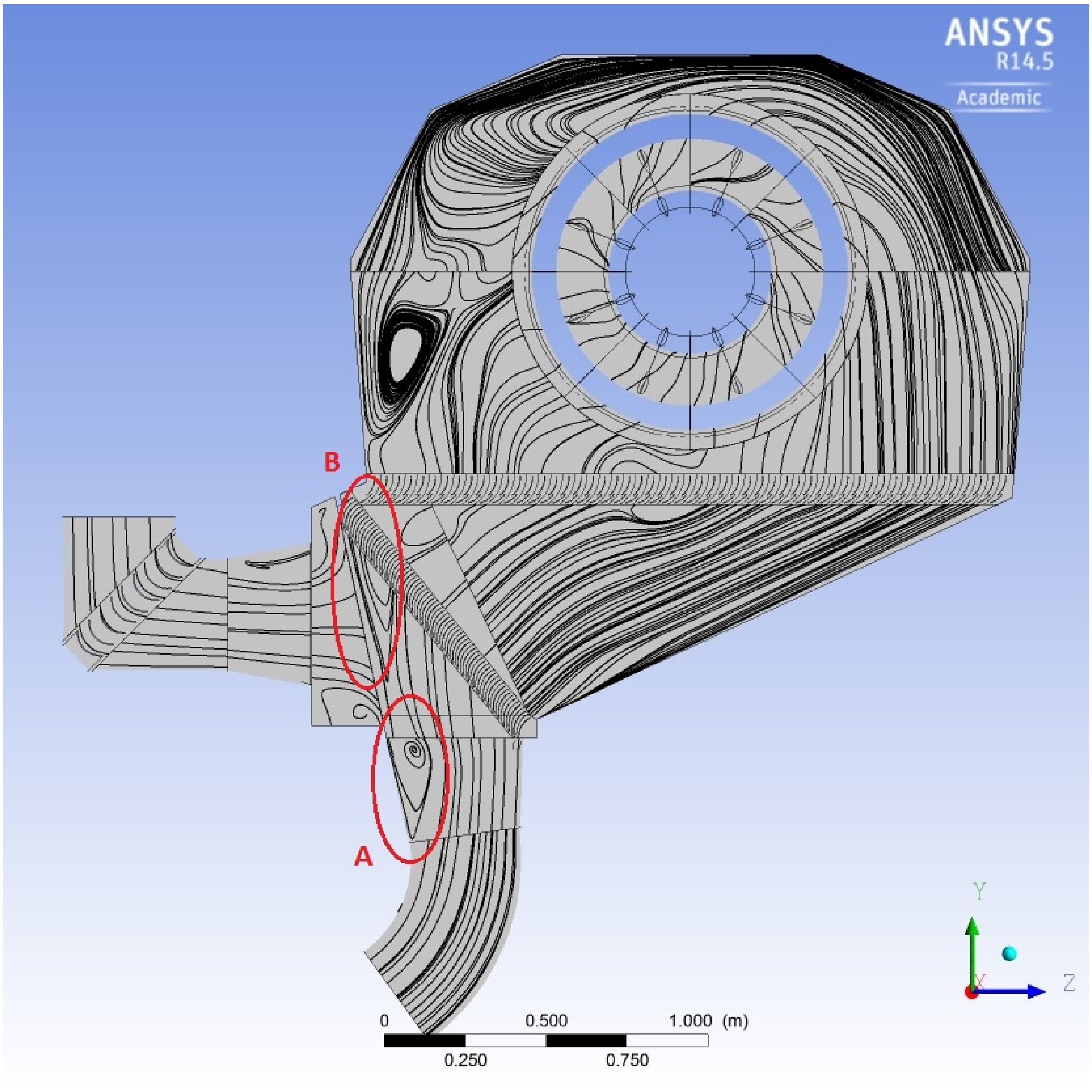

Figure 7.48: Streamline cross section through Main Blade, SST $k-\omega$

In Figure 7.49 the streamlines of a cross section positioned through a Channel of the Mixer are shown. Here, the flow provided from the GHH brake compressor can be analysed. We see two regions, where flow separation occurs. The first is indicated by a "C", occurs due to a too large angle of aperture of the funnel part from Inlet GHH. The pressure gradient is high, therefore the flow cannot follow the contour and separates, similar to the funnel part of Inlet SC. The second region where such a phenomenon occurs is marked by a "D". The reason for this flow separation is the sudden enlargement of cross section from the funnel part GHH4 to the Block part. Despite these regions of flow separation we see, that the air leaves the Mixer on the right and on the upper side.

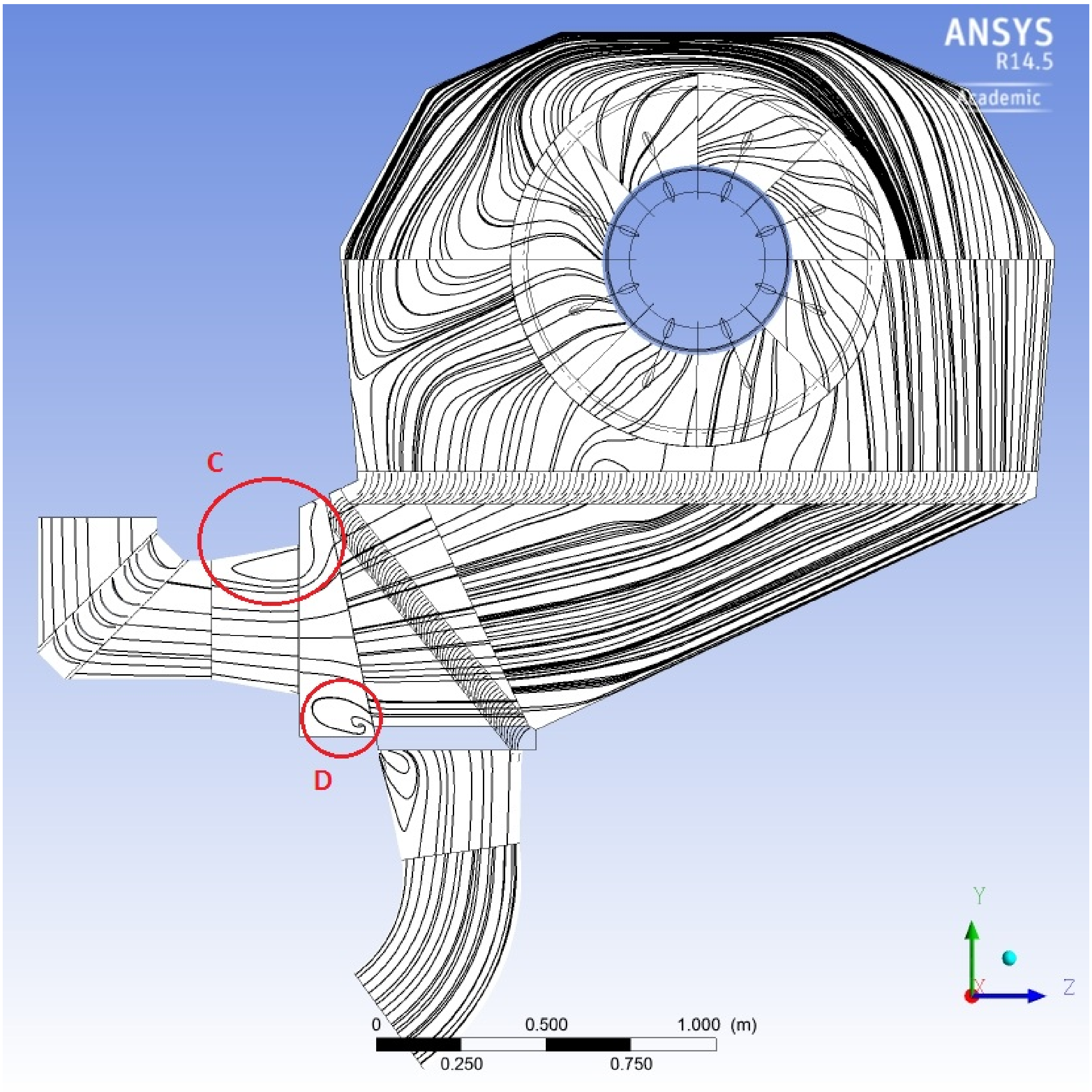

Figure 7.49: Streamline cross section through Channel, realizable $k - \epsilon$

Figure 7.50 visualizes the streamlines of the same cross section through the Channel partition of the Mixer for the SST $k-\omega$ simulation run. Occurrences are the same as mentioned before for Figure 7.49.

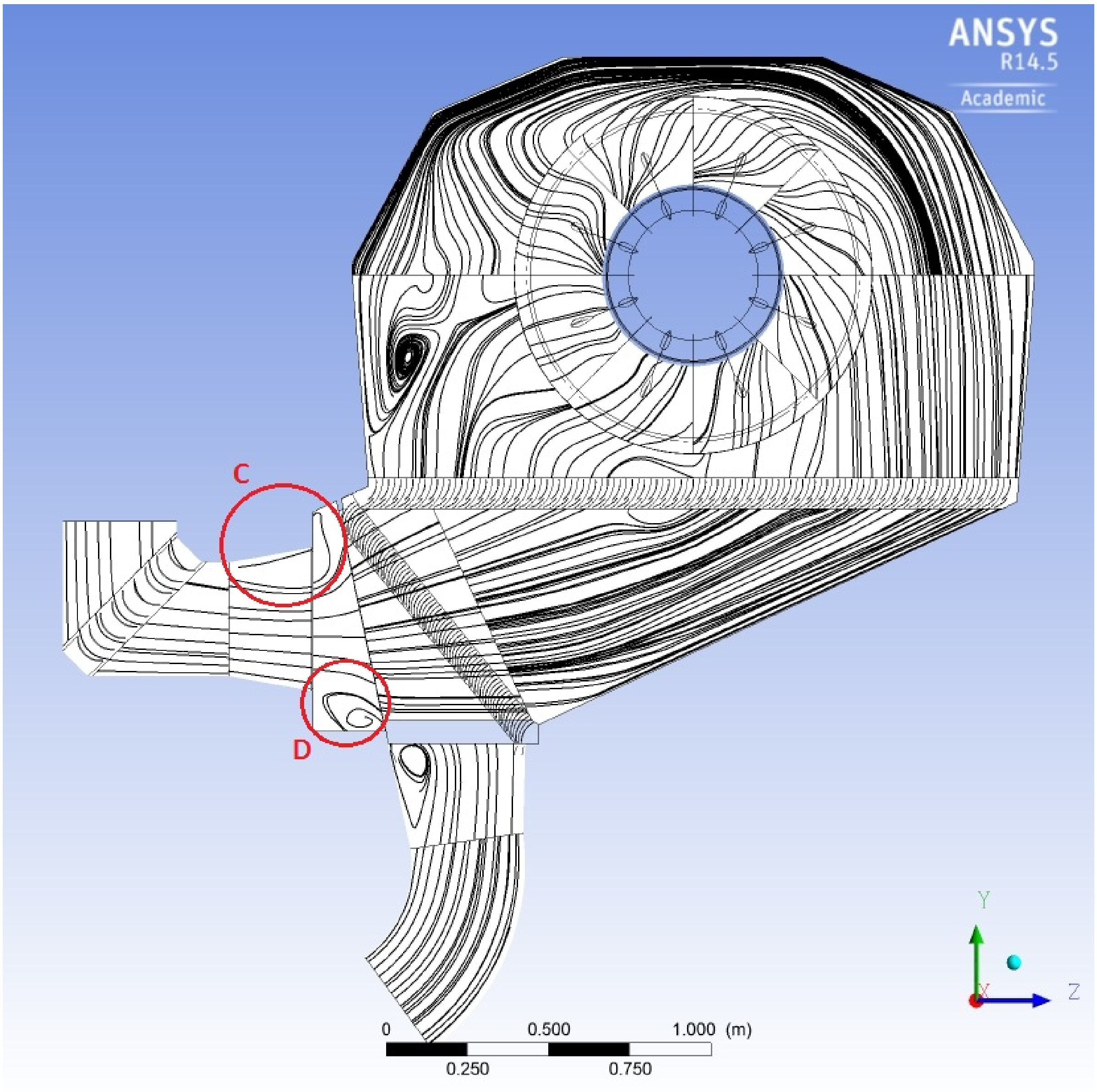

Figure 7.50: Streamline cross section through Channel, SST $k-\omega$

To illustrate the direction of flow velocity, especially in the backflow regions "A", "C" and "D" the following Figures 7.51 and 7.52 shall be presented. These figures show the velocity vectors in the same cross section as used for Figures 7.49 and 7.50.

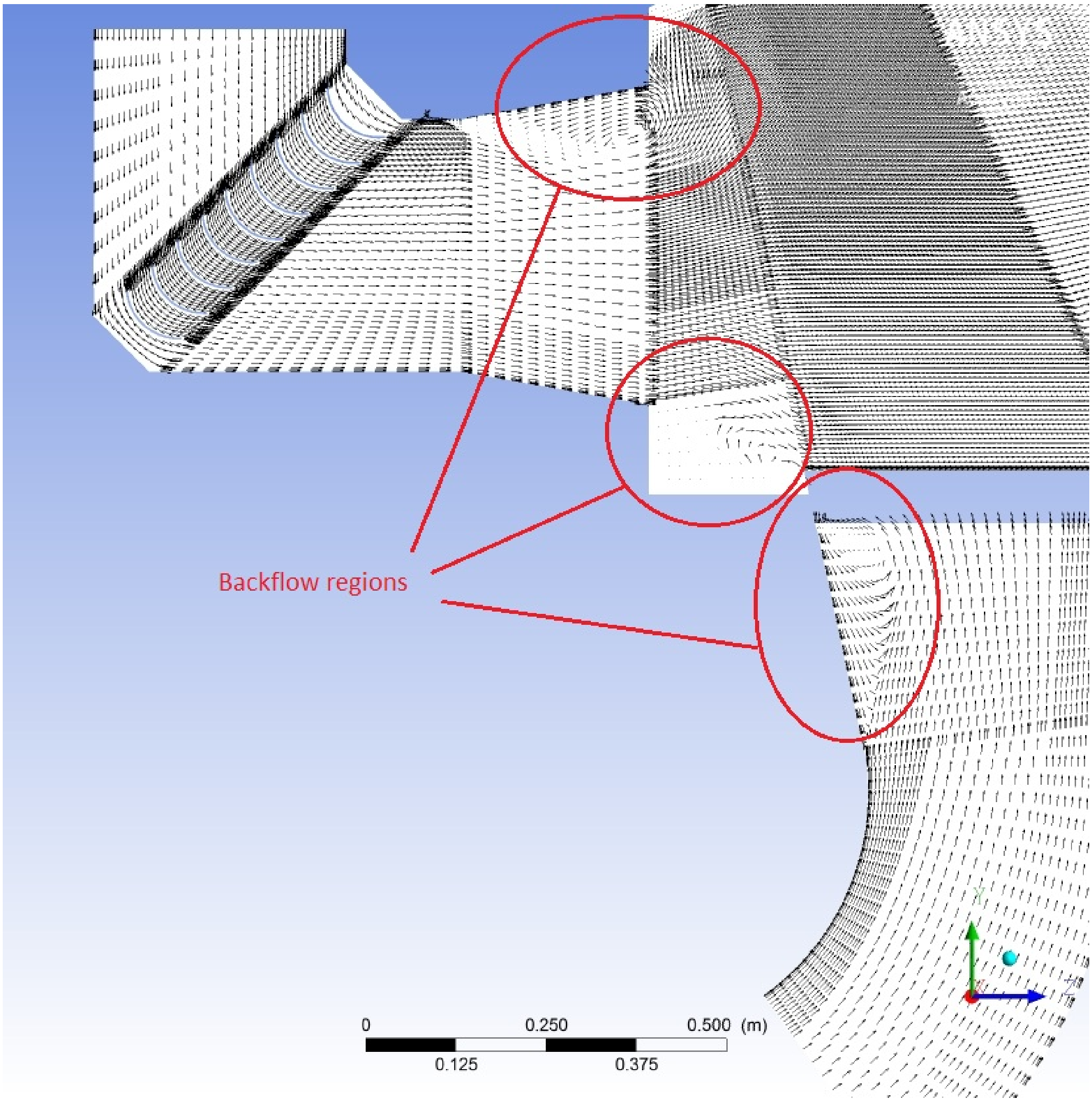

Figure 7.51: Velocity vectors in inlet domains, realizable $k-\epsilon$

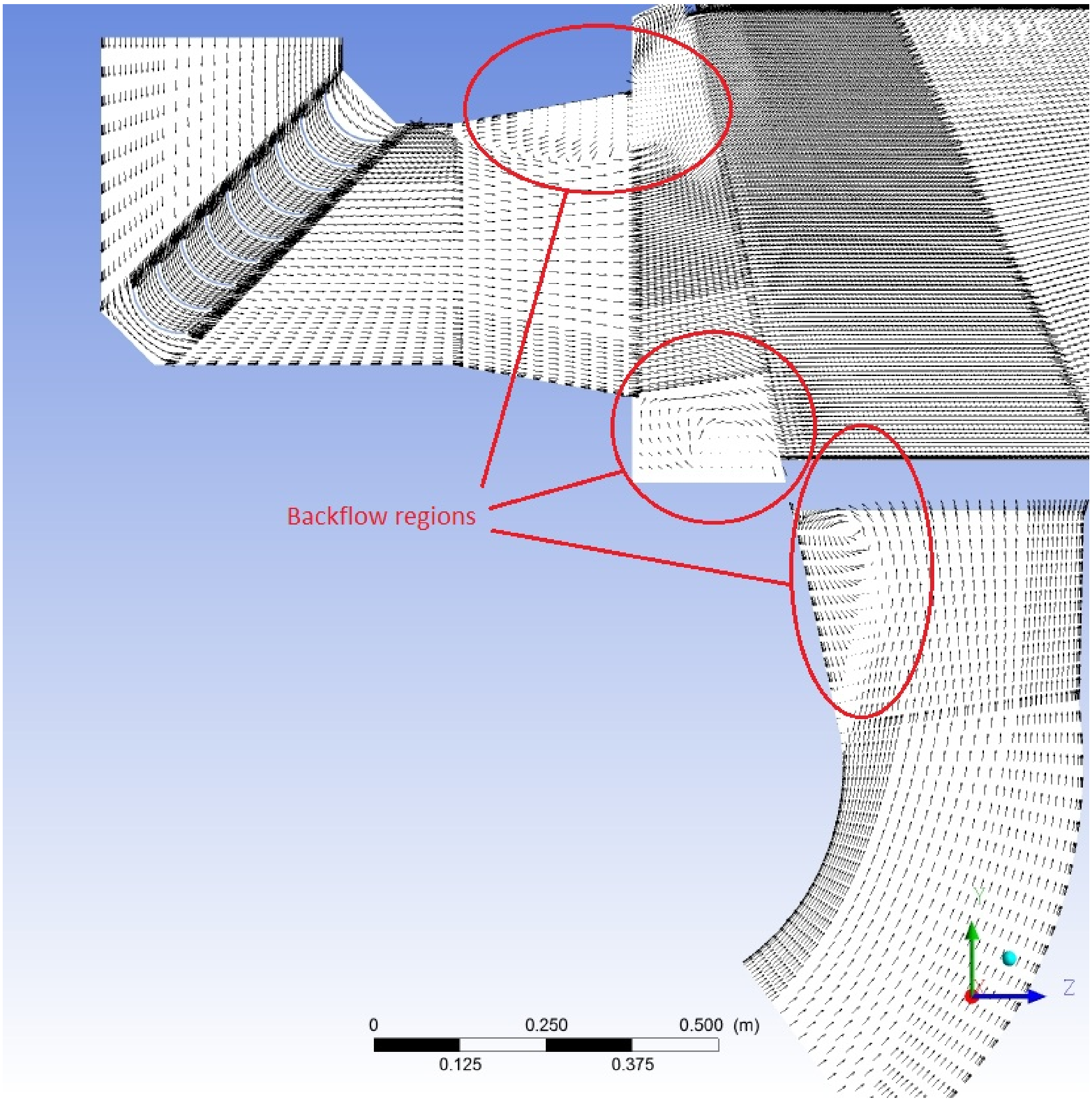

Figure 7.52: Velocity vectors in inlet domains, SST $k - \omega$

At this point an analysis of the temperature distributions at particular planes on the way through the mixing chamber shall be presented to explain the arising hotspot in the outlet plane of the Annulus. The order of presentation will be upstream starting at the outlet plane of the Lower Casing partition as shown in Figure 7.53 obtained from realizable $k - \epsilon$ simulation.

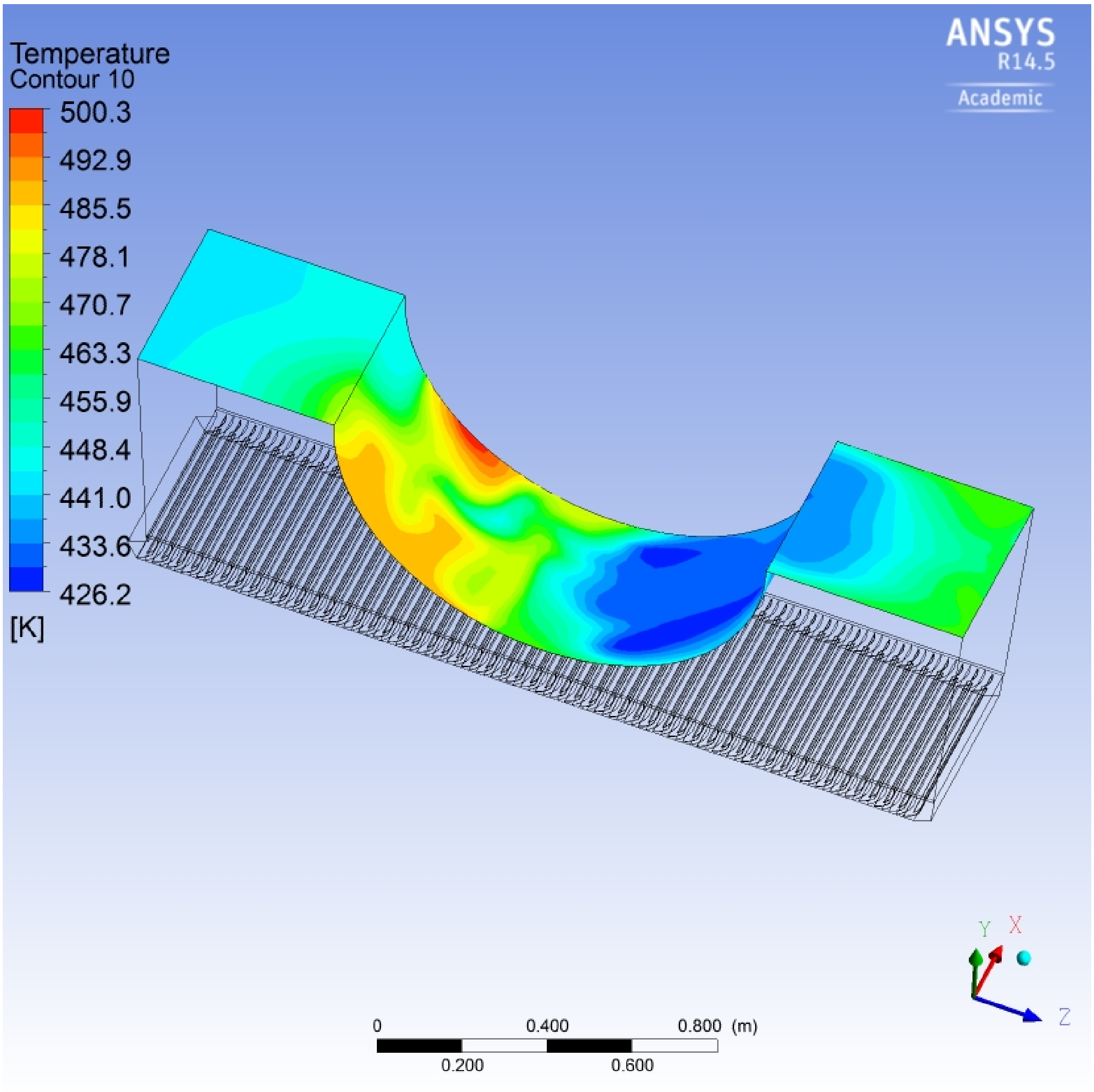

Figure 7.53: Temperature distribution at outlet of Lower Casing, realizable $k - \epsilon$

In the left region of the cut trough cylinder of Figure 7.53 temperatures of approximately $500K$ are detected. This air is only provided by the GHH brake compressor. At this late stage of the chamber this hot air will enter the annulus and finally reach the turbine inlet. So no mixing flow path will follow. In the rest of the temperature distribution acceptable mixing is performed proved by the legend of the figure, although the blue contribution on the right side of the cut through cylinder is dominated by air from the stationed compressor unit in the basement.

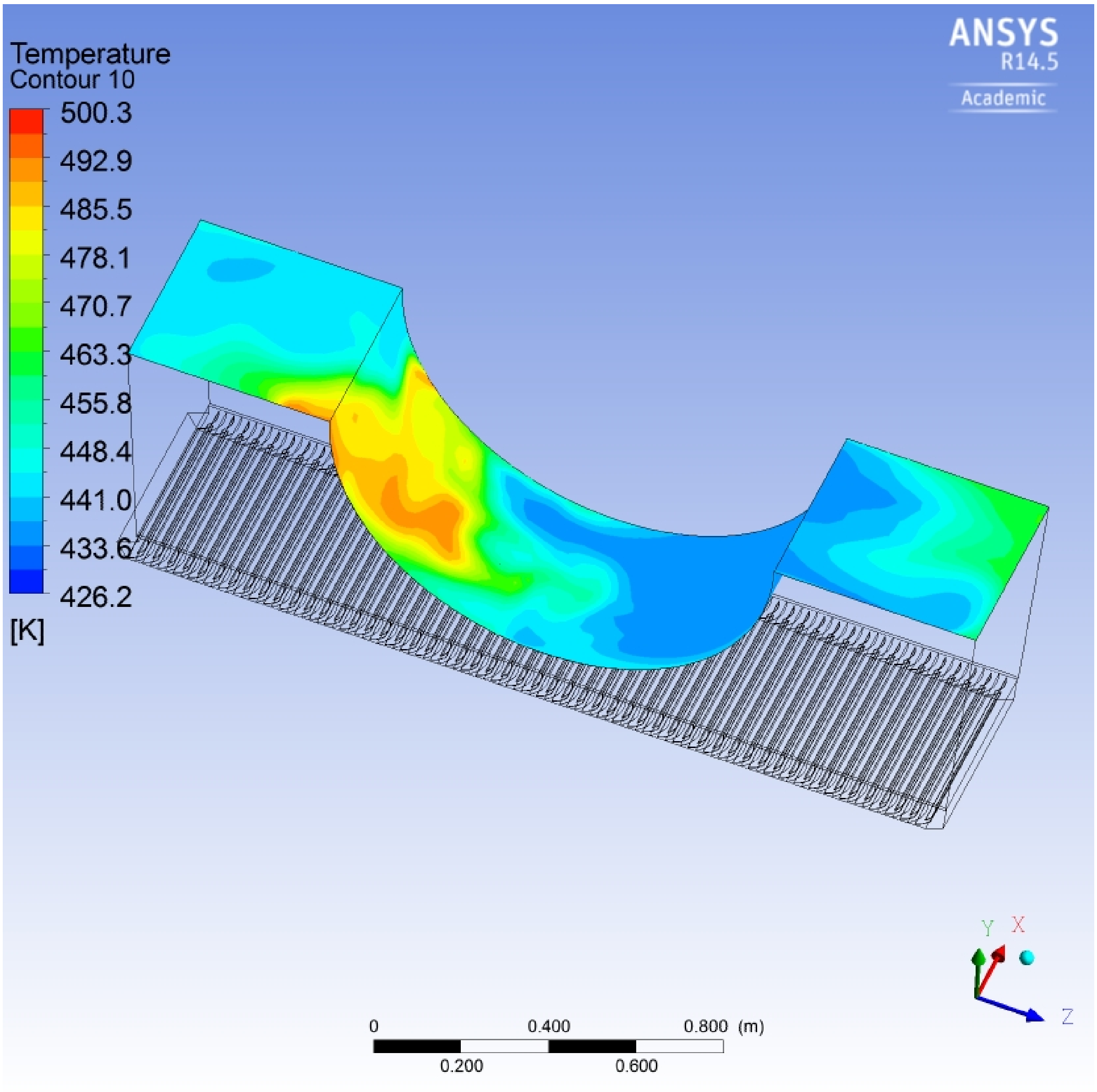

Figure 7.54: Temperature distribution at outlet of Lower Casing, SST $k-\omega$

In Figure 7.54 the total temperature distribution of the outlet plane from the Lower Casing partition is plotted. These results were obtained from the SST $k-\omega$ simulation run and can be compared to the previously discussed results of Figure 7.53. It can be mentioned that the left region of the cut through cylinder, where only pressurized air from the GHH inlet flows through, is larger and the hottest spots are assembled in the center of this cylinder half. Also the contours of air with same properties are different to the contours in realizable $k-\epsilon$ model. The SST $k-\omega$ model has a maximum temperature of about $490K$, which is lower the the maximum temperature of the realizable $k-\epsilon$ model.

Moving further upstream the next plane, where total temperature distributions shall be plotted is the outlet of the Tandem Cascade part. Again the results obtained from the two different turbulence models will be compared.

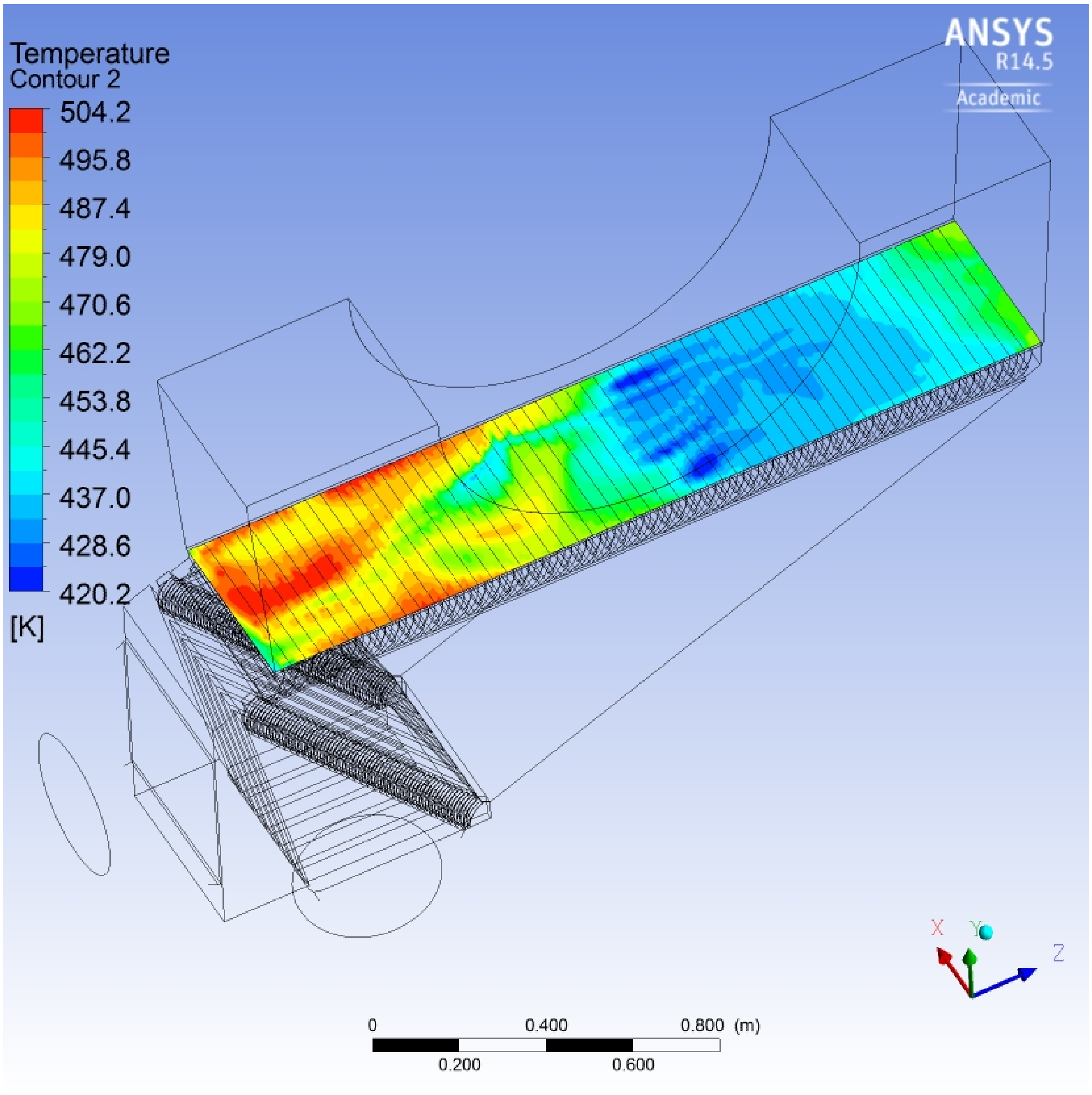

Figure 7.55: Total temperature distribution at outlet of Tandem Cascade, realizable $k-\epsilon$

Figure 7.55 shows the total temperature distribution on the outlet of the Tandem Cascade for realizable $k-\epsilon$ model. On the left side three hot areas, where pure GHH air flows through, can be seen. The rest of the distribution shows mixed up air. From the center to the right the contribution of air provided from SC inlet is dominating. Achieved maximum temperatures are at $504K$. The total temperature boundary condition applied at GHH inlet for OP1 are $504,7K$.

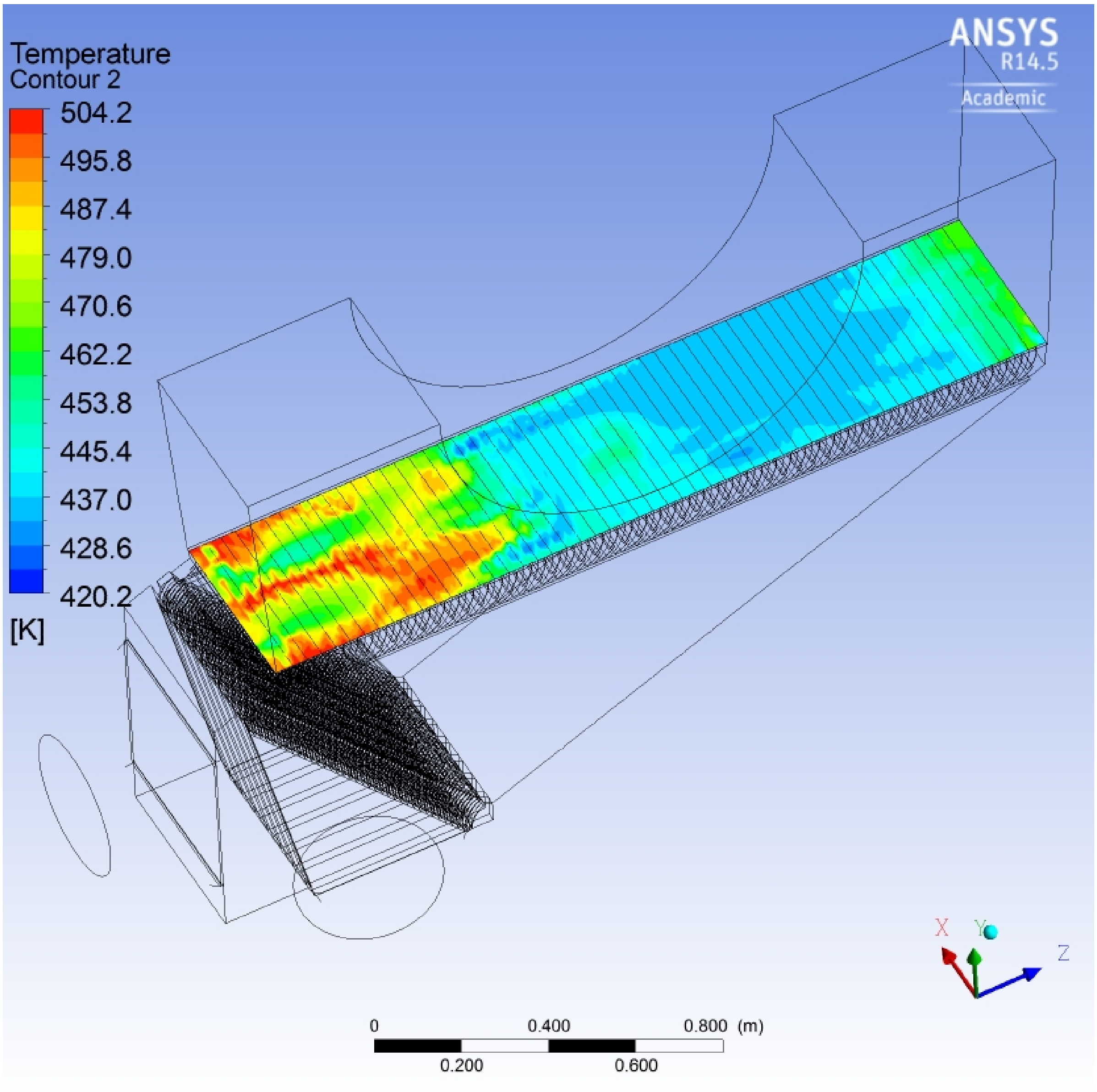

Figure 7.56: Temperature distribution at outlet of Tandem Cascade, SST $k-\omega$

Figure 7.56 shows the total temperature distribution at the outlet of the Tandem Cascade. The difference of temperature contours obtained from the two turbulence models is remarkable. The hotspots are located in the same region with the only difference, that the SST $k-\omega$ model has more hot air assembled in the area from the left to the center of the cascade. The realizable $k-\epsilon$ model assembles most of the hot air the center of the left end of the outlet plane as shown in Figure 7.55.

Following the way further upstream through the chamber the total temperature distribution on the outlet plane of the mixer part shall be shown in Figure 7.57.

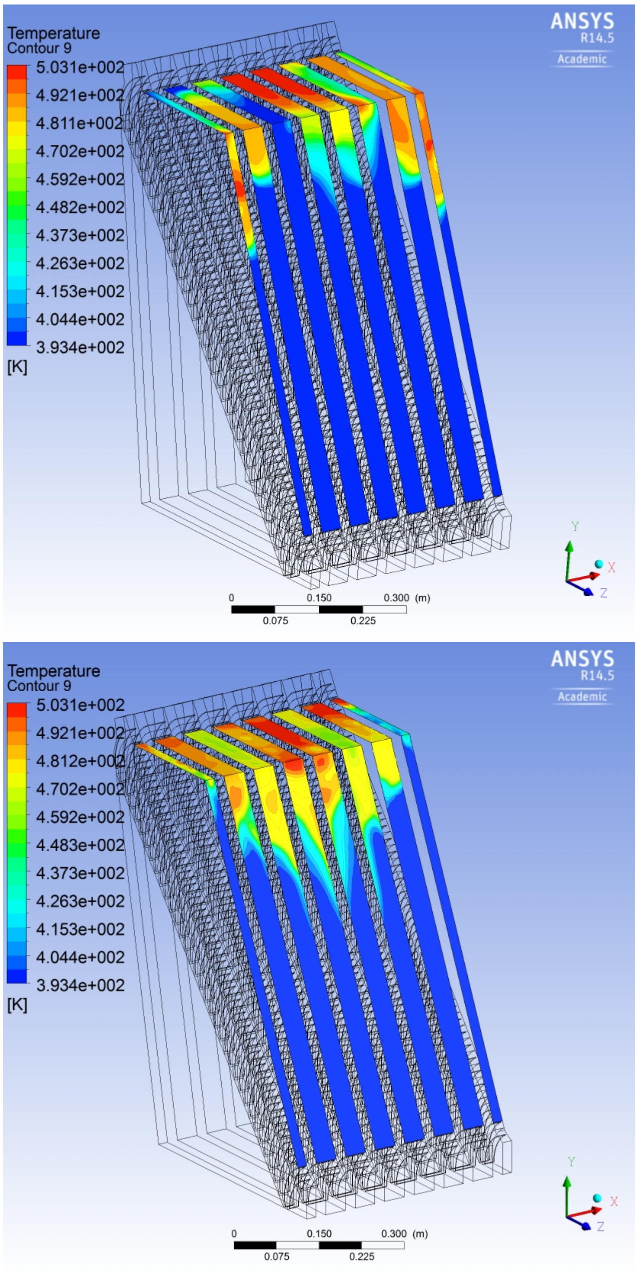

Figure 7.57: Total temperature distributions at outlet of Mixer part, realizable $k-\epsilon$ and SST $k-\omega$

The upper part of the Mixer is completely dominated by hot air provided from the GHH brake compressor. Both turbulence models capture this phenomenon, but again the difference between the obtained results is remarkable.

Following Figure 7.58 shows the velocity distribution on the outlet plane of the Mixer. The velocities in the upper region are lower than in the rest of the outlet plane. In the obtained results from the realizable $k-\epsilon$ simulation these regions widely spread in comparison to the SST $k-\omega$ results.

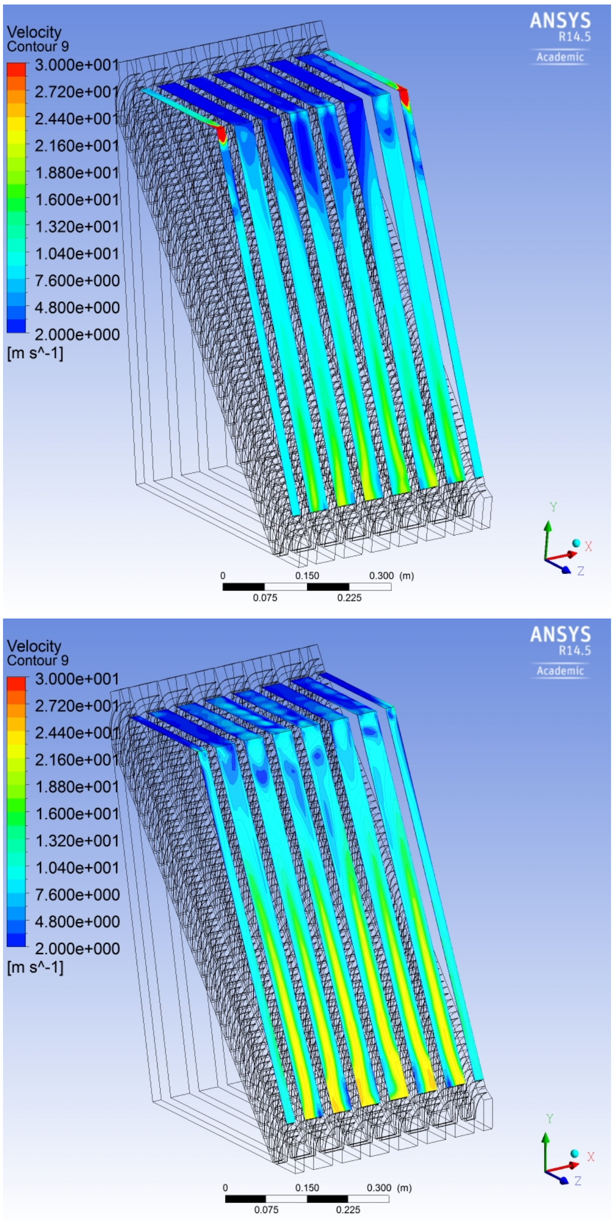

Figure 7.58: Velocity distributions at outlet of Mixer part, realizable $k-\epsilon$ and SST $k-\omega$

Based on the results potential improvements can be suggested. The analysis showed, that:

- The two funnel parts of the inlet domains acting as diffusers have the disadvantage, that the pressure gradient gets to high, with the consequence of flow separation. Replacing these parts by others, which do not have such a radical aperture angle should probably prevent such large areas of flow separation.
- Installing some guiding vanes in the elbow part of the SC inlet would force the fluid to reach the upper section of the Mixer part.
- The discontinuous, abrupt transition from the funnel of GHH inlet to the Block part is the reason for an additional area of backflow. The lower corner of the block part should be closed to achieve a smoother transition, where the flow can follow the geometry without occurring separation.
- The upper section of the Mixer is dominated by the GHH fluid. If the exit plane, which is also the inlet plane of the tandem cascade would be closed there, forcing all of the fluid flow to lower sections, the mixture with the SC fluid would be better, probably with the disadvantage of more pressure loss.
- In general, any modification of the chamber guaranteeing more mixing length would improve the situation.

7.5 Evaluation of Results

The obtained simulation results match with measurements in most regions of the outlet plane. Even if the distribution in some areas is not equal, the gradient of the analysed value is reproduced correctly.

The walls were modeled as adiabatic, because the residence time of fluid is relatively short and the heat transfer coefficient is small. Nevertheless, heat radiation could be a reason for different values of total temperature distribution in comparison to measurements.

Another important issue is, that in the stage of obtaining and analysing results, two absent guiding plates were detected in the CAD-model, right at the beginning of the Inlet SC domain, at the elbow, which were not modeled. These parts are shown in Figure 2.3 at Point 5. Obtained results show an intense flow separation at this elbow. Since guiding vanes are integrated there, this occurrence will probably not be so extreme. Now it can be claimed that these guiding vanes alone will not solve the problem of an inhomogeneous temperature distribution at the outlet plane of the mixing chamber.

For OP1 and OP2 the simulations with the SST $k - \omega$ as applied turbulence model the wall shear stress distribution over the blade of the annulus from Figures 7.2 and 7.21 would not be congruent even if more iterations would be performed. The reason for this are an unsteady flow with regions of flow separation.

The results of operating point 2 are quite different to the measurement data. The distributions would match well, if the results would be rotated for about 90 deg clock wisely. An explanation for this could be the missing guiding vanes in the elbow part of Inlet SC, in the CAD-model. Especially at this low part-load operating point the effect of flow separation in the funnel part is tremendous. The next Figure 7.59 shows the difference to Figure 7.51 of first part-load operating point of higher mass flow.

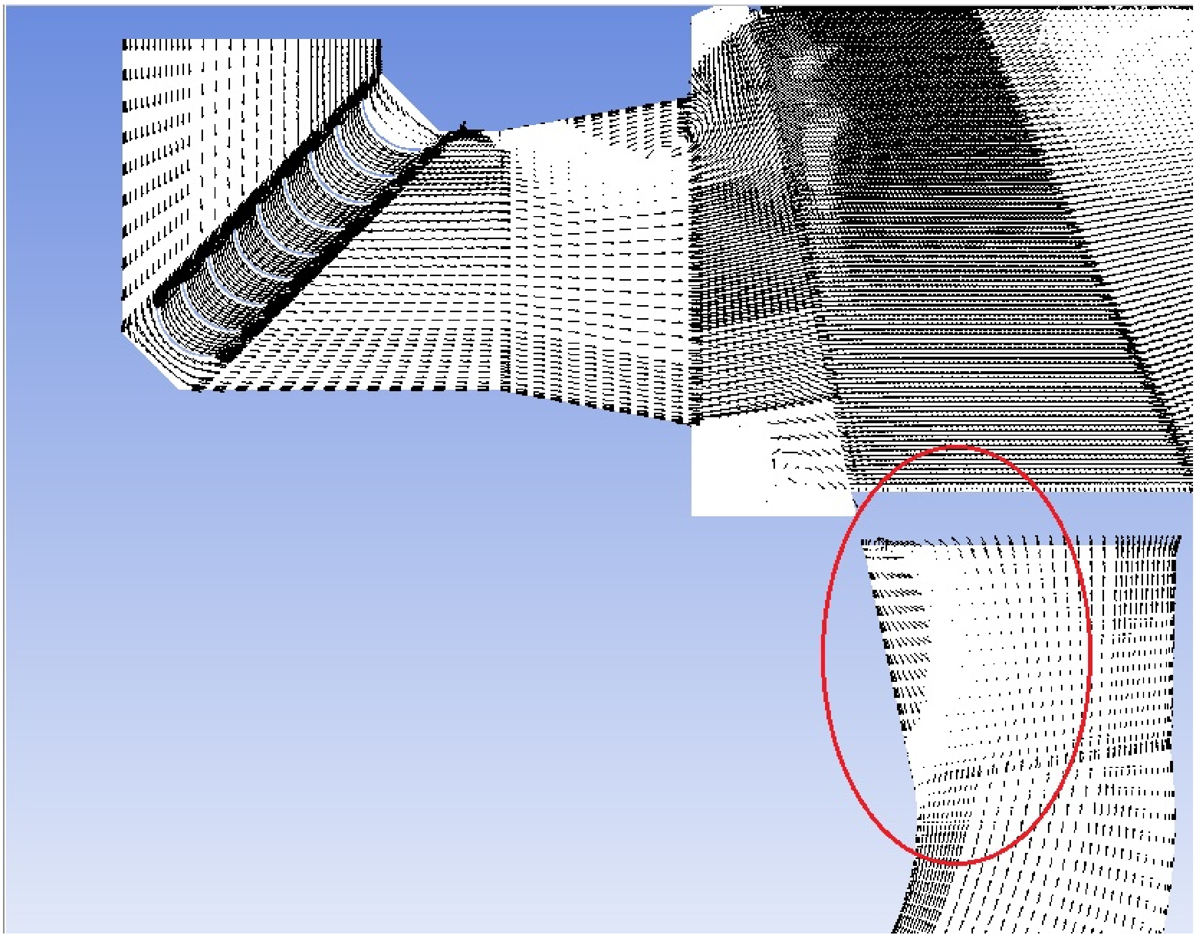

Figure 7.59: Flow separation in inlet domains, realizable $k-\epsilon$, OP2

8 Closing Words

It can be summarized, that this extensive analysis of the air flow through the mixing chamber of the test rig showed, that

- the inhomogeneities of temperature distribution, detected in measurements, were also confirmed by simulations
- dramatic flow separation occurs at Inlet SC and Inlet GHH
- guiding vanes at the elbow part of Inlet SC prevent large regions of flow separation tremendously, which is especially important when the mass flow is low
- only with the modification of guiding vanes in the elbow part of Inlet SC an homogeneous temperature distribution cannot be achieved
- the Mixer part has not optimal mixing properties
- the fluid flow through the Tandem Cascade partition at the side, where the inlets and the Mixer are located, basically consists only of GHH air and on the opposite side of the Tandem Cascade the flow is dominated by air from SC inlet
- mixing flow path of fluids is dimensioned too short
- the dependency on applied turbulence model is remarkable
- the hotspot movement of the temperature distribution on the outlet plane over the three operating points was confirmed by simulation.

Nomenclature

p	$[bar]$	pressure
T	$[K]$	temperature
n	$[rpm]$	rotational speed
P	$[W]$	power
$\dot{m}$	$[kg/s]$	mass flow
ρ	$[kg/m^3]$	density
t	$[s]$	time
$\vec{v}$	$[m/s]$	velocity
τ	$[N/m^2]$	shear stress
$\vec{f}$	$[N/m^3]$	force per volume unit
e	$[m^2/s^2]$	total inner energy per volume unit
Q	$[J/m^3]$	heat source
$\vec{x}$	$[m]$	position vector
μ	[kg/ms]	viscosity
q	$[W/m^2]$	heat flux
c_P	[J/kgK]	specific heat coefficient
Re	$[-]$	Reynolds number
Pr	$[-]$	Prandtl number
μ_t	$[m^2/s]$	turbulent viscosity
k	$[m^2/s^2]$	turbulent kinetic energy
ϵ	$[m^2/s^3]$	turbulent dissipation rate
ω	$[1/s]$	specific dissipation rate
R	$[J/molK]$	universal gas constant
M_W	$[kg/mol]$	molecular weight
S	$[K]$	Sutherland constant
CFL	$[-]$	Courant-Friedrichs-Lewy Number

Abbreviations

CFD	Computational Fluid Dynamics
CAD	Computer Aided Design
RAM	Random Access Memory
OP	Operating Point
RSM	Reynolds Stress Model

List of Figures

1.1 Turbine test rig 9

2.1 Transonic test-turbine facility flow scheme 12
2.2 Test rig with ways of air supply 13
2.3 Turbine inlet concept, showing GHH- and compressor station inlets, mixer and tandem cascade in section D-D 14

4.1 Finite Volume Cell 22

5.1 Geometrical elements: Hexahedron, Prism, Tetrahedron 26
5.2 Topology of solid adapted, structured grids 27
5.3 Geometry of mixing chamber 28
5.4 Interior geometry of mixing chamber with different flow domains 29
5.5 Partitions of inlet domains 30
5.6 Partitions of Mixer from SC side 31
5.7 Partitions of Mixer from GHH side 31
5.8 Domain of annulus 32
5.9 Hierarchy ANSYS ICEMcfd 33
5.10 Flow of fluids in diagonal blade rows part 34
5.11 Leading edge of channel 34
5.12 Blocking of SC1 39
5.13 Mesh of SC1 39
5.14 Blocking of SC2 39
5.15 Mesh of SC2 39
5.16 Blocking of GHH1 40
5.17 Mesh of GHH1 40
5.18 Blocking of GHH2 40
5.19 Mesh of GHH2 40
5.20 Blocking of GHH3 41
5.21 Mesh of GHH3 41
5.22 Blocking of GHH4 41
5.23 Mesh of GHH4 41
5.24 Blocking of Preblock 42
5.25 Mesh of Preblock 42
5.26 Blocking of Block 42
5.27 Mesh of Block 42
5.28 Blocking of Channels 43

5.29 Mesh of Channels 43
5.30 Blocking of Side IN 43
5.31 Mesh of Side IN 43
5.32 Blocking of Main IN 44
5.33 Mesh of Main IN 44
5.34 Blocking of Side Blades 44
5.35 Mesh of Side Blades 44
5.36 Blocking of Main Blades 45
5.37 Mesh of Main Blades 45
5.38 Blocking of Side OUT 45
5.39 Mesh of Side OUT 45
5.40 Blocking of Main OUT 46
5.41 Mesh of Main OUT 46
5.42 Blocking of Mixing Zone 46
5.43 Mesh of Mixing Zone 46
5.44 Blocking of Tandem Cascade 47
5.45 Mesh of Tandem Cascade 47
5.46 Blocking of Lower Casing 47
5.47 Mesh of Lower Casing 47
5.48 Blocking of Upper Casing 48
5.49 Mesh of Upper Casing 48
5.50 Blocking of Annulus 48
5.51 Mesh of Annulus 48

6.1 Interface Connections 52
6.2 Grid Check 53
6.3 Grid Information 53
6.4 Fluent V14, User interface 56

7.1 Wall shear stress around blade for OP1, realizable $k - \epsilon$ 60
7.2 Wall shear stress around blade for OP1, SST $k - \omega$ 61
7.3 Total temperature at outlet plane A for OP1, realizable $k - \epsilon$ 62
7.4 Total temperature at outlet plane A for OP1, SST $k - \omega$ 62
7.5 Total temperature at outlet plane A for OP1, RSM 62
7.6 Total temperature at outlet plane A for OP1, measurements 62
7.7 Turbine inlet total temperature for OP1 63
7.8 Streamlines upstream the outlet plane A for OP1, realizable $k - \epsilon$ 64
7.9 Streamlines upstream the outlet plane A for OP1, SST $k - \omega$ 64
7.10 Total pressure at outlet plane A for OP1, realizable $k - \epsilon$ 66
7.11 Total pressure at outlet plane A for OP1, SST $k - \omega$ 66
7.12 Total pressure at outlet plane A for OP1, RSM 66
7.13 Total pressure at outlet plane A for OP1, measurements 66
7.14 Turbulent kinetic energy at outlet plane A for OP1, realizable $k - \epsilon$ 68
7.15 Turbulent kinetic energy at outlet plane A for OP1, SST $k - \omega$ 68

7.16 Turbulent kinetic energy at outlet plane A for OP1, RSM 68
7.17 Axial velocity at outlet plane A for OP1, realizable $k-\epsilon$ 70
7.18 Axial velocity at outlet plane A for OP1, SST $k-\omega$ 70
7.19 Axial velocity at outlet plane A for OP1, RSM 70
7.20 Wall shear stress around blade, realizable $k-\epsilon$ 72
7.21 Wall shear stress around blade, SST $k-\omega$ 73
7.22 Total temperature at outlet plane A for OP2, realizable $k-\epsilon$ 74
7.23 Total temperature at outlet plane A for OP2, SST $k-\omega$ 74
7.24 Total temperature at outlet plane A for OP2, measurements 74
7.25 Turbine inlet total temperature for OP2 75
7.26 Total Pressure at outlet 2OP, realizable $k-\epsilon$ 77
7.27 Total Pressure at outlet 2OP, SST $k-\omega$ 77
7.28 Total Pressure at outlet 2OP, measurements 77
7.29 Turbulent kinetic energy at outlet plane A 2OP, realizable $k-\epsilon$ 78
7.30 Turbulent kinetic energy at outlet plane A 2OP, SST $k-\omega$ 78
7.31 Axial velocity at outlet plane A 2OP, realizable $k-\epsilon$ 79
7.32 Axial velocity at outlet plane A 2OP, SST $k-\omega$ 79
7.33 Wall shear stress around blade, realizable $k-\epsilon$ 80
7.34 Wall shear stress around blade, SST $k-\omega$ 81
7.35 Total temperature at outlet plane A for OP3, realizable $k-\epsilon$ 82
7.36 Total temperature at outlet plane A for OP3, SST $k-\omega$ 82
7.37 Turbine inlet total temperature for OP3 83
7.38 Mixer performance measurement of plane A 84
7.39 Total pressure at outlet plane A for OP3, realizable $k-\epsilon$ 85
7.40 Total pressure at outlet plane A for OP3, SST $k-\omega$ 85
7.41 Turbulent kinetic energy at outlet plane A for OP3, realizable $k-\epsilon$ . . . 86
7.42 Turbulent kinetic energy at outlet plane A for OP3, SST $k-\omega$ 86
7.43 Axial velocity at outlet plane A for OP3, realizable $k-\epsilon$ 87
7.44 Axial velocity at outlet plane A for OP3, SST $k-\omega$ 87
7.45 Temperature streamlines, realizable $k-\epsilon$ 88
7.46 Temperature streamlines, SST $k-\omega$ 89
7.47 Streamline cross section through Main Blade, realizable $k-\epsilon$ 91
7.48 Streamline cross section through Main Blade, SST $k-\omega$ 92
7.49 Streamline cross section through Channel, realizable $k-\epsilon$ 93
7.50 Streamline cross section through Channel, SST $k-\omega$ 94
7.51 Velocity vectors in inlet domains, realizable $k-\epsilon$ 95
7.52 Velocity vectors in inlet domains, SST $k-\omega$ 96
7.53 Temperature distribution at outlet of Lower Casing, realizable $k-\epsilon$ . . . 97
7.54 Temperature distribution at outlet of Lower Casing, SST $k-\omega$ 98
7.55 Total temperature distribution at outlet of Tandem Cascade, realizable $k-\epsilon$ 99
7.56 Temperature distribution at outlet of Tandem Cascade, SST $k-\omega$ 100
7.57 Total temperature distributions at outlet of Mixer part, realizable $k-\epsilon$ and SST $k-\omega$ 101

7.58 Velocity distributions at outlet of Mixer part, realizable $k - \epsilon$ and SST $k - \omega$ 102
7.59 Flow separation in inlet domains, realizable $k - \epsilon$, OP2 105

List of Tables

2.1 Design Point at 11000rpm 15
2.2 TTM-Stage Parameters 15

3.1 Measurement data of Part-load Operating Point 1 17
3.2 Measurement data of Part-load Operating Point 2 17
3.3 Measurement data of Full-load Operating Point 17

4.1 Description of turbulence and wall model 25

Bibliography

[1] J.H. Ferzinger, M. Perić **Computational Methods for Fluid Dynamics**, 3rd Edition, Springer Verlag Berlin Heidelberg 2002

[2] R. Byron Bird, Warren E. Stewart, Edwin N. Lightfoot **Transport Phenomena**, 2nd Edition, John & Wiley Sons Inc. 2002

[3] H. Örtel, E. Laurien **Numerische Strömungsmechanik**, Springer Verlag Berlin Heidelberg 1995

[4] J. Erhard **Design, Construction and Commisioning of a Transsonic Test-Turbine Facility**, PhD Thesis 2000

[5] J.Hubinka **Konstruktion, Aufbau und Betriebsführung eines Zweiwelligen Turbinenprüfstandes**, PhD Thesis 2012

[6] A.Gehrer **Entwicklung eines 3D-Navier-Stokes Codes zur numerischen Berechnung der Turbomaschinenströmung**, PhD Thesis 1998

[7] W. Sanz **CFD in Turbomaschinen und Energieanlagen**, Skriptum TUGraz 2006

[8] S. Martens **Strömungsmechanik und Stoffaustausch**, Skriptum TUGraz

[9] P. Bas, A. Mooren **Optimization of the Mixing Chamber and Intake of the Test Turbine at the Institute of Thermal Turbomachinery and Machine Dynamics**, Diploma Thesis 1998

[10] P.A. Leitl **CFD-Simulation einer Verdichtereinheit zur Motorenaufladung**, Diploma Thesis 2009

[11] **ANSYS FLUENT Theory Guide**, Release14 2011

[12] **ANSYS FLUENT User Guide**, Release14 2011

Internet Links

[13] Peter Junglas **Strömunglehre 3**, 10 Juli 2013, <http://www.peter-junglas.de/fh/vorlesungen/stroemungslehre3/html/kap3-1.html>

[14] aasche **CFD-Strömungssimulation**, 9 Januar 2013, 10 Juli 2013, <http://wiki.ubuntuusers.de/CFD_-_Str%C3%B6mungssimulation>

[15] ANSYS Inc. **ANSYS Fluent**, 2013, 21 Juli 2013, <http://www.ansys.com/Products/Simulation+Technology/Fluid+Dynamics/Fluid+Dynamics+Products/ANSYS+Fluent>

[16] cfd−online **cfd−online**, constant request of information, <http://www.cfd-online.com/>